Novel effects in quantum dot spectroscopy: Pseudospin blockade and level renormalization

Dissertation
zur Erlangung des Doktorgrades
des Fachbereichs Physik
der Universität Hamburg

vorgelegt von
Bernhard Wunsch
aus München

Hamburg
2006

Gutachter der Dissertation:	Prof. Dr. D. Pfannkuche Prof. Dr. G. Platero
Gutachter der Disputation:	Prof. Dr. D. Pfannkuche Prof. Dr. J. König
Datum der Disputation:	27.04.2006
Vorsitzender des Prüfungsausschusses:	Prof. Dr. A. Lichtenstein
Vorsitzender des Promotionsausschusses:	Prof. Dr. G. Huber
Dekan des Departments Physik:	Prof. Dr. A. Frühwald

To my wife Inés and to my son Marco

Abstract

Topic of this thesis are electronic properties and transport characteristics of single and double quantum dots. We begin with a discussion of the effects of Coulomb interaction on the eigenspectra of isolated single and double dots. Thereafter, we study consequences of these many-particle effects for the transport characteristics of dots that are coupled to external contacts. In these studies the limit of weak coupling is considered which allows to neglect any back action of the external coupling on the eigenspectrum of the dot structures. In the last part of this thesis we extend our description of quantum transport and describe effects of the external coupling on the eigenspectrum and transport characteristics of a double dot.

In the first part we discuss the excitation spectrum and the transport properties of a single two-dimensional dot with parabolic confinement. Classical and quantum mechanical effects of Coulomb interaction on the charge density excitations are studied for various numbers of electrons confined to the dot. The calculations explain recently measured Raman spectra of self-assembled dots. Thereafter, a blocking mechanism in the nonlinear transport regime is introduced, which completely suppresses the stationary current through the dot. The presented blocking mechanism only occurs if the Coulomb interaction exceeds the single particle level spacing and the blockade can be switched on and off by an external magnetic field.

The second part deals with the consequences of Coulomb interaction on the eigenspectrum and the transport properties of two vertically coupled dots. It is shown that a vertical magnetic field can tune a spontaneous charge polarization in vertical direction of the 3-electron ground state. This strong charge polarization is caused by the different magnetic-field dependence of the intra- and interdot Coulomb interaction and has severe consequences on the serial transport through the double dot. In particular linear transport through the double dot is blocked at the critical magnetic field.

In the last part of the thesis we study again the transport characteristics of a double dot coupled in series to external contacts. Now we consider the regime when the external coupling exceeds the interdot tunneling energy and extend our description of the double dot, by considering also superpositions of eigenstates. In fact we find that these superpositions are relevant since they describe the interplay between the decoherent coupling to the external contacts and the coherent dynamics on the double dot. Analogies to related work in the field of spintronics are pointed out. Furthermore, we find that the external coupling shifts the energy of the dot levels which results in characteristic features in the current-voltage characteristic of the double dot as well as in its stability diagram.

Zusammenfassung

Das Thema dieser Doktorarbeit sind elektronische Eigenschaften sowie Transporteigenschaften von Einzel- und Doppelquantenpunkten. Zunächst werden verschiedene Effekte der Coulombwechselwirkung auf die Eigenspektren der Quantenpunktsysteme untersucht. Danach wird aufgezeigt, welche Konsequenzen sich aus diesen Vielteilcheneffekten für die Transporteigenschaften von Quantenpunkten ergeben, wenn sie an externe Kontakte gekoppelt sind. In diesen Rechnungen wird vorerst angenommen, dass die externe Ankopplung schwach genug ist, um alle Rückwirkungen der externen Kontakte auf das Eigenspektrum der Quantenpunktstrukturen vernachlässigen zu können. Im letzten Teil der Arbeit wird die Beschreibung des Quantentransports erweitert und es wird gezeigt, wie sich Eigenspektrum und Transporteigenschaften eines Doppelquantenpunktes bei stärkerer externener Ankopplung ändern.

Im ersten Teil der Arbeit werden Anregungsspektrum und Transporteigenschaften eines einzelnen zweidimensionalen Quantenpunktes mit parabolischem Einschlusspotential besprochen. Klassische und quantenmechanische Auswirkungen der Coulombwechselwirkung auf die Ladungsdichteanregungen für verschiedene Elektronenzahlen im Quantenpunkt werden präsentiert. Diese Rechnungen erklären aktuelle Ramanspektren von selbstorganisiert gewachsenen Quantenpunkten. Danach wird ein Mechanismus diskutiert, der im nichtlinearen Transportregime zu einer vollständigen Unterdrückung des stationären Stroms durch den Quantenpunkt führt. Dabei tritt der dargestellte Mechanismus nur auf, wenn die Coulombwechselwirkung stärker als die Einteilchenanregungen des Quantenpunktes ist. Desweiteren kann die Blockade durch ein externes Magnetfeld an- und ausgeschaltet werden.

Im zweiten Teil dieser Arbeit werden die Auswirkungen der Coulombwechselwirkung auf Eigenspektrum und Transportcharakteristik zweier vertikal gekoppelter Quantenpunkte besprochen. Es zeigt sich, dass ein vertikales Magnetfeld eine spontane Ladungspolarisation des 3-Elektronengrundzustandes in vertikaler Richtung bewirken kann. Diese starke Ladungspolarisation wird durch eine unterschiedliche Magnetfeldabhängigkeit der Intra- und Interdotcoulombwechselwirkung hervogerufen und hat weitreichende Auswirkungen auf den Transport durch den seriell angekoppelten Doppelquantenpunkt. Insbesondere wird der lineare Transport durch den Doppelquantenpunkt am kritischen Magnetfeld nahezu vollständig unterdrückt.

Im abschließenden Teil der Arbeit werden erneut die Transporteigenschaften eines Doppelquantenpunktes berechnet, der seriell an externe Kontakte gekoppelt ist. Nun wird der Fall betrachtet, bei dem die externe Ankopplungsstärke größer als das Tunneln zwischen den Quantenpunkten ist. Dazu wird die Beschreibung des gekoppelten Doppelquantenpunktes um kohärente Überlagerungen von Eigenzuständen erweitert. Tatsächlich zeigt sich, dass in dem diskutierten Parameterbereich diese Überlagerungen für die Beschreibung des Zusammenspiels von der inkohärenten externen Ankopplung und der kohärenten Dynamik auf dem Doppelquantenpunkt notwendig sind. Der Zusammenhang zu ähnlichen Arbeiten im Bereich der Spintronic wird diskutiert. Darüberhinaus führt die externe Ankop-

plung zu einer Verschiebung der Energieniveaus der Quantenpunkte und somit zu neuen charakteristischen Merkmalen in der Strom-Spannungskennlinie und des Stabilitätsdiagramms des Doppelquantenpunktes.

Contents

1 Introduction

The physical concepts of the macroscopic and the microscopic world are principally different. While the basics for the macroscopic world and in particular all physical phenomena in our everyday world are described by classical mechanics and Maxwell equations, the microscopic world appearing at the atomic scale needs to be described by quantum mechanics.

The task of mesoscopic physics is to describe the intermediate regime, where on the one hand the system size is already smaller than the phase coherence length, so that quantum mechanical effects become relevant, but at the same time the system still consists of millions of atoms. The relevance of mesoscopic physics is not only explained by the thirst of knowledge of scientists, but also by the tremendous speed of the miniaturization of electronic devices. The electronic industry performs this task in a top-down approach, starting with their currently working devices and watching what happens upon shrinking them. Theoretically appealing is a bottom-up scheme, starting with the well understood quantum mechanical description of atomic physics. However, this is a rather hopeless approach since the complexity of the exact quantum mechanical calculations grows exponentially with the system size. The typical task in mesoscopic physics is thus to find an effective model, where the huge number of degrees of freedom can be reduced to a few characteristic ones.

Quantum dot systems are particularly suited for a prolific cooperation between experimentalists and theoreticians in mesoscopic physics, since they combine a microscopic understanding of the Hamiltonian of these systems with a tremendous experimental control over the system parameters. In particular semiconductor quantum dots can be designed on purpose since they are fabricated by semiconductor growth and processing technologies. A quantum dot is a quasi zero-dimensional electron system where electrons are confined in all spatial directions, giving rise to discrete single-particle levels. Furthermore the Coulomb interaction between the confined electrons together with the small volume results in a considerable addition energy needed before an extra electron can be put on the dot. Depending on the size of the dot the addition energy varies between 1-100 meV, which exceeds considerably the temperature used in current experiments, so that the Coulomb interaction stabilizes the electron number. The relative magnitude of single-particle level spacing and Coulomb interaction is preset by design. In general the influence of Coulomb interaction on the eigenspectrum increases with decreasing confinement.

For small dots where the level spacing exceeds the Coulomb interaction between two electrons, the few-particle eigenspectrum shows many analogies to atomic physics. The eigenstates e.g. can be approximated by consecutively filling the single-particle levels, following

Hund's rule and the Aufbau principle known from atomic physics. Quantum dots are therefore often called artificial atoms. However, in contrast to atoms where confinement and electron number are determined by nature, quantum dots are man made structures allowing for example to systematically charge the dot with additional electrons. Furthermore due to the much weaker confinement and larger spatial extend of quantum dots in comparison to atoms, the eigenspectrum becomes much more sensitive to an external magnetic field. This allows to induce groundstate transitions in quantum dots at typical magnetic fields available in laboratories, while the corresponding transitions in atoms would require magnetic fields of the order of 10^6 Tesla. All these features show, that quantum dots offer a great opportunity to study many-particle physics.

A further enrichment of the physics of quantum dots is achieved by coupling several dots. Such coupled dots can then be thought of as artifical molecules and again, the high experimental control over the system parameters, like interdot coupling, confinement or occupation offers a systematic study of the many-particle and molecular physics.

Other keywords used in the context of quantum dot structures are spintronics, quantum computation or quantum cellular automata. In spintronics, one looks for electronic devices using not only the charge degree of freedom but also the spin of the electrons. This is particularly desirable since the spin degree is much less volatile than the charge degree of freedom, resulting in relatively long coherence times, which are a prerequisite of quantum computations. In quantum computing one tries to exploit the unique feature of quantum mechanics namely entanglement and superposition to perform computations that are not possible classically.

Other astonishing effects arise in transport through quantum dot structures. If a quantum dot structure is integrated in an electrical circuit, by connecting it via high tunneling barriers to external contacts, and if the temperature is low enough, then the Coulomb interaction and the discrete energy spectrum of the dot are manifest in the transport characteristics. In particular in the weak coupling regime and for small applied voltages transport is only possible at discrete energies, where the tunneling electron has the necessary energy to overcome the Coulomb interaction on the dot, while at other energies the dot is in the Coulomb blockade. In most experiments, the transport channels of the dot can be continuously shifted upwards or downwards in energy by a side gate. Due to the Coulomb blockade the current shows peaks in the linear transport regime as function of the voltage applied to the side gate. Complementary, the spectrum of the dot can be investigated in the nonlinear transport. As function of the transport voltage the current has the form of a staircase and correspondingly the differential conductance shows a peak structure, where the position of the steps or peaks reveals the excitation spectrum of the dot, while their height depends on the form of its eigenfunctions. Another important question concerns the influence of the external coupling on the eigenspectra of the dot. With increasing external coupling renormalizations of energy levels show up. Furthermore the Coulomb blockade, which is characteristic for the weak coupling regime, can be canceled by higher order tunneling processes. Finally Kondo physics arise in the regime of strong external coupling and for strong Coulomb interaction.

This work however is restricted to the weak coupling regime, where transport can be described by independent tunneling processes occurring one after the other. The aim of this thesis is to study many-particle effects based on Coulomb interaction in single and double quantum dots containing few electrons and the manifestations of these effects in optical spectroscopy and mainly in transport experiments.

After the introduction, the few-electron eigenspectrum of a two-dimensional harmonic quantum dot and its manifestation in optical and transport experiments is studied in chapter 2. First the effect of Coulomb interaction on the charge density excitations is discussed for various numbers of electrons confined to the dot. The presented calculations allowed to interpret recent Raman spectra. Thereafter different aspects of Coulomb interaction are discussed for the transport through the dot. In particular a blockade mechanism is introduced, that results in a complete suppression of the nonlinear current through the dot.

In chapter 3 the spectrum and the transport properties of a vertically coupled double dot containing few electrons are studied. It is shown that the different magnetic field dependence of intra- and interdot Coulomb interaction can induce a spontaneous charge polarization in the three-electron ground state at critical magnetic fields. Again this many-particle effect has severe consequences on the transport characteristic of this structure, if it coupled in series to external contacts. In particular the current through the double dot vanishes at the critical magnetic fields.

In chapter 4 the influence of the external coupling on the eigenspectrum and the transport characteristics of a double dot coupled in series to external contacts is investigated. When the coupling to the external contacts is of the same order or even larger than the interdot coupling, then the transport through the double dot changes significantly with respect to limit of weak external coupling. Then transport through the double dot is accompanied by partially coherent dynamics on the double dot, corresponding to superpositions of different eigenstates. Furthermore the external coupling shifts the energy of the dot levels. Consequences of these effects are already visible at rather high temperatures, where transport is dominated by incoherent tunneling processes.

Some of the main results of this thesis have already been published.

Publications

- *"Spectroscopy of Few-Electron Collective Excitations in Charge-Tunable Artificial Atoms"* [1].
- *"Inelastic light scattering on few-electron quantum-dot atoms"* [2].
- *"Charge localization and isospin blockade in vertical double quantum dots"* [3].
- *"Isospin blockade in transport through vertical double quantum dots"* [4].
- *"Probing level renormalization by sequential transport through double quantum dots"* [5].

2 Few-electron quantum dots

The eigenspectrum of a quantum dot containing few electrons is determined by the single-particle spectrum on the one side and the Coulomb interaction on the other side. In semiconductor quantum dots the single-particle spectrum is often well described by the Fock-Darwin spectrum, which assumes a two-dimensional quantum dot with harmonic confinement potential in lateral direction. If one neglects the interaction between electrons for a moment, the few-particle spectrum is obtained by consecutively filling the single-particle levels with electrons. However this simple picture can be strongly modified by the interaction between the electrons. In this chapter we discuss the effect of Coulomb interaction on the spectroscopy of quantum dots for two different experimental setups.

In the first case we show how the Coulomb interaction affects the charge density excitations of self-assembled dots. In general we find that with increasing Coulomb energy the excitations spread over a broader energy regime where the upper limit is given by the single-particle excitation. Furthermore the excitation spectrum reveals the shell structure of the single-particle levels.

In the second case we study a blocking mechanism arising in transport experiments due to transitions to excited states. The blocking mechanism depends on the excitation spectrum at constant electron number as well as on the energy differences between the ground-states energies corresponding to consecutive electron numbers. The characteristics of these energies strongly depends on the Coulomb energy and in particular we show that the blocking mechanism disappears for strong confinement.

In the following we first discuss different experimental realizations of semiconductor quantum dots in section 2.1. Then, in section 2.2 the effective theoretical model for these dots is introduced and it is shortly explained how the eigenspectra can be obtained by means of exact diagonalization. In section 2.3 the effects of Coulomb interaction on the charge density excitations of self-assembled dots are studied depending on the number of electrons occupying the dots. These calculations were used to understand recent experimental results obtained by resonant Raman spectroscopy and are published together with the experimental data in references [1, 2]. In section 2.4 the transport spectroscopy of quantum dots is shortly introduced, which is valid if the external coupling sets the lowest energy scale. This approach is then applied to study a blocking mechanism for the nonlinear current through the dot in section 2.5. Finally we conclude this chapter in section 2.6.

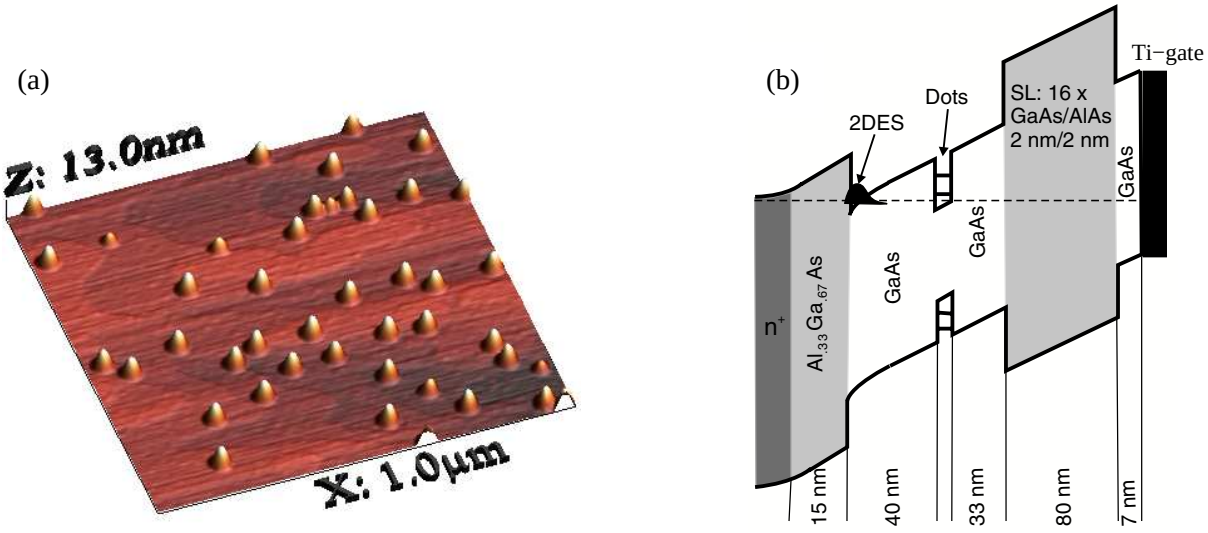

Figure 2.1: *a) Atomic-force-microscope image of an array of self-assembled InAs quantum dots (taken from the group of Prof. Hansen, university of Hamburg). b) Schematic energy profile for conductance band and valence band of heterostructure, where dots are embedded. The occupation of the dot with electrons can be tuned by the voltage applied between the two-dimensional electron system and the titanium top gate. Data taken from reference [1].*

2.1 Experimental realizations

In this work we focus on semiconductor quantum dots, containing few conduction electrons. In the following we shortly discuss three important types of quantum dots, namely self-assembled dots, lateral or planar dots, and vertical dots.

Self-assembled dots

Self-assembled dots form spontaneously during an epitaxial growth process. Choosing the right experimental conditions, InAs grown on a GaAs substrate forms nanometers sized islands for energetic reasons.[6] Fig. 2.1 a) shows an array of self-assembled dots as they are realized in the experimental group of Prof. Hansen at the university of Hamburg. All dots have approximately the same size, however they are randomly distributed on the GaAs surface. By overgrowing these islands again with GaAs one can confine electrons in these InAs dots in all three dimensions due to the much higher bandgap of the surrounding GaAs material. The single-particle-excitation energy for the lateral motion is about 50 meV. The motion in vertical direction is typically restricted to the ground state,

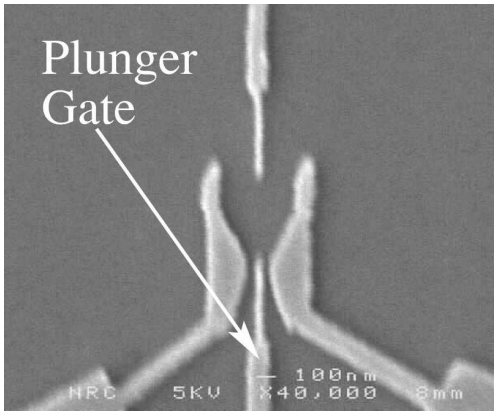

Figure 2.2: *Scanning-tunneling-microscope image of the gate geometry forming a lateral quantum dot in the 2DES about 90nm below the surface. The plunger gate allows to trap a precise number of electrons varying from 0-50. In a transport experiment a characteristic current flows through this structure as response to an applied source drain voltage not shown in this graph. Figure taken from [8].*

since the vertical confinement is about an order of magnitude larger than the lateral one. Fig. 2.1 b) shows the growth sequence and the band structure of the heterostructure where the dots are embedded. The two-dimensional electron system (2DES), residing in an inverted heterostructure, acts as a back contact, while the titanium gate is deposited on top of the sample. By applying a gate voltage between top and back contact the quantum dots can be charged by single electrons.

Lateral dots

A lateral or planar quantum dot is created by patterning several metal electrodes, or gates, on the surface of a 2DES-heterostructure, usually of GaAs.[7] Applying a negative voltage to the gates raises the electrostatic potential in their neighborhood and depletes the 2DES in the vicinity of the gates. The confinement in vertical direction is thus provided by a quantum well produced by the growth process, while the lateral confinement is caused by the electrostatic potentials of the gates. Fig. 2.2 shows the setup of a lateral quantum dot, which can be emptied completely.[8] Depending on the voltage applied to the plunger gate, the dot can be precisely charged with electrons, starting from the empty dot up to about 50 electrons. Connecting the outer regions of the 2DES with a source and drain contact one can run a current through the quantum dot as response to a transport voltage. In the weak coupling regime, where we are interested in, the current flow is then caused by a sequence of single electrons hopping one after the other from source contact into the dot and then out to the drain contact. The corresponding tunneling rates and thus the current through the dot strongly depend on the properties of the dot, like its single-particle spectrum and the Coulomb energy. The manifestation of the dot spectrum in transport measurements is one of the main topics of this thesis. Thereby we limit our studies to the weak coupling regime, where the external coupling can be treated as a small perturbation.

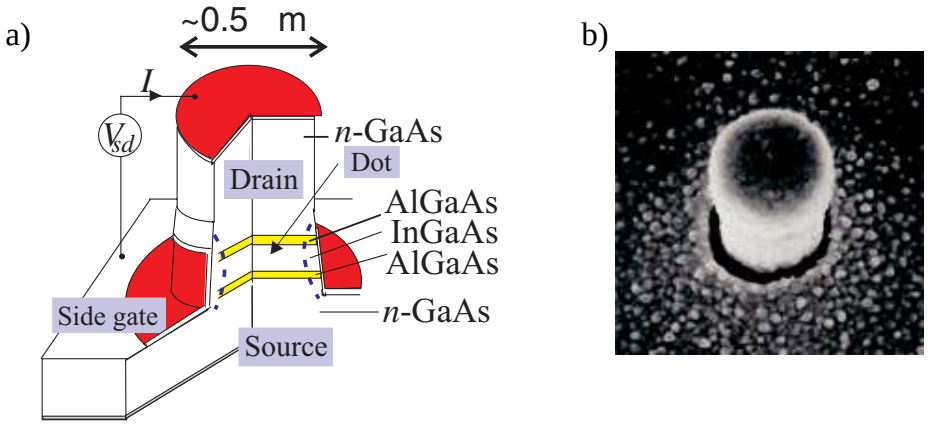

Figure 2.3: *a) Schematic diagram of vertical quantum dot. b) Scanning-tunneling-micrograph of quantum dot pillar. Data taken from [9] .*

Vertical dots

Vertical dots like the one depicted in Fig. 2.3 are fabricated by etching a pillar out of a semiconductor double barrier structure defined by the growth process.[9] A side gate is added by depositing a metal electrode around the pillar. The confinement of the dot is defined in z-direction by a double barrier structure and in lateral direction by the interplay of the surface potential and the gate potential. In contrast to planar dots, where electrons tunnel within the electron layer, the current now consists of electrons tunneling vertically through the double barriers. Therefore in vertical structures the electrons couple more or less to the entire area of the quantum dot and the tunnel amplitudes can be assumed to be independent of the single-particle orbitals, while in lateral quantum dots the electrons tunnel into the edges, which might lead to an orbital dependence of the tunnel amplitudes.

2.2 Many-particle eigenspectrum

In this section we show how we calculate the eigenspectrum of a quasi two-dimensional harmonic quantum dot. Therefore we first discuss its analytically solvable single-particle spectrum, known as Fock-Darwin spectrum. Then we dicuss the effects of Coulomb interaction, which we are going to include non-perturbatively via an exact diagonalization of the many-particle Hamiltonian.

2.2.1 Fock-Darwin Hamiltonian

The first task for a calculation of the electronic states in a quantum dot is to identify a good Hamiltonian (i.e. the possible approximations) to start with. Since the external confinement that defines the quantum dot is smooth on the atomic length scale it is allowed to

start with an effective Schrödinger equation determining the envelope wavefunction within the effective mass approximation. Furthermore the vertical confinement is much stronger than the lateral one, so that the motion in z-direction is frozen for all relevant eigenstates. Often the quasi two-dimensional confinement is turned into a strict two-dimensional one, by restricting the motion in z-direction to a delta layer. The lateral motion is often well described by a rotationally-symmetric parabolic confinement (harmonic confinement), which was shown theoretically in self-consistent calculations [10], and furthermore is justified by the good agreement between theoretical calculations and experimental data [9, 11, 12].

A single electron moving in a two-dimensional quantum dot with harmonic confinement potential and subject to a magnetic field B, perpendicular to its plane of motion, is well described by the Fock-Darwin Hamiltonian:

$$\hat{H} = \frac{1}{2m^*}\left(\vec{p} + e\vec{A}\right)^2 + \frac{m^*\omega_0^2}{2}r^2 \quad . \tag{2.1}$$

Here $\vec{A}$ denotes the vector potential with $rot(\vec{A}) = Be_z$, ω_0 the strength of the parabolic confinement potential, m^* the effective mass, and e is the positive elementary charge (i.e. the electron has the charge $q = -e$). The momentum $\vec{p}$ and the spatial vector $\vec{r}$ are restricted to the plane perpendicular to the magnetic field.

In addition to the orbital dynamics described by the Hamiltonian above, the magnetic field also causes a Zeeman splitting of the spin levels

$$\hat{H}_Z = g^*\frac{\mu_B}{\hbar}B\hat{S}_z \; . \tag{2.2}$$

Here μ_B is the Bohr magneton and g^* the effective Landé factor. In GaAs the Zeeman term is often neglectable, since the Zeeman splitting of spin-degenerate states is about 70 times smaller than the splitting of the orbital degree of freedom in a magnetic field (orbital Zeeman term). Furthermore, the many-particle Hamiltonian describing several interacting electrons confined to the quantum dot, commutes with the spin, so that the Zeeman term only shifts the eigenenergies a little bit, while it leaves the many-particle eigenstates unaffected.

Fock-Darwin eigenspectrum

The Schrödinger equation corresponding to the Fock-Darwin Hamiltonian (2.1) was first solved independently by Fock and Darwin [13, 14]. Its energy eigenspectrum is given by:

$$E_{nm} \;=\; \hbar\omega_{eff}(2n + |m| + 1) + \frac{\hbar\omega_c}{2}m \; . \tag{2.3}$$

Here $\omega_c = \frac{eB}{m^*}$ denotes the cyclotron frequency and $\omega_{eff} = \sqrt{\omega_0^2 + \frac{\omega_c^2}{4}}$ the effective confinement frequency. The relevant energies that determine the single-particle spectrum are therefore: $\hbar\omega_c$, $\hbar\omega_0$, $\hbar\omega_{eff}$. The eigenstates are denoted by the principal quantum number n and by the angular momentum m. The energy spectrum as function of magnetic field is illustrated in Fig. 2.4. With increasing magnetic field, states with highest negative angular

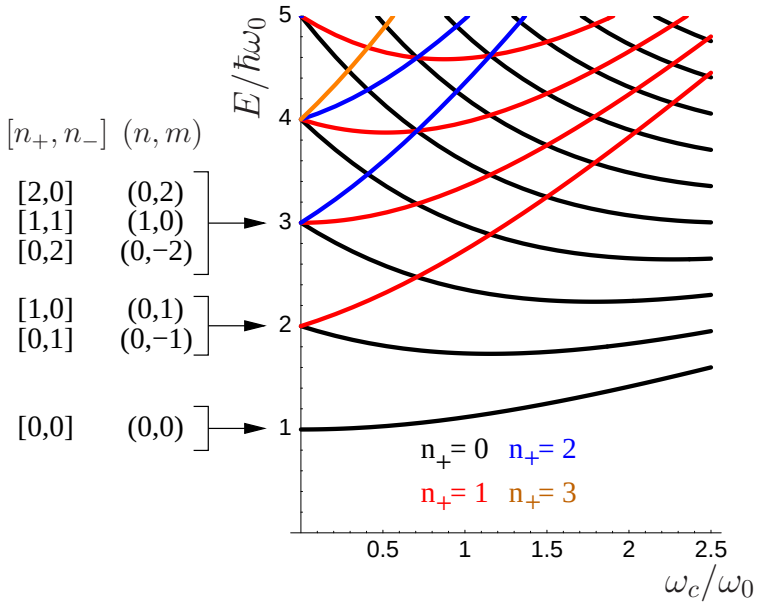

Figure 2.4: *Fock-Darwin spectrum as function of the external magnetic field. Eigenstates can either be labeled by the oscillator quantum numbers n_+, n_- or by principal quantum number and angular momentum n, m. The two representations are connected by Eq. (2.8). For high magnetic fields n_+ labels the Landau levels. In particular, states with minimum angular momentum $m = -n$ i.e. with $n_+ = 0$ converge to the lowest Landau level.*

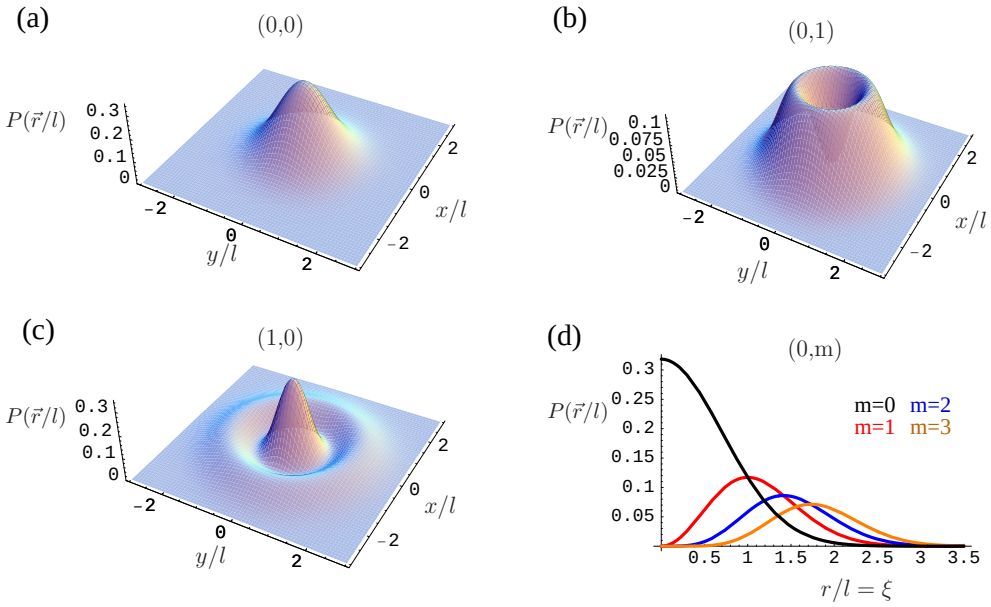

Figure 2.5: *a)-c) Probability density $P(\vec{r}/l) = |\langle n, m|\, \vec{r}/l\, |n, m\rangle|^2$ for the lowest eigenstates. (d) With increasing angular momentum the probability distribution is broadened.*

momentum $m = -n$ are favored. Fig. 2.4 also includes the oscillator representation of the eigenstates, which we introduce below.

One set of eigenstates are the Fock-Darwin states $|nm\rangle$:

$$\begin{aligned}
\langle \vec{r}|nm\rangle = \psi_{nm}(\vec{r}) &= \phi_m(\varphi)\rho_{nm}(r) = \frac{1}{l}\phi_m(\varphi)\tilde{\rho}_{nm}(\frac{r}{l}) \\
\tilde{\rho}_{nm}(\xi) &= (-1)^n\sqrt{\frac{2n!}{(n+|m|)!}}\xi^{|m|}e^{-\xi^2/2}L_n^{|m|}(\xi^2) \\
\phi_m(\varphi) &= \frac{1}{\sqrt{2\pi}}e^{im\varphi} \\
l &= \sqrt{\hbar/(m^*\omega_{eff})}
\end{aligned} \tag{2.4}$$

Here l denotes the characteristic length scale of the quantum dot, which exclusively contains confinement ω_0 and magnetic field ω_c. The radial part $\rho_{nm}(r)$ of the wavefunction is form-invariant under a change of either ω_0 or ω_c, or in other words an increase (decrease) in either ω_0 or ω_c shrinks (stretches) the radial wavefunction $\rho_{nm}(r)$ without changing its characteristic form. Mathematically this follows from the fact that $\tilde{\rho}_{nm}(\xi)$ is independent of ω_0 and ω_c. Furthermore the radial wavefunction $\rho_{nm}(r)$ only depends on the absolute value of the angular momentum m.

We put the prefactor $(-1)^n$ (which is a mere phase factor) in the definition of the radial wavefunction to allow a direct transformation between the Fock-Darwin eigenstates and the bosonic representation of eigenstates introduced below. As an example of the eigenfunction we mention that the ground-state wavefunction is given by $\psi_{00}(\vec{r}) = \frac{1}{l\sqrt{\pi}}e^{-\frac{r^2}{2l^2}}$. Figure 2.5 shows the probability density of the lowest eigenfunctions. In general the extend of the wavefunction increases with the magnitude of the angular momentum see Figure 2.5 (d) while the principal number gives the number of nodes in the radial part see Figure 2.5 (c).

Introduction of ladder operators

The Hamiltonian can also be represented by the bosonic operators $a_\pm^\dagger, a_\pm$ of a harmonic oscillator [15]

$$\begin{aligned}
a_\pm^\dagger &:= \frac{1}{\sqrt{2}}(a_x^\dagger \pm i a_y^\dagger)\,;\; a_\pm := \frac{1}{\sqrt{2}}(a_x \mp i a_y) \\
a_x &:= \frac{1}{\sqrt{2}}(\frac{x}{l} + i\frac{l}{\hbar}p_x)\,;\; a_y := \frac{1}{\sqrt{2}}(\frac{y}{l} + i\frac{l}{\hbar}p_y)\,.
\end{aligned} \tag{2.5}$$

They fulfill canonical commutator relations ($i, j \in \{x, y, +, -\}$)

$$\left[a_i, a_j^\dagger\right] = \delta_{ij};\; [a_i, a_j] = \left[a_i^\dagger, a_j^\dagger\right] = 0\,. \tag{2.6}$$

With the help of the bosonic operators the Hamiltonian and its eigenspectrum can be rewritten in the following form:

$$\begin{aligned}
\hat{H}_{FD} &= \hbar\Omega_+ \left(a_+^\dagger a_+ + \frac{1}{2}\right) + \hbar\Omega_- \left(a_-^\dagger a_- + \frac{1}{2}\right) \\
E_{|n_+n_-\rangle} &= \hbar\Omega_+(n_+ + \frac{1}{2}) + \hbar\Omega_-(n_- + \frac{1}{2}) = \hbar\omega_{eff}(n_+ + n_- + 1) + \frac{\hbar\omega_c}{2}(n_+ - n_-) \\
|n_+, n_-\rangle &= \frac{(a_+^\dagger)^{n_+}}{\sqrt{n_+!}} \frac{(a_-^\dagger)^{n_-}}{\sqrt{n_-!}} |0,0\rangle \\
\Omega_\pm &= \omega_{eff} \pm \frac{\omega_c}{2} \,. \qquad (2.7)
\end{aligned}$$

The angular momentum expressed by the ladder operators is: $\hat{L}_z = \hbar\left(a_+^\dagger a_+ - a_-^\dagger a_-\right)$. Since both presented eigensystems to the Hamiltonian (2.1) (either the Fock-Darwin states described by the quantum number n, m or the eigenstates described by n_+, n_-) are also eigenstates to $\hat{L}_z$, there is a one to one correspondence between both systems, given by:

$$\begin{aligned}
m &= n_+ - n_- \\
n &= min(n_+, n_-) = \frac{n_+ + n_- - |n_+ - n_-|}{2} \\
n_\pm &= \frac{2n \pm m + |m|}{2} \,. \qquad (2.8)
\end{aligned}$$

In general the space representations of corresponding eigenstates (connected by equations (2.8)) can still differ by a phase factor, i.e. $\langle\vec{r}|nm\rangle = \alpha(n,m)\langle\vec{r}|n_+n_-\rangle$. However, by adding the prefactor $(-1)^n$ in the definition of the Fock-Darwin eigenstates this phase factor is always one, i.e. $\langle\vec{r}|nm\rangle = \langle\vec{r}|n_+n_-\rangle$ if Eq. (2.8) are fulfilled.

The oscillator representation is particularly useful to describe the high magnetic field regime defined by $\omega_c \gg \omega_0$, so that $\Omega_+ \to \omega_c$ and $\Omega_- \to 0$. In this regime n_+ labels the Landau levels and n_- labels the excitations within a Landau level caused by the comparatively low confinement ω_0, see Fig. 2.4.

2.2.2 Coulomb interaction

In this work we take the full Coulomb interaction into account, represented by

$$\hat{\mathcal{V}}_c = \frac{1}{2}\frac{1}{\kappa}\sum_{i,j=1}^{N_e}\frac{1}{r_{ij}} \qquad (2.9)$$

with $r_{ij} = |\vec{r}_i - \vec{r}_j|$ and $\kappa = \frac{4\pi\varepsilon_0\varepsilon}{e^2}$, where ε denotes the relative dielectric constant of the host material. The Coulomb interaction only acts on the orbital degree of freedom and

thus commutes with the square of the real total spin and with all spin components:

$$[\hat{\mathcal{V}}_c, \vec{S}] = 0 \ , \quad \vec{S} = \sum_{i=1}^{N_e} \vec{S}^{(i)} \tag{2.10}$$

Furthermore the Coulomb interaction only acts on the relative coordinates, while it is independent of the center of mass motion. Together with the rotational invariance of $\hat{\mathcal{V}}_c$, this leads to the following commutator relations:

$$[\hat{\mathcal{V}}_c, L_z] = 0 = [\hat{\mathcal{V}}_c, L_z^{(rel)}] = [\hat{\mathcal{V}}_c, L_z^{(cm)}] \ , \quad L_z = \sum_{i=1}^{N_e} L_z^{(i)} \tag{2.11}$$

Here $L_z^{(rel)}$ ($L_z^{(cm)}$) denotes the angular momentum of the relative (center of mass) motion. The eigenstates of the interacting dot can therefore be chosen to be simultaneously eigenstates of the z-component of the total spin and of the square of the total spin as well as of the total angular momentum in z-direction described by the quantum numbers S_z, S and M respectively. In section 2.3 we will furthermore determine the relative and center of mass angular momentum of the eigenstates.

Center of mass motion

In a quantum dot with harmonic confinement potential the dynamics of several electrons separates in the center of mass motion and the relative motion even in the presence of Coulomb interaction.[16, 17, 18] The center of mass motion is described by the noninteracting single-particle Hamiltonian (2.1), so that it is independent of interactions and the number of particles. Excitations of the center of mass motion therefore always appear at the single-particle excitation energies. In order to reveal many-particle effects it is necessary to excite the relative motion, which will be topic of section 2.3.

The conserved center of mass and relative angular momenta, denoted by $\hat{L}_z^{cm}$ and $\hat{L}_z^{rel}$, respectively, can be calculated with the ladder operator introduced in Eq. (2.5):

$$\begin{aligned}
\hat{L}_z &= \hbar \sum_{i=1}^{N_e} \left(a_{i+}^\dagger a_{i+} - a_{i-}^\dagger a_{i-} \right) \\
\hat{L}_z^{cm} &:= \hat{\vec{R}} \times \hat{\vec{P}} = 1/N_e \sum_{i=1}^{N_e} \hat{\vec{r}}_i \times \sum_{j=1}^{N_e} \hat{\vec{p}}_j = \hbar \left(A_+^\dagger A_+ - A_-^\dagger A_- \right) \\
A_\pm &= \frac{1}{\sqrt{N_e}} \sum_{i=1}^{N_e} a_{i\pm} \\
\hat{L}_z^{rel} &= \hat{L}_z - \hat{L}_z^{cm}.
\end{aligned} \tag{2.12}$$

Here N_e denotes the number of electrons.

Effective units and scaling of Coulomb interaction

We now comment on the relevance of the Coulomb interaction relative to the single-particle spacing. If one splits the motion of two electrons confined to the quantum dot in the center of mass and the relative motion of the electrons, one finds that the characteristic length scale for the relative motion is given by $l_{rel} = \sqrt{2}l$, where $l = \sqrt{\hbar/(m^*\omega_{eff})}$ denotes the confinement length introduced in Eq. (2.4). This calculation is performed in appendix A.1. The characteristic Coulomb energy is thus given by $1/(\kappa l_{rel})$. It can be related to the other characteristic energy scales $\hbar\omega_0$ and $\hbar\omega_c$ of the system by expressing distances in units of the effective Bohr radius a_0^* and energies in units of effective Rydbergs Ryd^* defined by:[19]

$$\begin{aligned} a_0^* &= \frac{\kappa\,\hbar^2}{m^*} \\ Ryd^* &= \frac{1}{2\kappa\,a_0^*} = \frac{\hbar^2}{2m^* a_0^{*2}}\,. \end{aligned} \tag{2.13}$$

The constant κ is given by $\kappa = 4\pi\varepsilon\varepsilon_0/e^2$. While in atomic physics a Rydberg is given by 13.6eV its effective value in semiconductors is drastically reduced to $Ryd^* = Ryd \cdot m^*/(m_0\,\varepsilon^2)$, where ε denotes the relative dielectric constant and m^* the effective mass. Accordingly the effective Bohr radius is strongly increased by $a_0^* = a_0\,\varepsilon\,m_0/m^*$, where the atomic Bohr radius is given by $a_0 = 5.29 \cdot 10^{-11}$m. The effective units absorb the material constants of the host material and the resulting values for InAs and GaAs are listed in Table 2.1. We now note the following identities:

$$\frac{1}{\kappa l_{rel}} = Ryd^* \sqrt{\frac{\hbar\omega_{eff}}{Ryd^*}} \tag{2.14}$$

$$\left(\frac{l}{a_0^*}\right)^2 = 2\frac{Ryd^*}{\hbar\omega_{eff}}\,. \tag{2.15}$$

The consequences of these equations become obvious in the absence of a magnetic field, i.e. for $\omega_{eff} = \omega_0$. In that case the characteristic interaction energy exceeds the single-particle level spacing for a confinement of $\hbar\omega_0 < 1Ryd^*$ (i.e. a characteristic length $l > \sqrt{2}a_0^*$), while the characteristic interaction energy is lower than the single-particle level spacing for $\hbar\omega_0 > 1Ryd^*$ (i.e. $l < \sqrt{2}a_0^*$).

Throughout chapter 2 and chapter 3 we will always use these energy units if not stated otherwise. Concerning the magnetic field we note that it only enters the Hamiltonian via the cyclotron frequency $\omega_c = eB/m^*$, which is proportional to the magnetic field. With the material constants of GaAs listed in Table 2.1 we find that a magnetic field of 1 Tesla corresponds in GaAs to $\hbar\omega_c = 0.29Ryd^*$ and vice versa $\hbar\omega_c = 1Ryd^*$ corresponds to a magnetic field of $B \approx 3.45T$.

Matrix elements of Coulomb interaction

We reexpress the Coulomb interaction $\hat{\mathcal{V}}_c$ introduced in Eq. (2.9) using Eq. (2.13) and

	m^*/m_0	ε	a_0	Ryd^*
GaAs	0.067	12.4	9.79 nm	5.93 meV=68.8 Kelvin $^*k_B$
InAs	0.0239	15.15	33.5 nm	1.42 meV=16.5 Kelvin $^*k_B$

Table 2.1: Material constants and values of effective units. k_B denotes the Boltzmann constant.

Eq. (2.14) by:

$$\hat{\mathcal{V}}_c^* = \sqrt{\hbar\omega_{eff}^*}\frac{1}{2}\sum_{i,j=1}^{N_e}\frac{l_{rel}}{r_{ij}} \tag{2.16}$$

Here the superscript $*$ again denotes that the quantity is given in units of Ryd^*, see Eq. (2.13). It is important to note the matrix elements of $\frac{l_{rel}}{r_{12}}$ are independent of both confinement and magnetic field and are only a function of the quantum numbers defining the matrix element, which is based on the following relation:

$$\begin{aligned}
&\langle n_1 m_1, n_2 m_2 |\, l_{rel}/r_{12} \,| n_3 m_3, n_4 m_4\rangle := \\
&\quad = l_{rel}\int\int d^2r_1\, d^2r_2 \frac{\psi^*_{n_1\,m_1}(\vec{r}_1)\,\psi^*_{n_2\,m_2}(\vec{r}_2)\,\psi_{n_3\,m_3}(\vec{r}_1)\,\psi_{n_4\,m_4}(\vec{r}_2)}{r_{12}} \\
&\quad = \int\int d^2\xi_1\, d^2\xi_2 \frac{\tilde{\psi}^*_{n_1\,m_1}(\vec{\xi}_1)\,\tilde{\psi}^*_{n_2\,m_2}(\vec{\xi}_2)\,\tilde{\psi}_{n_3\,m_3}(\vec{\xi}_1)\,\tilde{\psi}_{n_4\,m_4}(\vec{\xi}_2)}{\xi_{12}}\,.
\end{aligned} \tag{2.17}$$

Here we used $\tilde{\psi}_{n\,m}(\vec{\xi}) = \tilde{\rho}_{n\,m}(\xi)\phi_m(\varphi)$ as defined in Eq. (2.4) and furthermore $\xi_{12} = |\vec{r}_1 - \vec{r}_2|/l_{rel} = \left|\vec{\xi}_1 - \vec{\xi}_2\right|/\sqrt{2}$, $\vec{\xi}_i = \vec{r}_i/l$. With Eq. (2.17) we expressed the matrix element only by functions that are independent of ω_0 and ω_c. For the actual calculation of the matrix elements shown in Eq. (2.17) it is useful to transform $\vec{r}_1, \vec{r}_2$ into relative and center of mass coordinates $\vec{R} = (\vec{r}_1 + \vec{r}_2)/2$ and $\vec{r} = (\vec{r}_1 - \vec{r}_2)$, as shown in Appendix A.2.

In Tables 2.2 and 2.3 we list matrix elements of the Coulomb energy for various basis states. Since the Coulomb interaction commutes with the total angular momentum the only non-vanishing matrix elements are $\langle n_1 m_1, n_2 m_2 |\, l_{rel}/r_{12} \,| n_3 m_3, n_4 m_4\rangle \propto \delta_{m_1+m_2,m_3+m_4}$. Table 2.2 lists examples of the direct and exchange Coulomb energy. We note that electrons in the s-shell interact strongest with each other while electrons in higher levels generally interact weaker due to the larger spatial extend of the wavefunctions. Furthermore the exchange term illustrates that the spin degree of freedom affects the Coulomb energy of a wavefunction, since it determines the symmetry of a wavefunction, even though the Coulomb operator itself is independent of the spin.

The matrix elements listed in Table 2.3 lead to superpositions of different states belonging to the same subspace M, S, S_z, giving rise to Coulomb correlations. These matrix elements are particularly important whenever different states belonging to the same subspace M, S, S_z have the same single-particle energy, so that they can easily be coupled

$\psi_1 = \|n_1 m_1\rangle$	$\psi_2 = \|n_2 m_2\rangle$	E_{12}^c	E_{12}^x
$\|0,0\rangle$	$\|0,0\rangle$	1	-
$\|0,0\rangle$	$\|0,\pm1\rangle$	$\frac{3}{4} = 0.75$	$\frac{1}{4} = 0.25$
$\|0,0\rangle$	$\|0,\pm2\rangle$	$\frac{19}{32} \approx 0.594$	$\frac{3}{32} \approx 0.094$
$\|0,0\rangle$	$\|1,0\rangle$	$\frac{11}{16} = 0.6875$	$\frac{3}{16} = 0.1875$
$\|0,\pm1\rangle$	$\|0,\pm1\rangle$	$\frac{11}{16}$	-
$\|0,\pm1\rangle$	$\|0,\mp1\rangle$	$\frac{11}{16}$	$\frac{3}{16}$

Table 2.2: Direct (E_{12}^c) and exchange (E_{12}^x) Coulomb energy for lowest orbitals in units of $\sqrt{\pi}\sqrt{\hbar\omega_{eff}^*}$ Ryd^*. [20] Definition: $E_{12}^c = \langle\psi_1,\psi_2|\,\frac{l_{rel}}{\vec{r}_{rel}}\,|\psi_1,\psi_2\rangle\,/\sqrt{\pi}$, $E_{12}^x = \langle\psi_1,\psi_2|\,\frac{l_{rel}}{\vec{r}_{rel}}\,|\psi_2,\psi_1\rangle\,/\sqrt{\pi}$, space-representation of Coulomb matrix elements given in Eq. (2.17).

n_1, m_1	n_2, m_2	n_3, m_3	n_4, m_4	$\langle n_1 m_1, n_2 m_2|\,\frac{l_{rel}}{r_{12}}\,|n_3 m_3, n_4 m_4\rangle\,/\sqrt{\pi}$
0, ±1	0, ±1	0, 0	0, ±2	0.221
0, 0	1, 0	0, 0	0, 0	0.25
0, 0	1, 0	0, ±1	0, ∓1	0.0625

Table 2.3: Coulomb matrix elements leading to correlations. Units chosen as in Table 2.2.

by Coulomb interaction. This will be discussed in section 2.3. Furthermore the matrix elements listed in Table 2.3 are also important for weak external confinement or strong magnetic fields, since then the single-particle level spacing is of the same order or lower than the Coulomb interaction matrix elements.

2.2.3 Full Hamiltonian in second quantization

The few-electron eigenspectrum of a harmonic quantum dot is determined by the following Hamiltonian:

$$\hat{\mathcal{H}} \;=\; \hat{\mathcal{H}}_{FD} + \hat{\mathcal{H}}_Z + \hat{\mathcal{V}}_c = \sum_i (\hat{H}_{FD}^{(i)} + \hat{H}_Z^{(i)}) + \frac{1}{2}\sum_{i,j} \hat{V}_c^{(i,j)}\,. \tag{2.18}$$

Here $\hat{\mathcal{H}}_{FD} = \sum_i \hat{H}_{FD}^{(i)}$ denotes the Fock-Darwin Hamiltonian (2.1), $\hat{\mathcal{H}}_Z = \sum_i \hat{H}_Z^{(i)}$ represents the Zeeman term (2.2) and $\hat{\mathcal{V}}_c = \frac{1}{2}\sum_{i,j} \hat{V}_c^{(i,j)}$ the Coulomb interaction on the dot, introduced in Eq. (2.9).
Written in second quantization the different parts of the Hamiltonian (2.18) have the

following form:

$$\begin{aligned}\hat{\mathcal{H}}_{FD} &= \sum_{nm\sigma} E_{nm} c^\dagger_{nm\sigma} c_{nm\sigma}\,; \;\; \hat{\mathcal{H}}_Z = g^* \frac{\mu_B}{2\hbar}(n_\uparrow - n_\downarrow) \\ \hat{\mathcal{V}}_c &= \frac{1}{\kappa l_{rel}} \frac{1}{2} \sum_{\substack{n_1,m_1\\n_2,m_2}} \sum_{\substack{n_3,m_3\\n_4,m_4}} \sum_{\sigma,\sigma'} \langle n_1 m_1, n_2 m_2| \, \frac{l_{rel}}{r_{12}} \, |n_3 m_3, n_4 m_4\rangle \, c^\dagger_{n_1 m_1 \sigma} c^\dagger_{n_2 m_2 \sigma'} c_{n_4 m_4 \sigma'} c_{n_3 m_3 \sigma} \; .\end{aligned}$$

The operator $c^\dagger_{n_i m_i \sigma}$ ($c_{n_i m_i \sigma}$) creates (annihilates) an electron with spin σ in the orbital $|n_i m_i\rangle$, and $\hat{n}_\sigma = \sum_{nm} c^\dagger_{nm\sigma} c_{nm\sigma}$ denotes the number of electrons with spin σ. The eigenspectrum is determined by the competition between $\hat{\mathcal{H}}_{FD}$ favoring a succeeding filling of the lowest single-particle states on the one side and the Coulomb interaction $\hat{\mathcal{V}}_c$ favoring a maximum distance between the electrons on the other side. The Coulomb interaction builds up correlations between the electrons and causes the occupation of higher orbitals.
Rewriting the Fock-Darwin term and the Coulomb interaction, defined in Eq. (2.1), (2.16), in the effective units given in Eq. (2.13) results in:

$$\begin{aligned}\hat{\mathcal{H}}^*_{FD} &= \hbar\omega^*_{eff} \sum_{n,m,\sigma} (2n + |m| + 1)\, c^\dagger_{n\,m\,\sigma}\, c_{n\,m\,\sigma} + \frac{\hbar\omega^*_c}{2} \sum_{n,m,\sigma} m\, c^\dagger_{n\,m\,\sigma}\, c_{n\,m\,\sigma} \\ \hat{\mathcal{V}}^*_c &= \sqrt{\hbar\omega^*_{eff}} \frac{1}{2} \sum_{\substack{n_1,m_1\\n_2,m_2}} \sum_{\substack{n_3,m_3\\n_4,m_4}} \sum_{\sigma,\sigma'} \langle n_1 m_1, n_2 m_2| \, \frac{l_{rel}}{r_{12}} \, |n_3 m_3, n_4 m_4\rangle \, c^\dagger_{n_1 m_1 \sigma} c^\dagger_{n_2 m_2 \sigma'} c_{n_4 m_4 \sigma'} c_{n_3 m_3 \sigma}.\end{aligned} \tag{2.19}$$

The star indicates again, that the quantity is expressed in effective Rydbergs. The appealing feature of the above equations is that the parameters ω_0, ω_c only appear as prefactors, while the matrix elements are independent of these values. In particular the different scaling of the single-particle and interaction terms with the effective confinement becomes obvious. Furthermore we note that all material constants are absorbed in the effective units. Independent of the host material, we therefore describe the eigenspectrum of the quantum dot in the absence of an external magnetic field by a single parameter that describes the effective confinement $\hbar\omega^*_0$.
In Eq. (2.19) an external magnetic field applied perpendicular to the plane of motion enters the Hamiltonian only via the cyclotron frequency $\hbar\omega^*_c \propto B$. One further parameter is needed to take into account the Zeeman term, describing the spin splitting in the magnetic field. The Zeeman splitting defined in Eq. (2.2) is given in effective units by:

$$\begin{aligned}\hat{\mathcal{H}}^*_Z &= \alpha\, \hbar\omega^*_c\, \hat{\mathcal{S}}_z \\ \alpha &= g^* m^*/(2m_0)\; .\end{aligned} \tag{2.20}$$

For (bulk) GaAs the effective Landé factor is given by $g^* = -0.44$ and we obtain $\alpha = -0.0145$.

2.2.4 Exact diagonalization

The eigenspectrum of the time-independent Hamiltonian (2.18) needs to be determined numerically. We use the method of exact diagonalization or configuration interaction [19, 21, 22, 23], alternative methods are based on Hartree-Fock calculations [24] or spin density functional theory [11].

Starting point is the stationary Schrödinger equation, that determines the eigenfunctions $|\psi\rangle$ and eigenenergies E via the eigenvalue problem:

$$\hat{\mathcal{H}}\,|\psi\rangle = E\,|\psi\rangle\,. \tag{2.21}$$

In order to calculate the eigenspectrum we reexpress this equation in an appropriate basis $|n\rangle$. Thus the Hamilton operator $\hat{\mathcal{H}}$ is transformed in a Hamilton matrix $\underline{\underline{H}}$ and the eigenfunction $|\psi\rangle$ in a vector $\underline{\psi}$, resulting in the following set of linear equations:

$$\underline{\underline{H}}\,\underline{\psi} = E\,\underline{\psi} \tag{2.22}$$

$$H_{n\,n'} = \langle n|\,\hat{\mathcal{H}}\,|n'\rangle \;;\; \psi_n = \langle n|\psi\rangle\,. \tag{2.23}$$

The eigenenergies of the stationary Schrödinger equation (2.21) are given by the eigenvalues of the Hamilton matrix and correspondingly the eigenfunctions $|\psi\rangle$ are determined from the eigenvectors $\underline{\psi}$ of Eq. (2.22) by $|\psi\rangle = \sum_n \psi_n\,|n\rangle$. In the case of a complete basis $|n\rangle$ the result is exact.

Applying this idea to the Hamiltonian (2.18) we first note that there is no finite basis for the Hilbert space corresponding to any electron number N_e, since there are already infinitely many single-particle states. In order to truncate the basis in a reasonable way, we note the following: First, we know the exact solution for the noninteracting problem, namely the Fock-Darwin spectrum introduced in Eqs. (2.3) and (2.4). Furthermore we found that according to the symmetries of the system, the number of electrons, the total angular momentum perpendicular to the plane of motion as well as the square and the z-component of the total spin are conserved. These quantities are described by the quantum numbers N_e, M, S, S_z respectively. Therefore the symmetries of the systems allow us to restrict the basis states $|n\rangle$ of Eq. (2.22) to a given subspace characterized by N_e, M, S, S_z. Furthermore we choose the basis elements as eigenstates of the non-interacting Fock-Darwin Hamiltonian and numerate them according to their (single-particle) energy. We then truncate the basis at a specific single-particle energy, calculate the Hamilton matrix for this basis and diagonalize it. The size of the matrix is chosen big enough, so that the eigenspectrum has converged, i.e. it does not change significantly by further increasing the basis size. The code was implemented by David Jacob [19].

It is very useful to take the symmetries of the system into account, because for a required precision it reduces the size of the basis, thus allowing to calculate higher particle numbers. Furthermore it allows to specify the eigenspectrum according to the conserved quantities. We note that the basis vectors to constant N, M, S_z are single Slater determinants, however basis states of constant S may include superposition of Slater determinants that only

differ in the spin degree of freedom. Technical details of the implementation of an exact diagonalization scheme can be found in references [19, 22, 23].

2.3 Coulomb effects in charge density excitations

In this section we study how charge density excitations of self-assembled dots are affected by Coulomb interaction. The calculations presented here were used to model experimental data obtained from resonant inelastic Raman scattering on InAs self-assembled quantum dots and are published together with the experimental data in references [1, 2].

The experimental realization of self-assembled dots was shortly explained in subsection 2.1 and a typical sample was shown in Fig. 2.1. The number of (conduction) electrons in the dots is controlled by the voltage applied between top and back contact and is varied from one up to six electrons. Further experimental input for our calculations are the confinement strength $\hbar\omega_0 = 50meV$ and the material constants of bulk InAs $m^* = 0.024m_0$, $\varepsilon = 15.15$. Using the effective units introduced in Eq. (2.13) and Table 2.1 this results in $Ryd^* = 1.42meV$, $a_0^* = 33.5nm$ and $\hbar\omega_0 = 35.2Ryd^*$. According to our discussion in subsection 2.2.2 we note that in this regime the Coulomb energy between any pair of electrons is always smaller than the confinement energy by at least a factor of $\sqrt{\pi}/\sqrt{\hbar\omega_0^*} \approx 0.3$.

In Raman spectroscopy the excitation energies of quantum dots are measured in a two-photon process. Roughly spoken, first the incoming laser light causes a transition from the many-particle ground state of a quantum dot to an intermediate state with an additional electron-hole pair. If after the recombination of the electron-hole pair the dot is left in an excited many-particle state, then the emitted photon is red shifted with respect to the incoming light. The energy difference between incoming and outgoing photon equals the excitation energy of the electronic many-particle state.

Polarization selection rules enable to distinguish charge density and spin density excitations in Raman spectroscopy. Charge density excitations (spin density excitations) are defined as excitations where the excited state has the same spin (has a different spin) as the ground state, and they appear in an experimental configuration where the polarizations of the incoming laser light and of the inelastically scattered photon are parallel (perpendicular) to each other.

In our calculations we use the Hamiltonian introduced in Eq. (2.18). In first quantization and without an external magnetic field it reads:

$$\mathcal{H} = \sum_{i=1}^{N} \left[\frac{p_i^2}{2m^*} + \frac{m^*}{2}\omega_0^2 \mathbf{r}_i^2 \right] + \frac{1}{2}\frac{e^2}{4\pi\epsilon\epsilon_0} \sum_{i\neq j}^{N} \frac{1}{|\mathbf{r}_i - \mathbf{r}_j|}\,, \tag{2.24}$$

The dimensionless form of the Hamiltonian was derived in Eq. (2.19) and in the absence

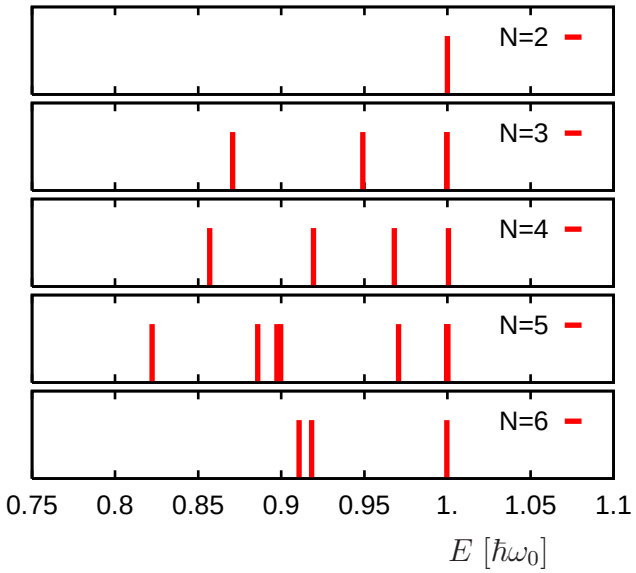

Figure 2.6: *Energetically lowest charge density excitations of a two-dimensional parabolic quantum dot occupied with N electrons. The excitation of the center of mass motion (Kohn mode) always appears at the single-particle level spacing $\hbar\omega_0$. Below the Kohn mode excitations of the relative motion arise, that are influenced by the Coulomb interaction. Parameters: $\hbar\omega_0 = 35.2 Ryd^*$*

of a magnetic field it is given by:

$$\hat{\mathcal{H}}^* := \hbar\omega_0^* \sum_{n,m,\sigma} (2n + |m| + 1)\, c^\dagger_{n\,m\,\sigma}\, c_{n\,m\,\sigma} + \tag{2.25}$$
$$+\sqrt{\hbar\omega_0^*} \sum_{\substack{n_1,m_1\\n_2,m_2}} \sum_{\substack{n_3,m_3\\n_4,m_4}} \sum_{\sigma,\sigma'} \langle n_1 m_1, n_2 m_2 | \frac{l_{rel}}{r_{12}} | n_3 m_3, n_4 m_4 \rangle\, c^\dagger_{n_1 m_1 \sigma} c^\dagger_{n_2 m_2 \sigma'} c_{n_4 m_4 \sigma'} c_{n_3 m_3 \sigma}.$$

Here the superscript $*$ again denotes that the quantity is given in units of Ryd^*. The low number of electrons confined to the dots allows to calculate the eigenspectrum by means of exact diagonalization of the Hamiltonian.

Fig. 2.6 shows the low lying charge density excitations (spin conserving excitations) from the ground state, for different numbers N of electrons confined to the dot. First, one can see that, independent of N, there is always an excitation at the confinement energy $\hbar\omega_0$, which represents the excitation of the center of mass mode (Kohn mode). However for $N > 2$ and at energies below the Kohn mode, further excitations show up, which are sensitive to the electron number and that can be identified as excitations of the relative motion. Consistent with the experimental finding Fig. 2.6 shows, that the average excitation energy shifts to lower energies if the occupation of the dot is increased, while the distribution of possible excitations becomes broader. Furthermore we note the special situation for $N = 2$ and $N = 6$ electrons confined to the dot. For two electrons on the dot there is only the center of

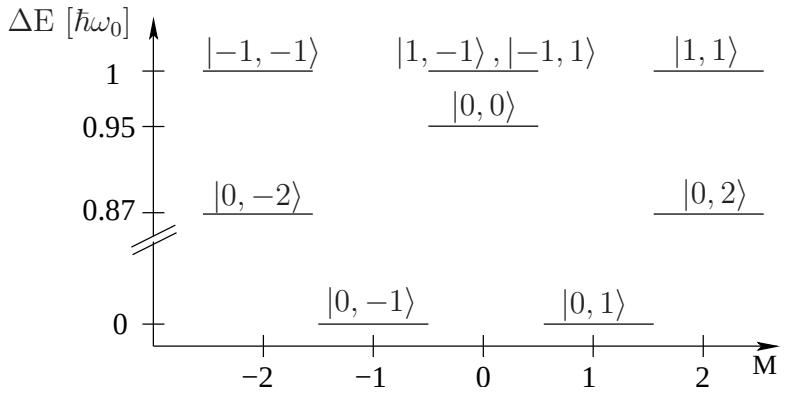

Figure 2.7: *Schematic energy differences between three-electron states with the same spin as the ground state i.e.* $S = \frac{1}{2}$, $S_z = \pm\frac{1}{2}$. *States are characterized by* $\left|M^{cm}, M^{rel}\right\rangle$, *where* M^{cm} *denotes the angular momentum of the center of mass motion and* M^{rel} *that of the relative motion. Parameters* $\hbar\omega_0 = 35.2 Ryd^*$.

mass excitation and no excitation of the relative motion and for six electrons the possible excitations have a higher average value and a smaller width than for $N = 5$. This effect is caused by the shell filling of the $n = 0, m = 0$ level for $N = 2$ and of the p-shell for $N = 6$.

The difference between excitations of the center of mass and relative motion is explainable by the Coulomb interaction, which only influences the relative motion. We argue that the excitations of the relative motion are below the single-particle excitation, since the N-particle excited state has a lower Coulomb energy than the N-particle ground state. We identify two general mechanisms that reduce the excitations of the relative motion below the center of mass or single-particle excitation. First, we note that the wavefunction of an excited state has a larger spatial extend than the ground state, since higher single-particle orbitals are occupied. This can lead to a larger distance between the electrons and thus to a lower Coulomb interaction in the excited state than in the ground state. In terms of matrix elements this fact is visible in Table 2.2 since the direct and exchange term decrease if higher orbitals are occupied. Secondly, we note that all ground states discussed here are (approximately) given by single Slater determinants, since for each subspace N, M, S, S_z there is only a single Slater determinant which minimizes the single-particle energy. Therefore the many-particle ground state cannot profit of Coulomb correlations that arise due to the superposition of different basis states. In contrast the many-particle excited states are built up by superpositions of different basis states belonging to the same subspace M, S, S_z, which all have the same single-particle energies. This allows to reduce the Coulomb energy by building up correlations, connected with the matrix elements listed in Table 2.3. In the following we discuss these mechanism in more detail for the case of three electrons.

As an example for the microscopic structure of the different excitations we discuss the case of three electrons inside the dot by means of Fig. 2.7 and 2.8 . In agreement with the single-particle picture the ground state is four-fold degenerate in the absence of a magnetic field, with angular momentum $M = \pm 1$ and spin $S = \frac{1}{2}$, $S_z = \pm\frac{1}{2}$. Its form is schematically

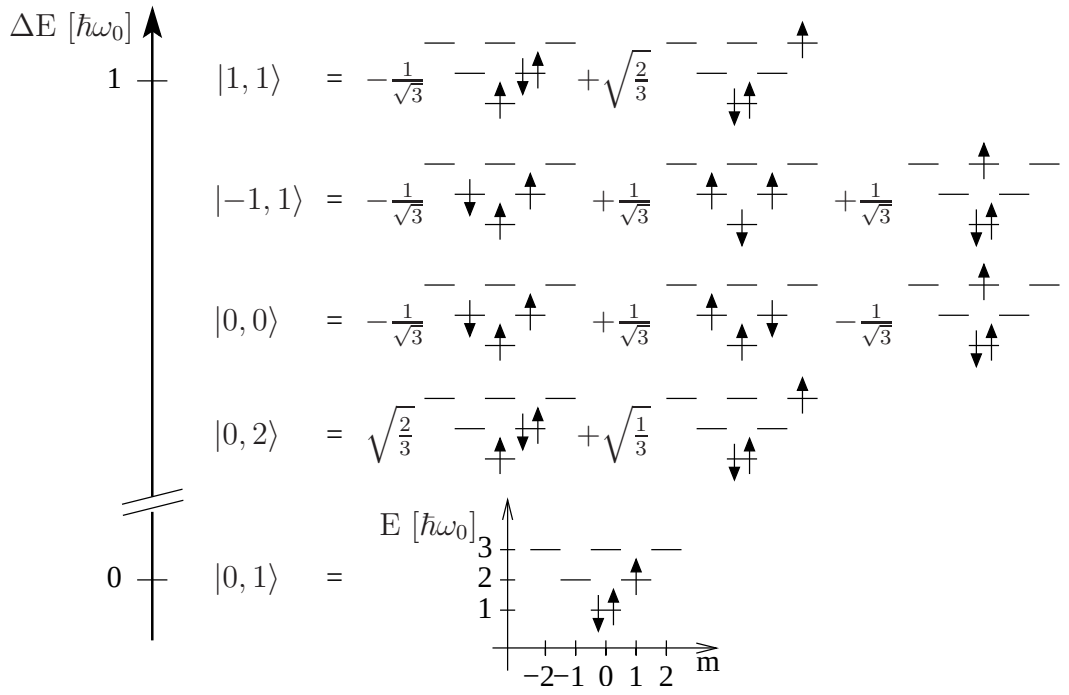

Figure 2.8: *Schematic representation of many-body wavefunction of the ground state and its lowest charge density excitations in Slater determinants of Fock-Darwin orbitals.*

depicted in Fig 2.8. In order to distinguish excitations of relative and center of mass motion we specify in Fig. 2.7 the angular momentum of the center of mass (M^{cm}) and of the relative motion (M^{rel}) and label the ground state and its lowest excitations by $\left|M^{cm},\, M^{rel}\right\rangle$. This can be done with the help of Eq. (2.12). Due to the degeneracy of the orbitals $|n, \pm m\rangle$ we find degenerate excitation spectra, either starting from $M = 1$ or $M = -1$. The lower lying excitations correspond to excitations of the relative motion with $\Delta M^{rel} = \pm 1$ while the Kohn modes have $\Delta M^{cm} = \pm 1$. We note that the effect of Coulomb interaction on the excitation spectrum discussed here will be more pronounced for weaker confinement, since the influence of the Coulomb interaction increases with decreasing confinement. While the single-particle energy in Fig 2.6 and 2.7 is given by $\hbar\omega_0^*$ the characteristic energy scale for the Coulomb interaction is $\sqrt{\hbar\omega_0^*}$, so that the ratio between Coulomb energy and single particle energy is approximately doubled if the confinement is reduced by a factor of 4.

In Fig. 2.8 we represent the form of the corresponding many-particle states by showing the dominant Slater determinants of the Fock-Darwin orbitals. For illustration we considered in Fig. 2.8 for each state only Slater determinants with the same single-particle energy which can be justified by the strong confinement energy and which is checked by proving the close agreement with the exact wavefunction obtained with a much larger basis size. The strong reduction of the basis for the many-particle states in Fig. 2.8 helps to identify the two different aspects of the Coulomb interaction. First we note that each of the two Slater determinants contributing to the lowest excited state $|0, 2\rangle$ has a lower Coulomb

energy than the ground state. This can be explained by the larger extend of these wavefunctions and by the corresponding matrix elements listed in Table 2.2. However the lowest excited state $|0,2\rangle$ has still a smaller Coulomb energy than each of its Slater determinants individually, which is explained by the Coulomb correlations arising due to the superposition of different states with same M, S, S_z. These correlations are connected with the matrix elements listed in Table 2.3. Since the ground state consists of a single Slater determinant it cannot profit of such Coulomb correlations. Following the same reasoning we understand the appearance of excitation energies below the Kohn mode for all occupation numbers $N_e > 2$.

We now comment on the special situation for $N_e = 2$, where at low energies only center of mass excitations exist. The ground state is non-degenerate and is approximated by the single Slater determinant $|0\,0\uparrow, 0\,0\downarrow\rangle$, where two electrons fill the s-shell leading to the quantum numbers $M = 0, S = S_z = 0$ and $M^{rel} = M^{cm} = 0$. In each of the subspaces $M = \pm 1, S = S_z = 0$ there is only a single charge density excitation which corresponds to $M^{rel} = 0$; $M^{cm} = \pm 1$. These center of mass excitations illustrate again the importance of the spin degree of freedom. They are well approximated by $|0\,0\downarrow, 0\pm 1\uparrow\rangle - |0\,0\uparrow, 0\pm 1\downarrow\rangle$. The Coulomb energy of such a charge density excitation is the same as in the ground state even though each of its Slater determinants has a lower Coulomb energy. The reason is, that for the singlet excited states the orbital wavefunction is symmetric which increases the Coulomb energy. It is given by the direct interaction E^c_{sp} plus the exchange term E^x_{sp} between an electron in the s-orbital and one in the p-orbital. This adds up to the direct Coulomb interaction between two electrons in the s-orbital $E^c_{sp} + E^x_{sp} = E^c_{ss}$ see Table 2.2. In contrast, the triplet state $|0\,0\downarrow, 0\pm 1\uparrow\rangle + |0\,0\uparrow, 0\pm 1\downarrow\rangle$ has an antisymmetric orbital wavefunction which decreases the Coulomb energy which is given by $E^c_{sp} - E^x_{sp}$.

2.4 Introduction to transport spectroscopy

The eigenspectrum of an interacting quantum dot is also manifest in its transport characteristics. [9] We are interested in transport experiments, where the quantum dot is weakly tunnel coupled to two contacts and furthermore electrostatically coupled to one or more side gates as illustrated in Fig. 2.9. Experimental setups are illustrated in Fig 2.2 and 2.3 in subsection 2.1. In these transport experiments electrons can only tunnel through the dot at characteristic, discrete energies determined by the eigenspectrum of the interacting dot. This has severe consequences for the current through the dot as we will show in subsection 2.4.2.

In the following subsection we will present the theoretical basics for transport spectroscopy, which are valid if the tunnel coupling is the smallest energy scale in the system.

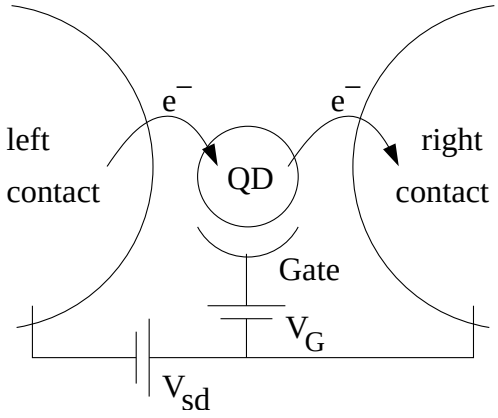

Figure 2.9: *Schematic picture of transport setup. The quantum dot is connected via tunneling barriers to a left and right contact and is electrostatically coupled to a side gate. By applying a transport voltage, V_{sd}, between source and drain contact one can push a tunnel current through the dot. A voltage V_G applied to the gate voltage tunes the electrostatic potential on the dot.*

2.4.1 Theoretical basics

Hamiltonian: The total Hamiltonian describing the system depicted in Fig. 2.9 consists of the dot Hamiltonian, H_D, the left and right contact, H_L, H_R,[1] and a term describing the tunnel coupling between dots and reservoirs, H_T [22, 25]

$$H = \underbrace{\sum_{r=\mathrm{L,R}} H_r + H_D}_{H_0} + H_T \, . \tag{2.26}$$

The contacts $H_r = \sum_{k,\sigma} \varepsilon_{kr} a^\dagger_{rk\sigma} a_{rk\sigma}$ are modeled by large reservoirs of noninteracting electrons. Here $a_{rk\sigma}, a^\dagger_{rk\sigma}$ denote the annihilation and creation operators for electrons in the reservoir $r \in \{\mathrm{L,R}\}$ with spin σ and wave vector k. Each reservoir is assumed to be in equilibrium, so that it can be characterized by the Fermi distribution $f_{\mathrm{L/R}}(\omega)$. An applied bias voltage V_{sd} is modeled by different chemical potentials in the left and right contact $\mu_L - \mu_R = eV_{sd}$. We set $\mu_L = eV_{sd}/2 = -\mu_R$ or $f_{\mathrm{L/R}}(\omega) = f(\omega \mp eV_{sd}/2)$, with $f(x) = 1/(exp(\beta x) + 1))$ and $\beta = 1/(k_B T)$.

The dot Hamiltonian, H_D, is written in its eigenbasis:

$$H_D = \sum_s E_s \left|s\right\rangle \left\langle s\right| \, . \tag{2.27}$$

The eigenspectrum has to be determined in advance, for example by an exact diagonalization approach as discussed in subsection 2.2.4. The eigenenergies of the dot are shifted

[1] We make use of a labeling appropriate for a lateral quantum dot and therefore use the notation left and right contact, however the considerations are equally valid for a vertical dot. In the latter case it is more appropriate to think of an upper and lower contact.

by the electrostatic interaction with a side gate, which is controlled by the gate voltage V_G. It is assumed that the voltage V_G applied to the side gate causes a constant electrostatic potential $V_D = \alpha V_G$ on the dot, with some proportionality factor α. This leads to $E_s(V_D) = E_s(V_D = 0) - eV_D N(s)$, where $N(s)$ describes the number of electrons of state s. The terms of the Hamiltonian (2.26) describing the dot and the contacts define the unperturbed Hamiltonian denoted by $H_0 = \sum_{r=\mathrm{L,R}} H_r + H_D$.
The Tunnel Hamiltonian H_T consists of $H^r_{T,in}$ with $r \in \{\mathrm{L}, \mathrm{R}\}$, which describes electrons hopping from the reservoir r into the dot, and of $H^r_{T,out}$ describing the opposite process:

$$H_T = \sum_{r,k,l,\sigma} t^r_{kl} a^\dagger_{rk\sigma} c_{l\sigma} + t^{r*}_{kl} c^\dagger_{l\sigma} a_{rk\sigma} = \sum_r (H^r_{T,out} + H^r_{T,in}) \; . \tag{2.28}$$

Here $c^\dagger_{l\sigma}, c_{l\sigma}$ again describe the creation and annihilation operator of a single-particle state in the quantum dot characterized by the orbital quantum number l (in our case the Fock-Darwin quantum numbers n, m) and the spin σ. Within this model the tunnel process preserves the spin orientation and the tunnel matrix elements are independent of the spin.
It is useful to reexpress the Tunnel Hamiltonian in the eigenbasis of the dot:

$$H^r_{T,out} = \sum_{k,s,s',\sigma} T^r_{k\sigma ss'} a^\dagger_{rk\sigma} P_{ss'} \tag{2.29}$$

$$H^r_{T,in} = (H^r_{T,out})^\dagger = \sum_{k,s,s',\sigma} T^{r*}_{k\sigma ss'} P_{s's} a_{rk\sigma} \tag{2.30}$$

$$T^r_{k\sigma ss'} = \sum_l t^r_{kl} \langle s | \, c_{l\sigma} \, | s' \rangle \propto \delta_{N(s)+1,N(s')} \tag{2.31}$$

$$P_{ss'} = |s\rangle \langle s'| \; . \tag{2.32}$$

The tunnel matrix elements $T^{r*}_{k\sigma ss'}$ determine the probability amplitude for a transition between the states $|s\rangle$ and $|s'\rangle$ caused by the tunneling of an electron from reservoir r described by its quantum numbers k and σ. It not only depends on the single-particle amplitudes t^r_{kl} but according to Eq. (2.31) also on the structure of the involved few-electron wavefunctions $|s\rangle$ and $|s'\rangle$.
Relevant for transport characteristics are the spectral functions $\Gamma^r_{l_1 l_2}(\omega), \Gamma^r_{s_1 s'_1 s_2 s'_2}(\omega)$ of the tunnel matrix elements, defined as:

$$\Gamma^r_{l_1 l_2}(\omega) := 2\pi \sum_k t^r_{kl_1} t^{r*}_{kl_2} \delta(\varepsilon_{kr} - \omega) \tag{2.33}$$

$$\begin{aligned} \Gamma^r_{s_1 s'_1 s_2 s'_2}(\omega) &= 2\pi \sum_{k\sigma} T^r_{k\sigma, s_1 s'_1} T^{r*}_{k\sigma, s'_2 s_2} \delta(\varepsilon_{kr} - \omega) \\ &= \sum_{l_1, l_2, \sigma} \Gamma^r_{l_1 l_2}(\omega) \langle s_1 | \, c_{l_1\sigma} \, | s'_1 \rangle \langle s'_2 | \, c_{l_2\sigma} \, | s_2 \rangle^* \; . \end{aligned} \tag{2.34}$$

Since the single-particle matrix elements are in general unknown one has to specify $\Gamma^r_{l_1 l_2}(\omega)$ by some reasonable assumption. Thereafter the structure of the many-particle eigenfunc-

tions can be taken into account exactly in the spectral function $\Gamma^r_{s_1 s_1' s_2 s_2'}(\omega)$ defined by Eq. (2.34).

Transition rates: The tunnel coupling to the external reservoirs causes transitions between many-particle states $|s\rangle, |s'\rangle$ differing in the number of electrons confined to the dot. While a more sophisticated transport theory will be presented in chapter 4 in form of a real time transport theory [26] we will now calculate the transition rate $W_{s's}$ from state $|s\rangle$ to $|s'\rangle$ applying Fermi's golden rule [25, 27, 28]:

$$\begin{aligned} W_{s's} &= \sum_r \left(W^{r+}_{s's} + W^{r-}_{s's}\right) \\ W^{r+}_{s's} &= \frac{2\pi}{\hbar}\sum_{k\sigma} \delta(E_s + \varepsilon_k - E_{s'}) \left|T^r_{k\sigma s s'}\right|^2 f_r(\varepsilon_k) \\ &= \frac{\Gamma^r_{ss's's}(E_{s'} - E_s)}{\hbar} f_r(E_{s'} - E_s) \\ W^{r-}_{s's} &= \frac{2\pi}{\hbar}\sum_{k\sigma} \delta(E_s - \varepsilon_k - E_{s'}) \left|T^r_{k\sigma s' s}\right|^2 f^-_r(\varepsilon_k) \\ &= \frac{\Gamma^r_{s'sss'}(E_s - E_{s'})}{\hbar} f^-_r(E_s - E'_s) \end{aligned} \tag{2.35}$$

Here we use the shortcut $f^-_r(\varepsilon_k) = 1 - f_r(\varepsilon_k)$. $W^{r+}_{s's}$ denotes the tunneling-in rate, connected with an electron entering the dot from reservoir r, thus causing a transition from $|s\rangle$ to $|s'\rangle$. Respectively $W^{r-}_{s's}$ denotes the tunneling-out rate, where an electron hops from the dot to reservoir r thus causing a transition from $|s\rangle$ to $|s'\rangle$. The delta function ensures the energy conservation during the tunneling process and the Pauli-factors $f_r(e_k)$, $f^-_r(e_k)$ determine the probability to find the electron or respectively the hole in the reservoir needed for the tunneling-in or tunneling-out process.

To calculate the transition rate one has to specify the spectral function $\Gamma^r_{l_1 l_2}(\omega)$. The energy dependence of the spectral function $\Gamma^r_{l_1 l_2}(\omega)$ is mainly determined by the density of states in the reservoirs. In the following we assume a constant density of states in the reservoirs and apply the random phase approximation for the tunneling matrix elements t^r_{kl} which leads to [22, 25, 28]

$$\begin{aligned} \Gamma^r_{l_1 l_2}(\omega) &= \delta_{l_1, l_2}\Gamma^r \\ \Gamma^r_{ss's's}(\omega) &= \Gamma^r \sum_{l\sigma} \left|\langle s| c_{l\sigma} |s'\rangle\right|^2 . \end{aligned} \tag{2.36}$$

Qualitatively our results do not depend on this assumption, and especially similar results are obtained for $\Gamma^r_{l_1 l_2}(\omega) = \Gamma^r$, valid for example for constant tunneling elements $t^r_{kl} = t$.

Applying Eq. (2.36) to Eq. (2.35) we get for the transition rates

$$W^{r+}_{s's} = \Gamma^r f_r(E_{s'} - E_s) \sum_{l\sigma} \left|\langle s| c_{l\sigma} |s'\rangle\right|^2 \tag{2.37}$$

$$W^{r-}_{s's} = \Gamma^r f^-_r(E_s - E_{s'}) \sum_{l\sigma} \left|\langle s'| c_{l\sigma} |s\rangle\right|^2 . \tag{2.38}$$

The meaning of the different terms is now quite intuitive. Γ_r specifies the coupling strength of the dot to contact r. The Pauli-factors $f_r(E_{s'} - E_s), f_r^-(E_s - E_{s'})$ guarantee the energy conservation of the tunneling process. A transition from $|s\rangle$ to $|s'\rangle$ defines a transport channel with its characteristic energy given by $\mu(s, s') := E_{s'} - E_s$. According to Eq. (2.37), an electron can only tunnel into the dot being in state $|s\rangle$, if there is a transport channel $\mu(s, s')$ below one of the chemical potentials of the reservoirs. Analogously an electron can only tunnel out of the dot being in state $|s\rangle$ if there is a transport channel $\mu(s, s')$, which lies above one of the electron chemical potentials μ_r of the reservoirs. While the eigenenergies of the dot determine the discrete energies of the transport channels, the form of the wavefunctions enters the spectral weight $\sum_{l\sigma} |\langle s| c_{l\sigma} |s'\rangle|^2$. In a sense it measures how well an electron entering the many-particle state $|s\rangle$ can cause a transition to $|s'\rangle$. A prominent consequence of the spectral weights is the spin blockade.[29, 30] It states that transitions between two states differing in either of the spin quantum numbers S, S_z by more than a half, i.e. $\Delta S_z, \Delta S \neq \frac{1}{2}$, are forbidden.

Master equation and current: With the help of the transition rates given in Eq. (2.37) and (2.38) we can now calculate the occupation probabilities of the many-particle eigenstates in the stationary case:

$$0 = \frac{d}{dt} P_s = \sum_{s'} \left(W_{ss'} P_{s'} - W_{s's} P_s \right) \tag{2.39}$$

$$1 = \sum_s P_s \, . \tag{2.40}$$

The first equation states that the gain rate of state $|s\rangle$, given by $\sum_{s'} W_{ss'} P_{s'}$ is the same as the loss rate $\sum_{s'} W_{s's} P_s$. The second equation guarantees probability conservation.

With the steady state probabilities P_s one can calculate the stationary current, I, through the dot:

$$I := -e \frac{dN_R}{dt} = e \sum_{s,s'} \left(W^{R+}_{s's} P_s - W^{R-}_{ss'} P_{s'} \right) \, . \tag{2.41}$$

Here N_R denotes the number of electrons in the right reservoir. Since in our convention the electron charge is $q = -e$ the current is positive if electrons flow from the left to the right reservoir, which is the case for positive transport voltage. In the stationary case the following relation holds: $\frac{dN_L}{dt} = -\frac{dN_R}{dt}$. With Eqs. (2.37), (2.39), (2.41) we are now able to calculate the stationary current through the dot, as well as the stationary occupation probabilities of its eigenstates depending on the spectrum of the dot, the applied voltages and temperature.

2.4.2 Linear and nonlinear transport

In this subsection we discuss the main aspects of how Coulomb interaction influences the transport through an interacting dot. The relevant quantities are the energies of transport

channels through the dot and the addition energies, which we define in the following. We denote the energy of the transport channel corresponding to a transition between the i-th N-electron state and the j-th $(N+1)$-electron state by:

$$\mu(N,i;N+1,j) = E(N+1,j) - E(N,i) - eV_D \ . \tag{2.42}$$

Applying a gate voltage V_G continuously changes the electrostatic potential $V_D \propto V_G$ on the dot, which is taken into account in Eq. (2.42) by the term $-eV_D$. The energy separation between consecutive ground-state channels is called addition energy $\Delta\mu(N)$:

$$\Delta\mu(N) = \mu(N,0;N+1,0) - \mu(N-1,0;N,0) \ . \tag{2.43}$$

We first discuss the regime where the applied transport voltage and the temperature are both small enough so that transitions to excited states are not possible and transport through the dot can take place only via the ground-state channels. Fig. 2.10 shows the

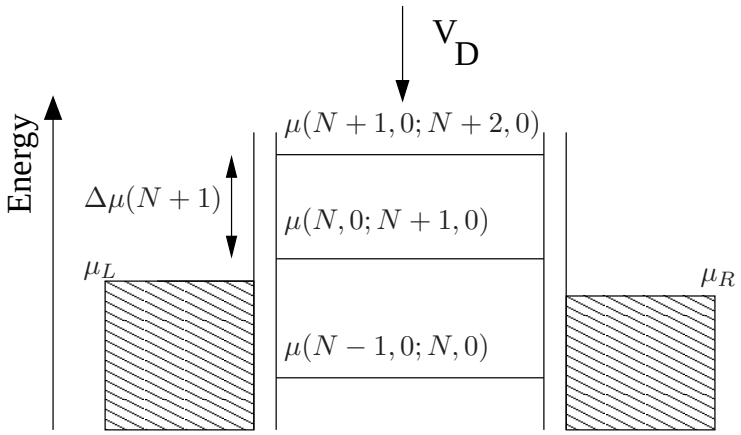

Figure 2.10: *Schematic energy profile for linear transport. The transport channels are shifted to lower (higher) energies relative to the chemical potentials of the reservoirs by increasing (decreasing) the electrostatic potential V_D on the dot. An applied transport voltage V_{sd} separates the electrochemical potentials of the reservoirs $\mu_L = eV_{sd}/2 = -\mu_R$. Consecutive ground-state channels are separated by the addition energy $\Delta\mu$. For the situation depicted here the dot is occupied by N electrons and transport is Coulomb blocked.*

energy profile for such a case. The quantum dot can only be passed via the ground-state channels which are separated in energy by the addition energy. In the situation depicted in Fig. 2.10 no ground-state channel is inside the transport window, defined by the chemical potential of the source and drain reservoir. Transport through the dot is therefore blocked and the dot is in the N-particle ground state. Increasing the electrostatic potential V_D on the dot shifts the ground-state channels to lower energies. For specific values of V_D a ground-state channel is inside the transport window and current can flow through the dot. This leads to the so called Coulomb oscillation of the current as function of the gate

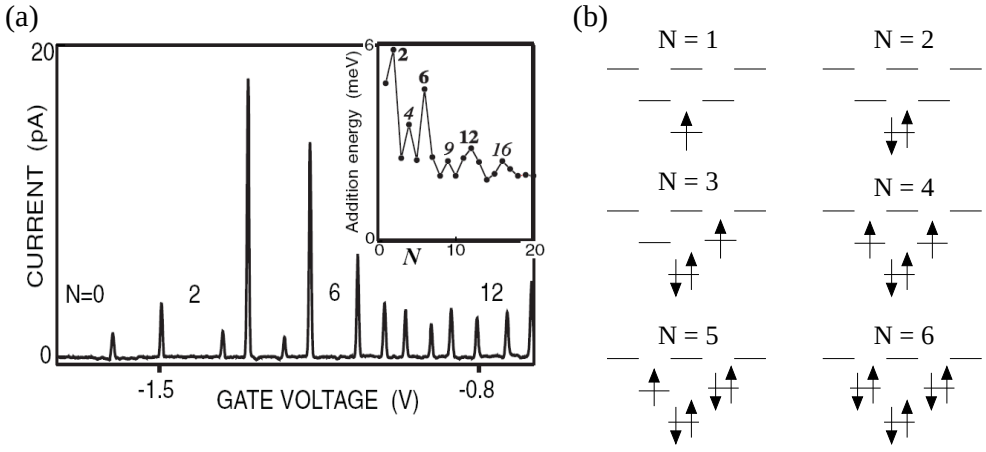

Figure 2.11: *a) Measurement of Coulomb oscillations of the current as function of the gate voltage for transport through a vertical dot. Only for specific voltages a ground-state channel is inside the transport window and a current flows through the dot. Between the current peaks transport is blocked and the number of electrons on the dot is fixed. Electron numbers corresponding to a filled shell are indicated. The inset shows the magnitude of the addition energies as function of the occupation of the dot. Data taken from reference [9]. b) Dominant Slater determinant of N-electron ground state. Schematic representation based on Fock-Darwin spectrum like in Fig. 2.8.*

voltage as shown in Fig. 2.11 a). In order to understand the dependence of the addition energy on the number of electron, we follow references [9, 12] and approximate the ground states by the dominantly occupied Slater determinant as depicted in Fig 2.11 b). Within this rough estimate we obtain the following energies of the ground-state channels:

$$\begin{aligned}
\mu(0,0;1,0) &= \varepsilon_{1s} \\
\mu(1,0;2,0) &= \varepsilon_{1s} + E^c_{ss} \\
\mu(2,0;3,0) &= \varepsilon_{1p} + 2E^c_{sp} - E^x_{sp} \\
\mu(3,0;4,0) &= \varepsilon_{1p} + 2E^c_{sp} - E^x_{sp} + E^c_{pp} - E^x_{p+p-} \\
\mu(4,0;5,0) &= \varepsilon_{1p} + 2E^c_{sp} - E^x_{sp} + 2E^c_{pp} \\
\mu(5,0;6,0) &= \varepsilon_{1p} + 2E^c_{sp} - E^x_{sp} + 3E^c_{pp} - E^x_{p+p-}
\end{aligned} \tag{2.44}$$

Here we denote the orbitals according to their angular momentum that is the s-orbital corresponds to the Fock-Darwin quantum numbers $n = 0, m = 0$ and respectively the $p\pm$-orbitals correspond to $n = 0, m = \pm 1$. The Fock-Darwin levels have the energy $\varepsilon_s = \hbar\omega_0$ and $\varepsilon_p = 2\hbar\omega_0$. The Coulomb interaction is labeled as in Table 2.2, e.g. E^c_{ss} denotes the direct Coulomb interaction between two electrons in the s-orbitals and E^x_{p+p-} the exchange interaction between an electron in orbital $p+$ and one in orbital $p-$ both with the same spin orientation. The approximated energies of the ground-state channels given in Eq. (2.44)

result in the following addition energies:

$$\begin{aligned}
\Delta\mu(1) &= E^c_{ss} \\
\Delta\mu(2) &= \varepsilon_{1p} - \varepsilon_{1s} - E^c_{ss} + 2E^c_{sp} - E^x_{sp} = \hbar\omega_0 + 0.25E^c_{ss} \\
\Delta\mu(3) &= E^c_{pp} - E^x_{p+p-} = 0.5E^c_{ss} \\
\Delta\mu(4) &= E^c_{pp} + E^x_{p+p-} = 0.875E^c_{ss} \\
\Delta\mu(5) &= E^c_{pp} - E^x_{p+p-} = 0.5E^c_{ss}\ .
\end{aligned}$$

Here we expressed all Coulomb energies by E^c_{ss} using Table 2.2. We note that the simple estimate of the addition energies reproduces the qualitative behavior of the experimental values for the corresponding addition energies depicted in Fig. 2.11. The large addition energies $\Delta\mu(2)$ and $\Delta\mu(4)$ are explained by the filling of the s-shell and by the exchange energy between the two p-electrons respectively. We note that the addition energies for $N = 3$ to $N = 5$ are exclusively determined by the Coulomb interaction, since the added electron always occupies a p-level.

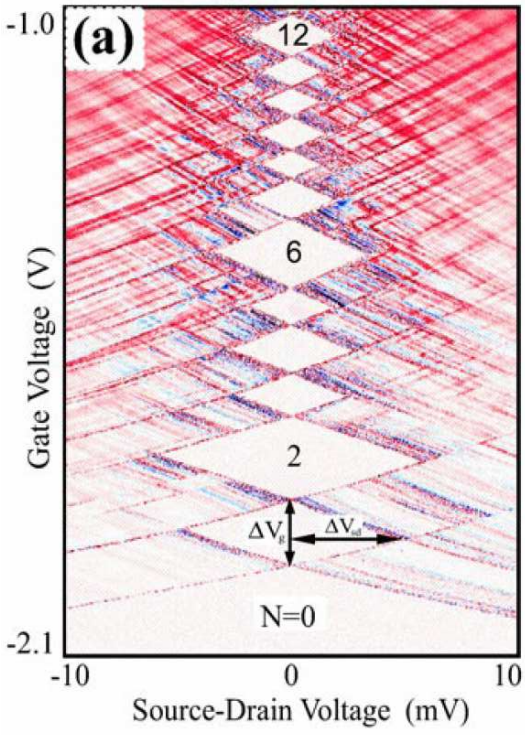

Figure 2.12: *Charging diagram for a vertical dot. dI/dV_{sd} is plotted as function of source-drain voltage V_{sd} and gate voltage V_G. White regions centered around zero transport voltage show the Coulomb diamonds, where the number of electrons on the dot is fixed and current is Coulomb-blocked. Red color indicates positive dI/dV_{sd}, while blue regions indicate negative dI/dV_{sd}. Data taken from reference [9].*

While the signals in the linear transport regime correspond to ground-state transitions, the excitations of the dot spectrum can be studied in the nonlinear response regime. In the nonlinear regime the current increases in form of a Coulomb staircase as function of the transport voltage.[7] Steps in the current arise whenever a further (allowed) transport channel enters the transport window. The linear and nonlinear transport spectra can

be combined in a so-called charging diagram, where either the current or the differential conductance is plotted as function of transport and gate voltage. [9, 31, 32, 33] An example for a charging diagram showing the differential conductance through a vertical dot is given in Fig. 2.12. Centered around zero transport voltage, the Coulomb blockade gives rise to Coulomb diamonds, where the current is blocked and the number of electrons on the dot is fixed. The Coulomb diamonds are limited by the resonances of the ground-state channels with either the source or drain chemical potential giving rise to a peak in the differential conductance and a step in the current. Outside the Coulomb diamonds the excitation spectrum of the dot becomes visible as lines parallel to the ground-state channels.

In the next section we discuss a blocking mechanism for the current through the dot which leads to an extension of the third Coulomb diamond. The mechanism is based on transitions to excited states. With the discussion presented in this subsection we therefore already know that it will be restricted to weak confinement, due to the following reasoning. The magnitude of the third Coulomb diamond is given by the addition energies $\Delta\mu(3)$ which is determined by the interaction on the dot as shown in Eq. (2.45). Since the Coulomb interaction scales like $\sqrt{\omega_0}$, the magnitude of the Coulomb diamonds will be small (large) compared to the excitation energies for $\hbar\omega_0 \gg 1Ryd^*$ ($\hbar\omega_0 \ll 1Ryd^*$).

2.5 Complete blocking of nonlinear transport

The most prominent selection rule for transport through quantum dots is the spin selection rule, stating that transitions are forbidden between two states differing in either of the spin quantum numbers S, S_z by more than a half. [29, 34, 35] If a ground-state channel is spin-blocked, the conductance peak in the linear transport regime, corresponding to this transition is absent and the Coulomb diamonds in the charging diagram are not closed at zero transport voltage. Experimentally such a behavior was found recently in transport through a lateral quantum dot. [30] Furthermore spin-blocking of energetically higher lying transport channels can lead to the appearance of negative differential conductances in the nonlinear transport regime and even to the complete disappearance of the current. This effect is theoretically discussed for a square-shaped dot and a colloidal nanocrystal in references [29, 34, 35] and [22], respectively, and experimentally observed in references [30, 36]. Furthermore recent theoretical work on molecular electronics shows that this effect is not restricted to quantum dots but it is also predicted for transport through charge-switchable molecular magnets. [37] Related work includes nonlinear transport spectra through interacting one-dimensional wires, where also negative differential conductances arise due to spin blockade. [34, 38, 39] It is crucial to note that the appearance of eigenstates with large spin in the low excitation spectrum is a many-particle effect, like the exchange interaction and can therefore not be found in simple constant interaction models.

In the following we discuss a blocking mechanism for the case of a parabolic quantum dot weakly coupled to external electron reservoirs. A parabolic dot is especially suited to study the dependence of the blocking mechanism on the confinement potential and on the

strength of the magnetic field, since the single-particle spectrum can be solved analytically and the dependence of the excitation spectrum and the addition energy on confinement and magnetic field are well understood.

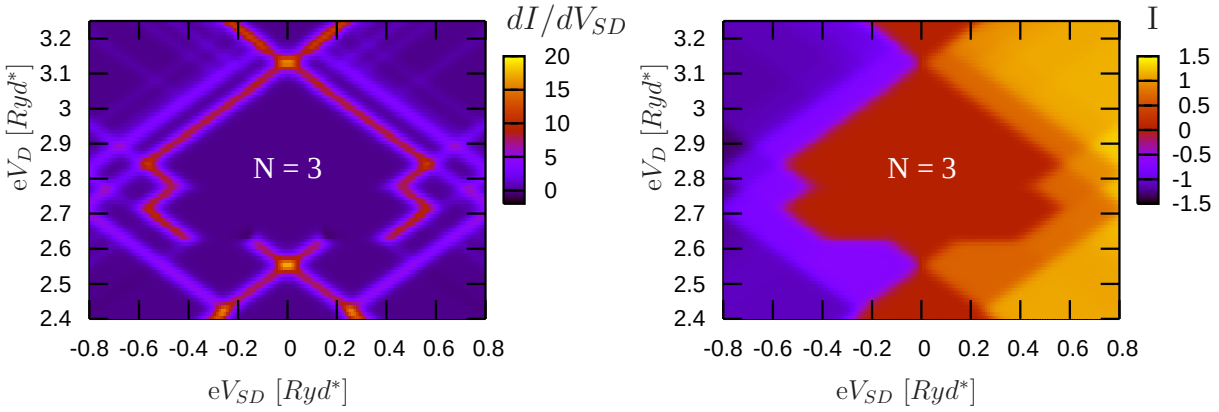

Figure 2.13: *Charging diagram of differential conductance (left) and stationary current (right) through a two-dimensional parabolic dot. Due to blocking mechanism transport through ground-state channel disappears for* $2.62Ryd^* \leq eV_D \leq 2.78Ryd^*$ *leading to an extension of the Coulomb diamond. Current given in units* $[\Gamma e/\hbar]$ *and differential conductance in* $[\Gamma e^2/(Ryd^*\hbar)]$*. Parameters:* $\hbar\omega_0 = 0.6Ryd^*, \hbar\omega_c = 0Ryd^*$, $kT = 0.01Ryd^*$, *symmetric coupling is assumed.*

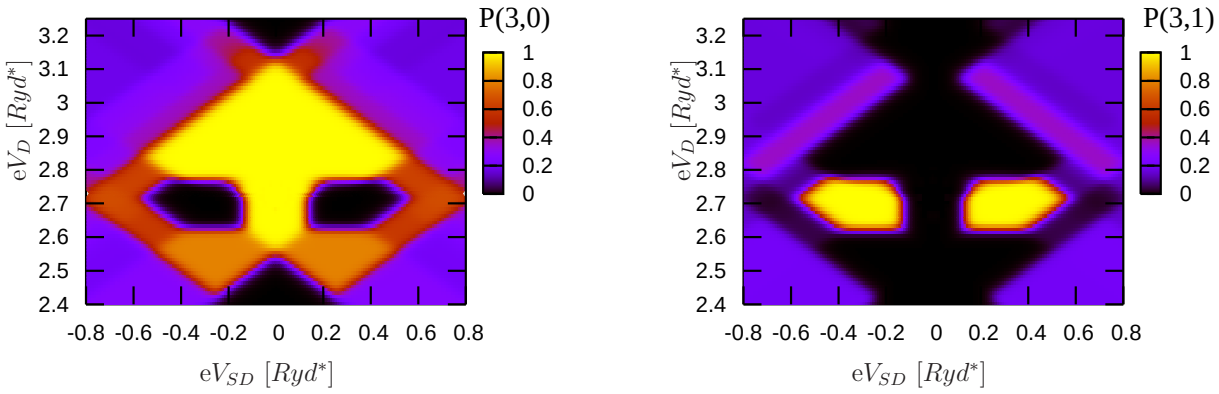

Figure 2.14: *Occupation probabilities for three-electron ground state (left) and first excited state (right). In the regime where the blocking is active (see Fig. 2.13) the dot is always in state* $|3,1\rangle$. *Same parameters as in Fig. 2.13*

.

Fig. 2.13 illustrates an example of the blocking mechanism in a (gate) voltage regime where the dot is preferably occupied by three electrons. If the electrostatic potential V_D on the dot ranges between $2.62Ryd^* \leq eV_D \leq 2.78Ryd^*$ the Coulomb diamond is extended to transport voltages, where already the ground-state channel $\mu(2,0;3,0)$ is inside the transport window. As illustrated on the left side of Fig. 2.13, the conductance peak

- corresponding to the resonance of the ground-state channel with the electrochemical potential in the drain reservoir (lower electrochemical potential) - is interrupted in this gate voltage regime and transport is only allowed at higher transport voltages[2].

Fig. 2.14 shows the occupation probabilities of the ground (left) and first excited (right) three-particle state. Inside the Coulomb diamond the dot is not always in the ground state as expected, but there is also a region where the dot is exclusively in the first excited state. It is just this region where blocking of transport occurs.

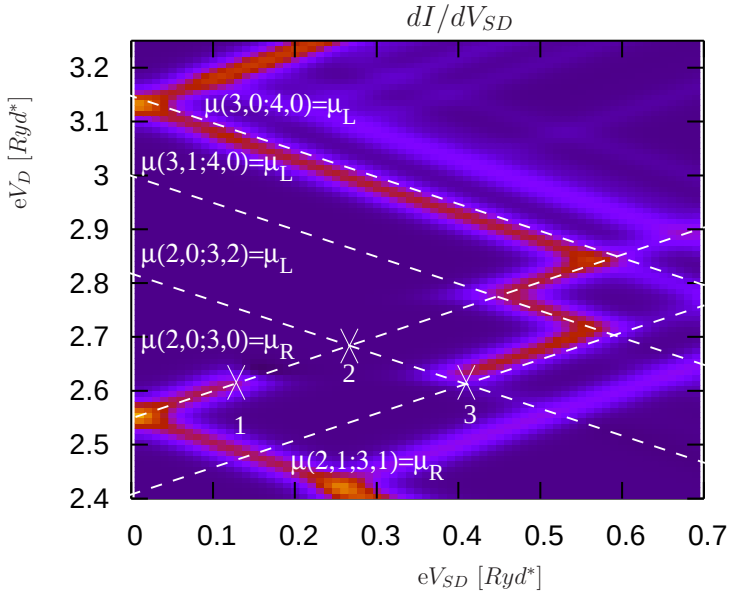

Figure 2.15: *Differential conductance as function of V_D and V_{SD} (same as in Fig. 2.13). Resonances of relevant transport channels with electrochemical potentials in the reservoirs are indicated. The transport channel $\mu(2,1;3,2)$, which is nearly degenerate with the ground-state channel $\mu(2,1;3,2) \approx \mu(2,0;3,0)$, is not shown here.*

In order to understand the blocking mechanism we indicate by dashed lines in Fig. 2.15 the resonances of the relevant transport channels with the electrochemical potentials of the reservoirs. Furthermore three characteristic points for the blocking mechanism are marked by crosses in the charging diagram. The transport properties at these points will be discussed in the following. Since we assume symmetric tunneling barriers the charging diagram depicted Fig. 2.15 is symmetric with respect to $V_{sd} = 0$.

The relevant states participating in the blocking mechanism are characterized in Table 2.4 (a). As indicated in Table 2.4 (b) the spin polarization of the first excited three-particle state leads to a spin blockade of the channel $\mu(2,0;3,1)$. There is a close degeneracy

[2]The blocking mechanism is completely determined by the states listed in Table 2.4, since further transport channels cannot cancel the blocking mechanism (by providing an exit channel in the relevant voltage regime). Our calculations do however also include the two lowest four electron excitations, to account for additional structures in the charging diagram. Adding further transport channels will only lead to new conductance peaks further outside the Coulomb diamond.

	$\|2,0\rangle$	$\|2,1\rangle$	$\|3,0\rangle$	$\|3,1\rangle$	$\|3,2\rangle$	$\|4,0\rangle$
M	0	±1	±1	0	±2	0
S	0	1	0.5	1.5	0.5	1
E[Ryd^*]	2.170	2.431	4.731	4.837	4.989	7.861

(a)

	$\|2,0\rangle$	$\|2,1\rangle$	$\|4,0\rangle$
$\|3,0\rangle$	✔	✔	✔
$\|3,1\rangle$	✘	✔	✔
$\|3,2\rangle$	✔	✔	✔

(b)

Table 2.4: (a): Characterization of relevant eigenstates for $\hbar\omega_0 = 0.6Ryd^*$, $\hbar\omega_c = 0$. (b): Indication of allowed (✔) and forbidden transitions (✘).

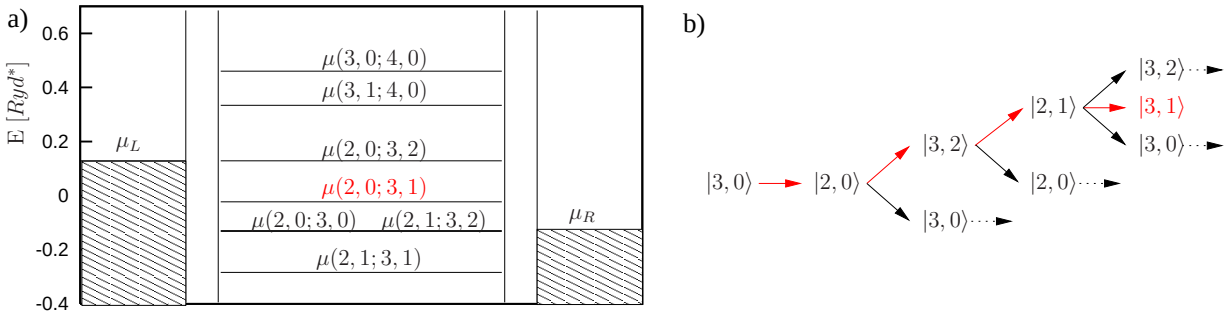

Figure 2.16: *a) Schematic energy diagram including the transport channels relevant for blocking mechanism. Voltages are chosen according to point 2 in Fig. 2.15. b) Possible transitions for the situation depicted in a). Cascade indicated by red arrows describes a possible entrance to state* $|3,1\rangle$*, while the exit from this state is spin-blocked. This leads to an exclusive occupation of* $|3,1\rangle$ *and to a complete suppression of the current.*

between the excitation energies $E(2,1) - E(2,0)$ and $E(3,2) - E(3,0)$, which results in $\mu(2,0;3,0) \approx \mu(2,1;3,2)$. Since all Coulomb matrix elements scale equally with the confinement strength like $\sqrt{\omega_0}$, this close degeneracy is true for the whole range of confinement strengths $0.4Ryd^* < \hbar\omega_0 < 1Ryd^*$, which is considered in this subsection.

Fig. 2.16 a) shows the energy profile at point 2 of Fig 2.15. One notices that the ground-state channel $\mu(2,0;3,0)$ is in resonance with the right (drain) chemical potential, so that electrons can hop from the left reservoir onto the dot and to the right reservoir. Nevertheless the stationary current is completely suppressed and the corresponding peak in the differential conductance is missing in Fig. 2.15. This can be explained by a complex interplay between different transport channels that leads to an exclusive occupation of state $|3,1\rangle$ as illustrated in Fig. 2.16 b).

Fig. 2.16 b) shows a possible entrance to the three-electron first excited state, via the cascade of transitions depicted in red. However being in state $|3,1\rangle$ the only energetically allowed transition is spin blocked namely $\mu(2,0;3,1)$. The other transport channels for leaving state $|3,1\rangle$ are not available due to Pauli-blocking. Only at higher voltages an exit from state $|3,1\rangle$ is allowed and current flows again. This happens for example when $\mu(2,1;3,1)$ enters the transport window (conductance line starting at point 3 in Fig. 2.15).

Another exit opens via occupation of the four-electron ground state using the transport channel $\mu(3,1;4,0)$.

The reason for the blocking mechanism to start already at point 1 in Fig. 2.15 rather than at point 2, is the finite temperature. The bottleneck for going through the cascade depicted in Fig. 2.16 b) is channel $\mu(2,0;3,2)$, which has a transition rate proportional to $f_L(\mu(2,0;3,2))$. Thus the entrance rate to state $|3,1\rangle$ is limited by the factor $f_L(\mu(2,0;3,2))$. Respectively the exit rate from state $|3,1\rangle$ is limited by $1-f_R(\mu(2,1;3,1))$, corresponding to an exit via channel $\mu(2,1;3,1)$. From point 1 in Fig. 2.15 onwards the entering rate is stronger than the exit rate so that the blocking is active.

The extension of the Coulomb diamond due to the described blocking mechanism depends on the relative position of the transport channels depicted in Fig. 2.15. The two relevant energy differences are $\mu(3,1;4,0) - \mu(2,0;3,2)$, and $\mu(2,0;3,0) - \mu(2,1;3,1)$. $\mu(3,1;4,0) - \mu(2,0;3,2)$ determines the voltage range in which the conductance line - corresponding to the resonance of the ground-state channel $\mu(2,0;3,0)$ with the drain reservoir - is interrupted. While the channel $\mu(2,0;3,2)$ enables the cascade depicted in Fig. 2.16 b) and thus switches on the blocking mechanism, the entrance of channel $\mu(3,1;4,0)$ in the transport window provides an alternative, allowed exit from state $|3,1\rangle$ and hence cancels the blocking.

Similarly, $\mu(2,0;3,0) - \mu(2,1;3,1)$ determines the extension of the Coulomb diamond to higher source drain voltages (distance between points 2 and 3 or points 1 and 3 in Fig. 2.15). The entrance of channel $\mu(2,1;3,1)$ in the transport window also allows an exit from state $|3,1\rangle$ and hence again cancels the blocking.

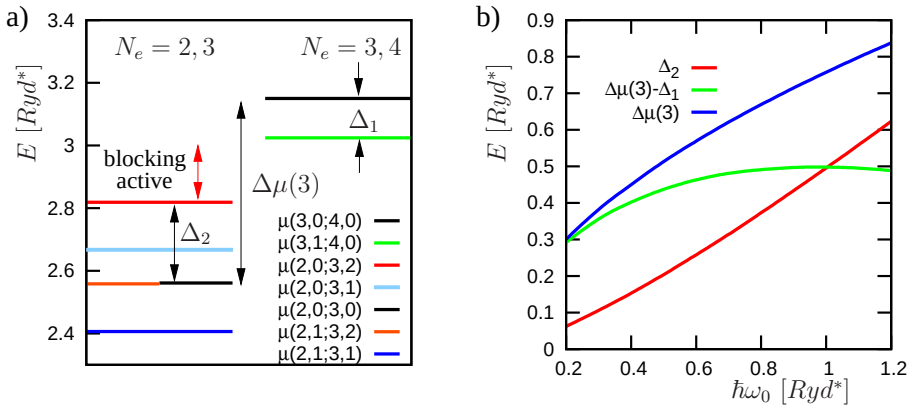

Figure 2.17: *a) Energy profile of transport channels relevant for blocking mechanism. With the entrance of the red channel in the transport window the blockade is switched on until also the green channel enters the transport window, which cancels the blocking. Parameters:* $\hbar\omega_0 = 0.6 Ryd^*$, $\hbar\omega_c = 0$. *b) Regime where the blocking is active is given by energy distance between red and green transport channel. This region shrinks with increasing confinement.*

These two characteristic energy differences can be manipulated by different means. The distance $\mu(3,1;4,0) - \mu(2,0;3,2) = \Delta\mu(3) - \Delta_1 - \Delta_2$ depends on the addition energy

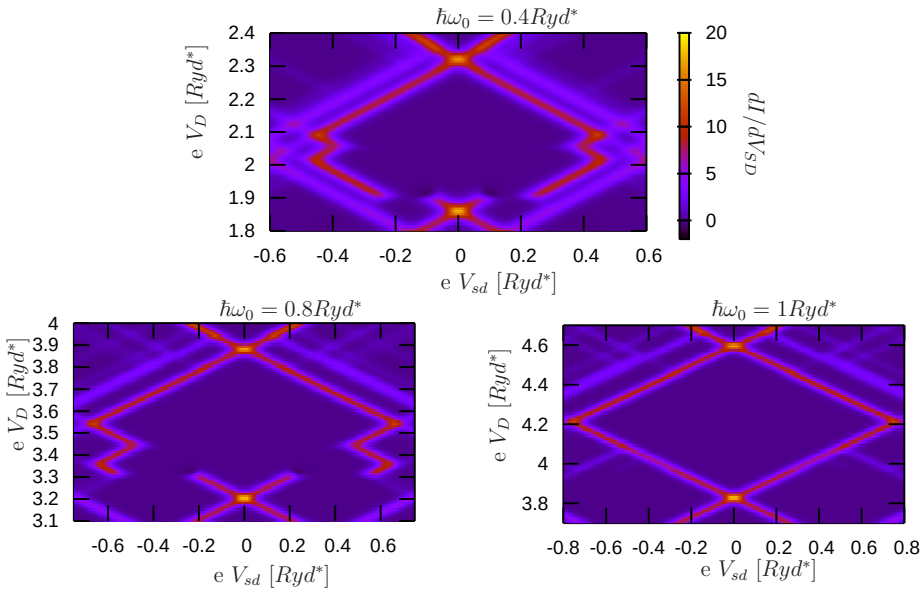

Figure 2.18: *Charging diagrams for different confinement strengths, in the absence of magnetic field. With increasing confinement the regime where the blocking is active becomes smaller, until it disappears for $\hbar\omega_0 > 1Ryd^*$ in agreement with Fig. 2.17. Scale of differential conductance is the same in all plots. Parameters: $kT = 0.01Ryd^*$, differential conductance in units of $\Gamma e^2/(Ryd^*\hbar)$.*

$\Delta\mu(3) = \mu(3,0;4,0) - \mu(2,0;3,0)$ as well as on the excitation energies $\Delta_1 = E(3,1) - E(3,0)$ and $\Delta_2 = E(3,2) - E(3,0)$. Fig. 2.17 a) illustrates the impact of Δ_1, Δ_2 and $\Delta\mu(3)$ on the order of the transport channels. As discussed at the end of subsection 2.4.2 the excitations Δ_1 and Δ_2 grow faster with increasing confinement than the addition energy $\Delta\mu(3)$. Consequently the regime where the blocking is active is therefore reduced with increasing confinement as illustrated in Fig. 2.17 b). For a confinement stronger than $\hbar\omega_0 \approx 1$ the blocking disappears completely. This behavior is demonstrated in Fig. 2.18 showing charging diagrams for different confinement potentials.

The other relevant energy, namely $\mu(2,0;3,0) - \mu(2,1;3,1)$, only depends on excitation energies and can be manipulated by a magnetic field applied perpendicularly to the plane of motion. In a magnetic field the degeneracy of the states listed in Table 2.4 (a) is canceled, mainly due to the orbital Zeeman splitting (which is much larger than the Zeeman splitting for the spin degree of freedom), which favors large negative angular momenta. For small and intermediate magnetic fields $\hbar\omega_c < \hbar\omega_0$ the three-electron ground state has $M = -1$ and the two-electron ground state has $M = 0$, respectively, while the blocking state is characterized by $|N_e = 3, M = 0, S = 1.5\rangle$. An exit from the blocking is possible via the exit channel μ_{exit} corresponding to a transition from $|N_e = 3, M = 0, S = 1.5\rangle$ to $|N_e = 2, M = -1, S = 1\rangle$. Figure 2.19 a) illustrates the magnetic field dependence of groundstate channel $\mu(2,0;3,0)$ and the exit channel. One finds that the extension of the Coulomb diamond to higher transport voltages reduces with increasing magnetic fields and for a confinement of $\hbar\omega_0 = 0.6Ryd^*$ it disappears for $\hbar\omega_c > 0.16Ryd^*$. This behavior is

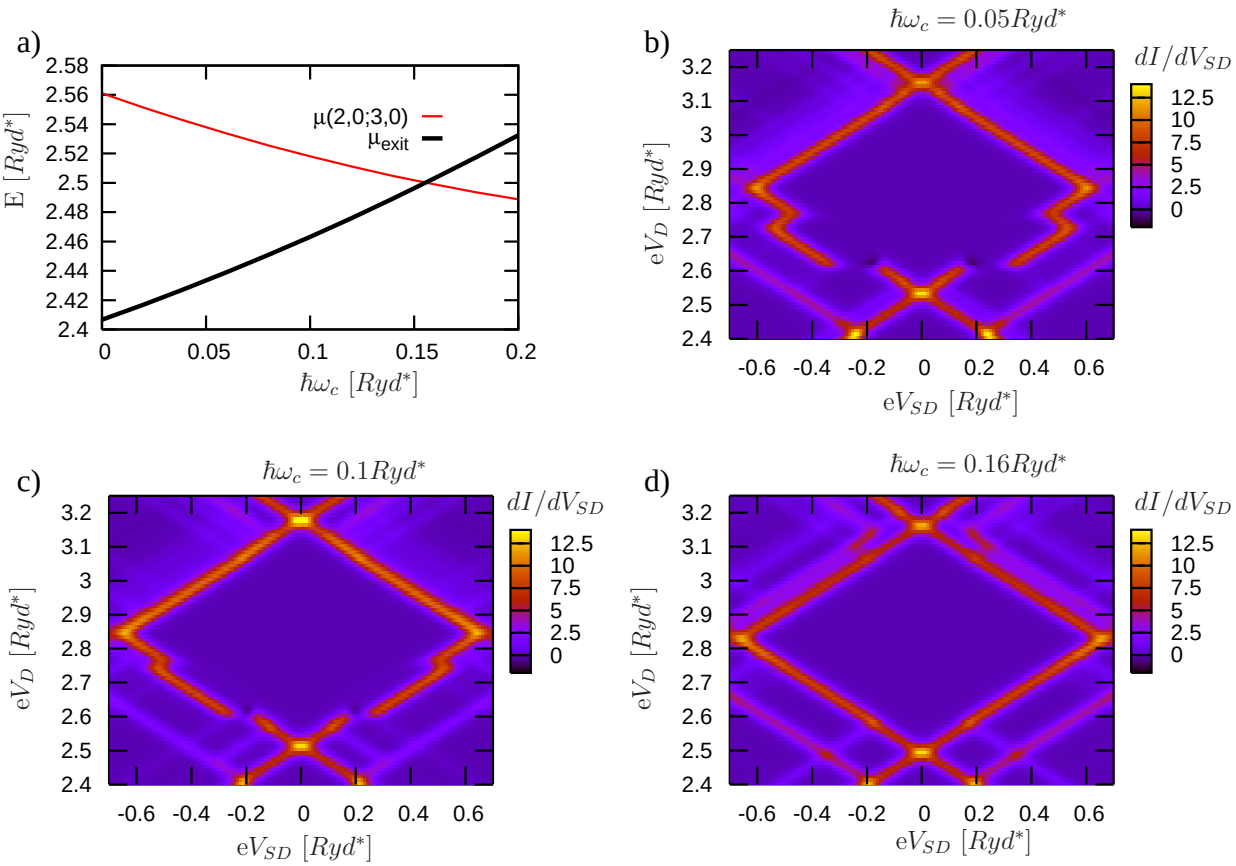

Figure 2.19: *Magnetic field dependence of blocking mechanism. a) As long as the exit channel (black line) is below the ground-state channel (red line) there is a blockade region in transport. This region shrinks with increasing magnetic field and disappears for* $\hbar\omega_c > 0.16 Ryd^*$. *The disappearance of the blocking mechanism with increasing magnetic field is shown in Figs. b)-d). Parameters:* $\hbar\omega_0 = 0.6 Ryd^*$, $kT = 0.01 Ryd^*$, *differential conductance given in units of* $\Gamma e^2/(Ryd^*\hbar)$.

demonstrated in Fig. 2.19 b)-d) showing charging diagrams for different magnetic fields.

Finally we briefly discuss the influence of energy relaxation in the dot, which was neglected up to now. According to Fig. 2.16 (b) the transition to the spin polarized state requires an intermediate occupation of excited states. Energy relaxation within the dot will therefore reduce the entrance rate to the spin-polarized state. In particular some of the excitations have a lower lying state of the same spin, so that only orbital relaxation is needed, which is supposed to be faster than the average time between consecutive tunneling processes. [40] However, the blocking of current persists if the ratio between the effective entrance rate and the exit rate continues to be larger than 1. Since the suppression of the exit rate is based on a spin blockade and the spin lifetime is known to be much longer than the average tunneling time, we expect that signatures of the blockade will survive even in the presence of relaxation. This is in agreement with experimental transport data of a dot containing

about 50 electrons. [36]

2.6 Conclusion

In this chapter we studied the influence of Coulomb interaction on the excitation spectrum and the transport properties of a quasi two-dimensional parabolic quantum dot. We obtain the eigenspectrum of the dot by diagonalizing its few-electron Hamiltonian, so that the Coulomb interaction on the dot is fully taken into account.

As a first example we use our numerically calculated spectra to study charge density excitations of a self-assembled quantum dot for different numbers of electrons confined to the dot. For charge density excitations ground state and excited states coincide in the spin degree of freedom. We show that the Coulomb energy of the ground state is always larger or equal to the Coulomb energy of excited states (with the same spin as the ground state). Therefore charge density excitations emerge below the single particle or center of mass excitation, due to the Coulomb interaction on the dot. The presented calculations explain recently measured Raman spectra for self-assembled dots.

In a second application of numerically calculated few-electron spectra we study the transport characteristics of a dot connected to external contacts. We consider the limit of weak external coupling and assume that the eigenspectrum of the dot is unaffected by the external coupling. We find that for weak lateral confinement where the Coulomb interaction exceeds the single particle energy a blocking mechanism occurs, that completely suppresses the nonlinear current through the dot. The presented current blockade can be switched on and off by sweeping the magnetic field.

3 Few-electron vertical double dots

While single quantum dots are often called artifical atoms, double dots build the simplest artifical molecule and allow detailed studies on few-particle molecular physics. The appealing feature is again the full experimental control over the number of confined electrons, the interatomic distance as well as the confinement potential of these systems. Furthermore an external magnetic field strongly influences the eigenspectrum and induces characteristic ground state transitions. The analog of such transitions in real molecules would require magnetic fields of the order of 10^6 Tesla.

A particularly interesting realization of double dots are two vertically-coupled quantum dots, since they can be produced nominally identical and with a high degree of cylindrical symmetry [41, 42]. Furthermore their occupation with electrons can be precisely controlled by a side gate voltage with allows to charge the double dot one by one starting from the empty double dot. In addition to their importance for the study of molecular physics, vertical double dots are considered as building block of a quantum computer [43, 44, 45] and they are the few electron analog of a coupled bilayer Quantum Hall system [46].

In vertically coupled double quantum dots the molecular binding for a single electron is determined by the vertical degree of freedom, while the lateral degree of freedom reflects the physics of the single dots or quasi-atoms building up the molecule. The additional vertical degree of freedom enriches the physics by interdot tunneling and the separation of the Coulomb interaction in intra- and interdot contributions. Many interesting effects arise from the competition between interdot tunnel-coupling and the Coulomb interaction. The former favors the occupation of only symmetric wavefunctions, and thus an uncorrelated wavefunction in z-direction. In contrast the Coulomb interaction prefers to occupy also antisymmetric wavefunctions in order to build up correlations between the electrons that maximize their mutual distance. This competition between interdot tunnel-coupling and Coulomb interaction leads to a qualitatively different behavior for strongly tunnel-coupled or weakly tunnel-coupled dots. Theoretical studies of the many-particle spectrum, molecular phase diagrams, and transport properties of vertical double dots as function of the interdot coupling can be found in references [47, 48, 49, 50, 51, 52]. Recent experimental studies of molecular phases in vertically coupled double dots as function of interdot tunneling, electron number and magnetic field are given in references [53, 54, 55, 56, 57, 58].

In this chapter we study the many-particle spectrum and the transport properties of a vertically coupled double dot containing few electrons. Therefore we first shortly describe the experimental realization of these systems in section 3.1. Then, in section 3.2 we introduce the theoretical model and discuss the single-particle and many-particle terms of the Hamiltonian of the double dots. The results are then presented in sections 3.3 and 3.4. In

section 3.3 we show that Coulomb correlations can lead to a spontaneous charge polarizations of the three-electron ground state, which is tunable by a magnetic field applied in vertical direction. We study in detail the mechanism leading to this spontaneous charge polarization and determine its dependence on the system parameters. In section 3.4 we then show consequences of the spontaneous polarization for transport spectra through the double dot. In a serial transport geometry the selective charge-polarization of the three-electron ground state leads to a blocking mechanism which is identified as a pseudospin-blockade, where the pseudospin labels the vertical degree of freedom. Some of the main results of this chapter have been published in references [3, 4].

3.1 Experimental realization

The double dots we study in this chapter are realized in a vertical geometry transistor as depicted in Fig. 3.1. It consists of a submicron cylindrical mesa incorporating a $GaAs/Al_xGa_{1-x}As/In_yGa_{1-y}As$ triple barrier structure surrounded by a single side gate which allows to control the number of electrons confined to the double dot [41, 42]. The geometrical lateral diameter of the mesa is about 0.56μm, however, the typical lateral extension of the few-electron wavefunction is only about $100 - 200$nm [54, 55]. The rotationally symmetric lateral confinement can well be modeled by a parabolic confinement, with a typical confinement $\hbar\omega_0$ ranging between $3meV$[57] up to $5meV$ [58].

The vertical extension of the wavefunction is determined by the triple barrier structure and is much smaller than the vertical one. It is often modeled by a double well potential as depicted in Fig. 3.1, where the thickness of the interdot barrier b determines the tunnel splitting Δ_{sas} between symmetric and antisymmetric wavefunction in z-direction and the width w of the potential wells determines the energy splitting to higher subbands of the vertical motion. Typical values are $w \approx 12nm$ and $2.5nm < b < 7.5nm$. Since the vertical extension of the wavefunction is much smaller than the lateral one only the lowest subband of the vertical potential is occupied, thus restricting the vertical degree of freedom to the lowest symmetric and antisymmetric wavefunction, splitted in energy by Δ_{sas}. Δ_{sas} decreases exponentially with the interdot distance and has values from $\Delta_{sas} \approx 0.1meV$ for $b = 7.5nm$ up to $\Delta_{sas} \approx 3.5meV$ for $b = 2.5nm$ [57, 58].

In many experiments the sample is subject to a magnetic field applied in z-direction, i.e. parallel to the symmetry axes of the double dot. The magnetic fields applied in these experiments reach up to $12T$ [57] and the samples are cooled down to about $100mK$.

The eigenspectrum of the double dot is studied by transport spectroscopy, i.e. by measuring the current I_d flowing from the substrate to the top contact in response to the applied transport voltage V_{sd}, see section 2.4. We will discuss the transport properties in subsection 3.4.

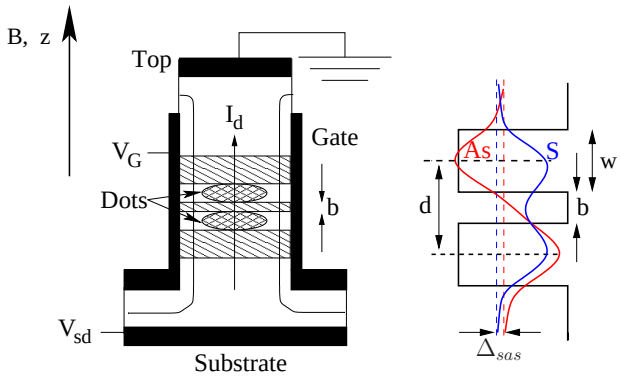

Figure 3.1: *(a) Schematic picture of the double dot device. Dots are defined in vertical direction by a triple barrier structure made of AlGaAs and InGaAs [53, 59] and laterally by the size of the mesa and the voltage applied to the side gate. Current can be pushed through the double dot by applying a source drain voltage V_{sd} between top contact and substrate. Additionally the occupation on the double dot can be controlled by tuning the gate voltage V_G applied to the side gate. An external magnetic field B is applied in z-direction. (b) Schematic single electron wavefunction in z-direction in the triple barrier structure characterized by the width of the wells w and the width of the central barrier b. Interdot tunneling leads to a level splitting between symmetric and antisymmetric wavefunctions given by Δ_{sas}.*

3.2 Model and Hamiltonian

In the vertical double dot structures introduced above, the confinement in both dots is in good approximation the same and one can separate the vertical and lateral degree of freedom in the single-particle Schrödinger equation. In analogy to the case of the single dot, a rotationally symmetric parabolic confinement potential is assumed for the lateral motion. The parabolic confinement and the perpendicular magnetic field determine the lateral motion and are described by the Fock-Darwin Hamiltonian $\hat{H}_{FD}$ given in Eq. (2.1). The magnetic field splits the spin degeneracy due to the Zeeman term $\hat{H}_Z$ given in Eq. (2.2). The vertical motion of a single electron in the double dot is determined by the interdot tunneling $\hat{H}_T$ and a possible asymmetry $\hat{H}_{As}$ between the energy levels of the upper and lower dot, as e.g. caused by a voltage drop between the dots. We describe the vertical motion within the layer model, thus restricting it to two δ-sheets separated by the interdot distance d. This approximation is justified due to the much larger vertical than lateral confinement. An estimate for an appropriate interdot distance d is given by the distance between the wavefunction maxima of the vertical wavefunction in the real structure and is given by $d \approx b + w$ as indicated in Fig. 3.1.
The single-particle Hamiltonian $\hat{H}$ has thus the following form:

$$\hat{H} = \hat{H}_{FD} + \hat{H}_Z + \hat{H}_T + \hat{H}_{As}\,. \tag{3.1}$$

If more than one electron is confined to the double dot, the Coulomb interaction $\hat{\mathcal{V}}_c$ between

different electrons has to be included. Therefore the many-particle Hamiltonian $\hat{\mathcal{H}}$ has the following form:

$$\begin{aligned}\hat{\mathcal{H}} &= \hat{\mathcal{H}}_{FD} + \hat{\mathcal{H}}_T + \hat{\mathcal{H}}_{As} + \hat{\mathcal{H}}_Z + \hat{\mathcal{V}}_c \\ &= \sum_{i=1}^{N_e} \left(\hat{H}_{FD}^{(i)} + \hat{H}_T^{(i)} + \hat{H}_{As}^{(i)} + \hat{H}_Z^{(i)} \right) + \frac{1}{\kappa}\frac{1}{2} \sum_{i,j=1}^{N} \hat{V}_C^{ij} \,, \end{aligned} \tag{3.2}$$

Here $\kappa = (4\pi\varepsilon_0\varepsilon_r)/\varepsilon^2$ and $\hat{V}_c^{i,j}$ denotes the inverse relative distance between two electrons. The tunneling Hamiltonian $\hat{\mathcal{H}}_T$ and the possible asymmetry $\hat{\mathcal{H}}_{As}$ are given in the following subsection.

3.2.1 Pseudospin

According to the layer model we introduce the single-particle quantum number $\alpha \in \{+,-\}$, where $\alpha = \pm$ corresponds to the upper dot $(+)$ or lower dot $(-)$ respectively.[60, 61, 62, 63] In analogy with the real electron spin one can define a spin operator algebra describing the vertical motion, where the quantum number of the z-component of this pseudo- or isospin, $\hat{I}_z$ is given by α [60][1]

$$\hat{I}_z \left|\pm\right\rangle = \pm\frac{1}{2} \left|\pm\right\rangle . \tag{3.3}$$

The $x-$ and $y-$ components of the pseudospin are typically expressed by the raising and lowering operators $\hat{I}_+$,$\hat{I}_-$ defined by:

$$\hat{I}_\pm \left|\mp\right\rangle = \left|\pm\right\rangle ; \quad \hat{I}_\pm \left|\pm\right\rangle = 0. \tag{3.4}$$

Thus the pseudospin algebra is given by:

$$\hat{I}_x := \frac{1}{2}\left(\hat{I}_+ + \hat{I}_-\right); \quad \hat{I}_y := \frac{1}{2i}\left(\hat{I}_+ - \hat{I}_-\right); \quad [\hat{I}_x, \hat{I}_y] = i\,\hat{I}_z. \tag{3.5}$$

The last equation denotes the cyclic commutation relation of the (pseudo-)spin algebra.
The eigenstates of I_x are the symmetric, $|s\rangle = (|+\rangle + |-\rangle)/\sqrt{2}$, and antisymmetric state, $|a\rangle = (|+\rangle - |-\rangle)/\sqrt{2}$, with $I_x \left|s\right\rangle = \frac{1}{2}\left|s\right\rangle$ and $I_x \left|a\right\rangle = -\frac{1}{2}\left|a\right\rangle$ respectively.
In the pseudospin representation the interdot tunneling $\hat{H}_T$ and the asymmetry $\hat{H}_{as}$ have the following form:

$$\begin{aligned}\hat{H}_T &= -\Delta_{sas}\,\hat{I}_x \\ \hat{H}_{as} &= V_Z\,\hat{I}_z \,. \end{aligned} \tag{3.6}$$

[1] Frequently the z-axes of the pseudospin is chosen to diagonalize the tunnel Hamiltonian (3.6), which corresponds to the x-axes in our definition [47, 50, 53, 55, 56]. The two representations are of course equivalent and are connected by a rotation of the pseudospin.

Δ_{sas} denotes the energy difference between the symmetric and antisymmetric wavefunction due to interdot tunneling and V_Z is a constant energy shift of all single-particle states between upper and lower dot. A complete single-particle basis for the Hamiltonian (3.1) is given by all states $|nm\alpha\sigma\rangle$, where the angular momentum m and the principal number n determine the Fock-Darwin orbital that characterizes the lateral motion, while $\alpha \in \{+,-\}$ labels the dot and characterizes the vertical motion. $\sigma \in \{\uparrow,\downarrow\}$ denotes the z-component of the real electron spin.

3.2.2 Intra- and interdot Coulomb interaction

The Coulomb interaction $\hat{\mathcal{V}}_c$ is defined by:

$$\hat{\mathcal{V}}_c \;=\; \frac{1}{\kappa}\frac{1}{2}\sum_{i,j=1}^{N}(\hat{V}_c^{ij})\;. \tag{3.7}$$

Here $\hat{V}_c^{i,j} = \frac{1}{(r_{ij}^2+(z_i-z_j)^2)^{1/2}}$ is the inverse relative distance between two electrons where r_{ij} defines the lateral distance and $z_i - z_j$ the vertical one. In the layer model $z_i - z_j \in \{0, d\}$, corresponding to either two electrons in the same dot or in opposite dots, giving rise to the terminology of intradot and interdot Coulomb interaction, respectively.

As discussed in the last chapter the matrix elements of the intradot Coulomb interaction depend on the external magnetic field and the confinement via the universal factor $\sqrt{\omega_{eff}}$ (see Eq. (2.19)), which accounts for the shrinking of the single-particle wavefunction with increasing effective confinement $\omega_{eff} = \sqrt{\omega_0^2 + \omega_c^2/4}$. However, the interdot Coulomb interaction is more complicated. Since the interdot distance d is independent of the effective confinement, it sets a minimum distance between electrons in different dots and thus an upper limit of the interdot Coulomb interaction. There is no single universal scaling factor relating interdot matrix elements of different parameters of ω_0, ω_c, d to one another. In fact, the interdot Coulomb interaction depends on the characteristic length $l \propto 1/\sqrt{\omega_{eff}}$ defined in Eqs. (2.4),(2.15) as well as on the ratio d/l.

Whether intra- or interdot interaction dominate the Coulomb correlations depends on the factor $\langle\sqrt{r^2+d^2}/r\rangle$ and thus on the ratio between vertical and average lateral distance $d/l \propto d\sqrt{\omega_{eff}}$. Classically the ground state configuration of N electrons confined to two parallel layers with parabolic in plane confinement changes as function of the layer distance [64, 65], which illustrates the impact of the ratio between interdot and intradot Coulomb interaction on the electronic structure of the double dot. In the quantum mechanical description of the double dot one also has to include the effect of interdot tunneling which opposes interdot Coulomb correlations.[51, 66] Experimentally a decreasing interatomic distance also increases the interdot tunneling, which complicates a systematic study of the change of Coulomb correlations with the interdot distance. Alternatively the transition from mainly intradot correlated electrons to mainly interdot correlated electrons can be seen by studying pair correlation functions for eigenstates with increasing total angular momentum, M, since the lateral extension of the eigenfunctions increases with M.[62, 63]

In this chapter we present another important consequence of the magnetic field dependence of the Coulomb correlations. We show that a change in the parameter d/l can lead to a crossing between states only differing in the vertical motion which causes a strong spontaneous charge-polarization in vertical direction at arbitrarily small asymmetries between the dots.

The dependence of the Coulomb operator $\hat{\mathcal{V}}_c$ defined in Eq. (3.7) on the pseudospin can be expressed by introducing the projection operators $\hat{P}_{\pm}^{(i)}$, which project the i-th electron to the upper dot ($\hat{P}_{+}^{(i)}$) or to the lower dot ($\hat{P}_{-}^{(i)}$), respectively. The inverse distance $\hat{V}_c^{(i,j)}$ between the electrons i and j is then expressed by:

$$\begin{aligned}\hat{V}_c^{(i,j)} &= \hat{V}_{intra}^{(i,j)} + \hat{V}_{inter}^{(i,j)} \\ &= \frac{1}{r_{ij}} \otimes \left(\hat{P}_{+}^{(i)}\hat{P}_{+}^{(j)} + \hat{P}_{-}^{(i)}\hat{P}_{-}^{(j)}\right) + \frac{1}{(r_{ij}^2+d^2)^{1/2}} \otimes \left(\hat{P}_{+}^{(i)}\hat{P}_{-}^{(j)} + \hat{P}_{-}^{(i)}\hat{P}_{+}^{(j)}\right) .\end{aligned}$$

We will use this representation in the following subsection to prove symmetries of the double dot system.

Finally we briefly discuss the form of the Coulomb matrix elements in the basis used for the numerical calculations. They are given by:

$$\begin{aligned}&\langle n_1\, m_1\, \alpha_1\, \sigma_1, n_2\, m_2\, \alpha_2\, \sigma_2| \frac{1}{(r_{12}^2+(z_1-z_2)^2)^{1/2}} |n_1'\, m_1'\, \alpha_1'\, \sigma_1', n_2'\, m_2'\, \alpha_2'\, \sigma_2'\rangle \qquad (3.8)\\ &= \delta_{m_1+m_2,m_1'+m_2'}\delta_{\alpha_1,\alpha_1'}\delta_{\alpha_2,\alpha_2'}\delta_{\sigma_1,\sigma_1'}\delta_{\sigma_2,\sigma_2'} \langle n_1\, m_1, n_2\, m_2| \frac{1}{\sqrt{r_{12}^2+(1-\delta_{\alpha_1\,\alpha_2})\,d^2}} |n_1'\, m_1',\ n_2'\, m_2'\rangle \ .\end{aligned}$$

Since the Coulomb interaction is independent of the real spin it commutes with all spin components. Furthermore the additional Kronecker deltas in the above equation correspond to the conservation of the total angular momentum $\hat{\mathcal{L}}_z = \sum_i \hat{L}_z^{(i)}$ and the z-component of the total pseudospin $\hat{\mathcal{I}}_z = \sum_i \hat{I}_z^{(i)}$. The matrix elements Eq. (3.8) are calculated for each value of d/l as presented in Appendix A.2.

3.2.3 Symmetries and competing mechanisms

The rotationally symmetric lateral confinement of the double dot leads the conservation of the angular momentum $\hat{\mathcal{L}}_z$. Since furthermore the Hamiltonian (3.2) does not act on the spin degree of freedom the spin operators $\hat{\mathcal{S}}^2, \hat{\mathcal{S}}_z$ also commute with the Hamiltonian. Therefore the eigenstates of the double dot can simultaneously be chosen to be eigenstates of $\hat{\mathcal{L}}_z, \hat{\mathcal{S}}^2, \hat{\mathcal{S}}_z$, and are thus characterized by their eigenenergy as well as by the quantum numbers M, S, S_z. However, while we encountered these symmetries already for a single dot, there is an additional symmetry for the double dot concerning exclusively the vertical degree of freedom. In case of perfectly symmetric dot (i.e. in absence of the interdot asymmetry, $V_Z = 0$) the dots can be interchanged without changing the system. In other words, the pseudospin parity $\hat{\mathcal{P}}$ (in the following only called parity), that flips the isospin

of each electron (exchanging electrons between upper and lower dot) is conserved.[46] It can be represented by the pseudospin operators in the following form:

$$\hat{\mathcal{P}} = 2^{N_e} \cdot \hat{I}_x^{(1)} \otimes \ldots \otimes \hat{I}_x^{(N_e)} \,. \tag{3.9}$$

Applying the (pseudospin) parity operator twice results in the identity i.e. $\hat{\mathcal{P}}\hat{\mathcal{P}} = \mathbf{1}$, so that the eigenvalues of the parity are $P = \pm 1$. For a single particle the parity eigenstates are the symmetric and the antisymmetric state i.e. $|P = \pm 1\rangle = (|\alpha = +\rangle \pm |\alpha = -\rangle)/\sqrt{2}$. For a many-particle state the parity eigenstates can have a rather complicated form and in particular they are in general not eigenstates to $\hat{\mathcal{I}}_x$. The eigenvalue of $\hat{\mathcal{P}}$ is given by $P = (-1)^{n_a} \in \{+1, -1\}$, where n_a denotes the occupation of antisymmetric orbitals. In the presence of an asymmetry between the dots the parity conservation is broken and states of different parity are mixed. Except for the pseudospin parity which is conserved for a symmetric double dot, neither of the components of the pseudospin $\hat{\mathcal{I}}_x, \hat{\mathcal{I}}_y, \hat{\mathcal{I}}_z$ nor its square $\hat{\mathcal{I}}^2$ are conserved.[50, 60]

It is important to understand the competition between interdot tunneling and Coulomb interaction. The Coulomb operator commutes with the z-component of the pseudospin:

$$0 = [\hat{\mathcal{V}}, \hat{\mathcal{I}}_z] = [\hat{\mathcal{V}}_{intra}, \hat{\mathcal{I}}_z] = [\hat{\mathcal{V}}_{inter}, \hat{\mathcal{I}}_z]$$

which follows from the relation $[\hat{P}_+^{(i)}, \hat{I}_z^{(i)}] = 0 = [\hat{P}_-^{(i)}, \hat{I}_z^{(i)}]$. However, the conservation of $\hat{\mathcal{I}}_z$ is broken by the interdot tunneling $\hat{\mathcal{H}}_T = -\Delta_{sas}\hat{\mathcal{I}}_x$. Vice versa the Coulomb interaction does not commute with $\hat{\mathcal{I}}_x$, or the interdot tunneling, respectively.

$$[\hat{\mathcal{V}}_c, \hat{I}_x] \;=\; \frac{1}{\kappa} \sum_{i,j|i<j} \left(\frac{1}{r_{ij}} - \frac{1}{(r_{ij}^2 + d^2)^{1/2}} \right) \otimes [\hat{P}_+^{(i)}\hat{P}_+^{(j)} + \hat{P}_-^{(i)}\hat{P}_-^{(j)}, \hat{I}_x^{(i)} + \hat{I}_x^{(j)}] \,.$$

Thus the difference between inter- and intradot Coulomb energy breaks the conservation of $\hat{\mathcal{I}}_x$, since it leads to correlations in z-direction which oppose the occupation of the delocalized eigenstates of the interdot tunneling. On the other hand, the conservation of $\hat{\mathcal{I}}_z$ is broken only by the interdot tunneling and since we are interested in the weak coupling regime, we will use this fact later in subsection 3.3.2.

We summarize the discussion by emphasizing the following facts:

1. The orbital degree of freedom of the single-particle eigenstates separates in the lateral motion described by the Fock-Darwin states and a vertical motion consisting of a symmetric and an antisymmetric wavefunction. The interdot tunneling thereby always favors the symmetric wavefunction.

2. According to the symmetries of the system the eigenstates can be labeled in addition to their eigenenergies by N, S, S_z, M, labeling the electron number, the spin degrees of freedom and the angular momentum, respectively. For symmetric dots the pseudospin parity $\hat{\mathcal{P}}$ represents an additional symmetry.

3. The Coulomb interaction breaks the single-particle behavior and leads to correlations that mix vertical and lateral degree of freedom. By increasing the factor $d/l \propto d\sqrt{\omega_{eff}}$ the intradot Coulomb interaction grows faster than the interdot Coulomb interaction. Thus the factor d/l allows to modify the correlations on the double dot.

4. In the limit of vanishing interdot coupling $\hat{\mathcal{I}}_z$ is conserved.

5. Since the Coulomb interaction does not commute with $\hat{\mathcal{I}}_x$, the occupation of the symmetric or antisymmetric orbitals is not conserved, although in the case of symmetric dots the parity $P = (-1)^{n_a}$ is a good quantum number.

3.2.4 Exact diagonalization of the Hamiltonian

Before we present our results in the following sections, we shortly comment on how the method of exact diagonalization introduced in subsection 2.2.4 for the single dot is used to obtain the eigenspectrum of the interacting double dot.

Therefore, we first rewrite the many-particle Hamiltonian in second quantized form, where we use again the effective units introduced in Eq. (2.13).

$$\hat{\mathcal{H}}^* = \hat{\mathcal{H}}^*_{FD} + \hat{\mathcal{H}}^*_Z + \hat{\mathcal{H}}^*_T + \hat{\mathcal{H}}^*_{As} + \hat{\mathcal{V}}^*_{inter} + \hat{\mathcal{V}}^*_{intra} \,. \tag{3.10}$$

The superscript star, "*", indicates that the corresponding quantity is expressed in effective Rydbergs.

The single-particle terms of the Hamiltonian have the following form:

$$\begin{aligned}
\hat{\mathcal{H}}^*_{FD} &= \hbar\omega^*_{eff} \sum_{n,m,\alpha,\sigma} (2n + |m| + 1)\, c^\dagger_{n\,m\,\alpha\,\sigma}\, c_{n\,m\,\alpha\,\sigma} + \frac{\hbar\omega^*_c}{2} \sum_{n,m,\alpha,\sigma} m\, c^\dagger_{n\,m\,\alpha\,\sigma}\, c_{n\,m\,\alpha\,\sigma} \\
\hat{\mathcal{H}}^*_Z &= \alpha\, \hbar\omega^*_c\, \hat{\mathcal{S}}_z \\
\hat{\mathcal{H}}^*_T &= -\Delta^*_{sas} \hat{\mathcal{I}}_x \\
\hat{\mathcal{H}}^*_{As} &= V^*_Z \hat{\mathcal{I}}_z \,.
\end{aligned} \tag{3.11}$$

The operators $c^\dagger_{n\,m\,\alpha\,\sigma}$ and $c_{n\,m\,\alpha\,\sigma}$ create and annihilate an electron in the single-particle state $|nm\alpha\sigma\rangle$, where n and m denote the principal quantum number and the angular momentum of a Fock-Darwin orbital, α denotes the pseudospin and σ the real spin. The pseudospin operators $\hat{\mathcal{I}}_x, \hat{\mathcal{I}}_z$ are defined by:

$$\begin{aligned}
\hat{\mathcal{I}}_x &= \frac{1}{2} \sum_{n,m,\alpha,\sigma} c^\dagger_{n\,m\,\alpha\,\sigma} c_{n\,m\,\bar{\alpha}\,\sigma} \\
\hat{\mathcal{I}}_z &= \frac{1}{2} \sum_{n,m,\sigma} \left(c^\dagger_{n\,m+\sigma} c_{n\,m+\sigma} - c^\dagger_{n\,m-\sigma} c_{n\,m-\sigma} \right) \,.
\end{aligned} \tag{3.12}$$

Here we introduced $\bar{\alpha}$ denotes the opposite pseudospin of α.

The difficult part of the Hamiltonian is the Coulomb interaction, which is a two-particle operator causing correlations between the electrons. Intra- and interdot Coulomb interaction are defined by:

$$\begin{aligned}\hat{\mathcal{V}}^*_{inter} &= \sqrt{\hbar\omega^*_{eff}}\frac{1}{2}\sum_{\alpha,\sigma,\sigma'}\sum_{\substack{n_1,m_1\\n_2,m_2}}\sum_{\substack{n_3,m_3\\n_4,m_4}}\langle n_1m_1,n_2m_2|\,\tilde{V}_{inter}\,|n_3m_3,n_4m_4\rangle \\ &\quad\times c^\dagger_{n_1m_1\alpha\sigma}c^\dagger_{n_2m_2\bar{\alpha}\sigma'}c_{n_4m_4\bar{\alpha}\sigma'}c_{n_3m_3\alpha\sigma} \\ \hat{\mathcal{V}}^*_{intra} &= \sqrt{\hbar\omega^*_{eff}}\frac{1}{2}\sum_{\alpha,\sigma,\sigma'}\sum_{\substack{n_1,m_1\\n_2,m_2}}\sum_{\substack{n_3,m_3\\n_4,m_4}}\langle n_1m_1,n_2m_2|\,\tilde{V}_{intra}\,|n_3m_3,n_4m_4\rangle \\ &\quad\times c^\dagger_{n_1m_1\alpha\sigma}c^\dagger_{n_2m_2\alpha\sigma'}c_{n_4m_4\alpha\sigma'}c_{n_3m_3\alpha\sigma}\ .\end{aligned}$$

The Coulomb matrix elements are defined via the dimensionless quantities: $\tilde{V}_{intra} = l_{rel}/r_{12}$, and $\tilde{V}_{inter} = l_{rel}/\sqrt{r_{12}^2+d^2}$, where $r_{12} = |\vec{r}_1 - \vec{r}_2|$ denotes the lateral distance and $l_{rel} = \sqrt{2}l$ is the characteristic length of the relative motion. While the matrix elements of $\tilde{V}_{intra}$ are parameter independent, the elements of $\tilde{V}_{inter}$ have to be computed for each value of d/l.

The eigenstates of the Hamiltonian (3.10) are calculated by means of exact diagonalization, as discussed in subsection 2.2.4 for the case of a single dot. This approach is particularly important here since it takes Coulomb interaction fully into account, which turns out to be essential for the correlation-induced charge polarization discussed in the following section. In our calculations we again use the symmetries of the system and build up the many-particle basis for the eigenstates to a fixed subspace characterized by N, M, S, S_z as discussed in subsection 2.2.4.

Relevant parameters for the experimentally realized vertical double dots are: $0.5Ryd^* < \hbar\omega_0 < 1Ryd^*$, $0 < \hbar\omega_c < 5Ryd^*$, $1a_0^* < d < 3a_0^*$. Finally we mainly consider weak coupling and often use $\Delta_{sas} = 0.02Ryd^*$. The effective units are listed in Table 2.1. The relevant material is GaAs where $1Ryd^* = 5.93meV$ and a magnetic field of 1 Tesla corresponds to $\hbar\omega_c = 0.29Ryd^*$ and vice versa $\hbar\omega_c = 1Ryd^*$ corresponds to a magnetic field of $B \approx 3.45T$. Furthermore the effective Bohr radius is given by $a_0^* = 9.79nm$.

3.3 Spontaneous charge localization tunable by perpendicular magnetic field

The Hamiltonian (3.10) of the double dot depends on the distance d between the layers, the confinement $\hbar\omega_0$, the interdot tunneling Δ_{sas}, the level asymmetry between the dots V_Z and the magnetic field applied in z-direction, characterized by the cyclotron frequency $\hbar\omega_c = eB/m^*$. While d, $\hbar\omega_0$ and Δ_{sas} are fixed by the growth process of the sample, the magnetic field can be changed easily.

Surprisingly we found, that a sweep of the perpendicular magnetic field does not only lead to transitions to states with higher angular momenta, but it can also lead to a spontaneous

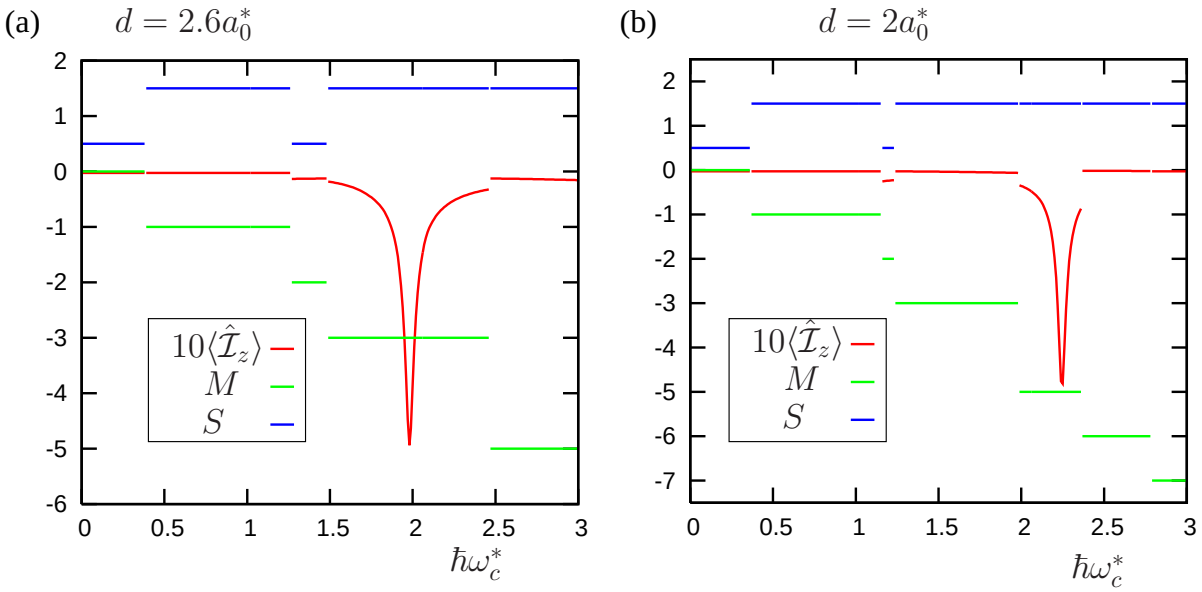

Figure 3.2: *Angular momentum M, total spin S and expectation value of the z-component of the isospin $\langle\hat{\mathcal{I}}_z\rangle$ for the three-electron ground state as function of the magnetic field. Due to the Zeeman term the spins are always aligned with the external field, i.e. $S_z = S$. The peak in $\langle I_z\rangle$ illustrates a strong spontaneous charge localization. Parameters: Tunneling strength: $\Delta_{sas} = 0.02 Ryd^*$, confinement: $\hbar\omega_0 = 0.5 Ryd^*$, layer asymmetry: $V_Z = 10^{-4} Ryd^* \ll \Delta_{sas}$ layer separation in (a) $d = 2.6\, a_0^*$ and (b) $d = 2\, a_0^*$.*

charge localization in one of the dots. In the following we use the words charge-polarization and charge-localization as synonyms. Fig. 3.2 shows the angular momentum and the spin of the three-electron ground state characterized by M, S, and the expectation value $\langle\hat{\mathcal{I}}_z\rangle$ of the z-component of the isospin for two different interlayer distances d.[2] The value of the charge localization at the peak is $\langle\hat{\mathcal{I}}_z\rangle \approx -0.5$ and corresponds to two electrons occupying the lower dot and only one electron the upper dot. The special feature of the charge localization depicted in Fig. 3.2 is, that it is not tuned by the asymmetry between the dots, but by the external magnetic field which doesn't cause any force in z-direction. Furthermore the charge localization is not connected with a transition between states of different angular momentum and/or spin.

In the following we call transitions where either the angular momentum or the spin is changed (or both), 'transitions in the lateral degree of freedom', since they arise already for single dots. They are based on two effects. First the lateral extension of the wavefunction shrinks with increasing magnetic field like $l \propto 1/\sqrt{\omega_{eff}}$, see Eqs. (2.4),(2.15), which leads to an increase of the Coulomb interaction. Second, the Fock-Darwin states converge into Landau levels with increasing magnetic field and thereby reduce the level spacing between

[2] Even though Fig. 3.2 (a) and Fig. 3.2 (b) correspond to a different interlayer distance d we use the same coupling strength Δ_{sas}. In an experiment this could be achieved e.g. by properly choosing the width of the wells w and the interdot barrier width b introduced in Fig. 3.1.

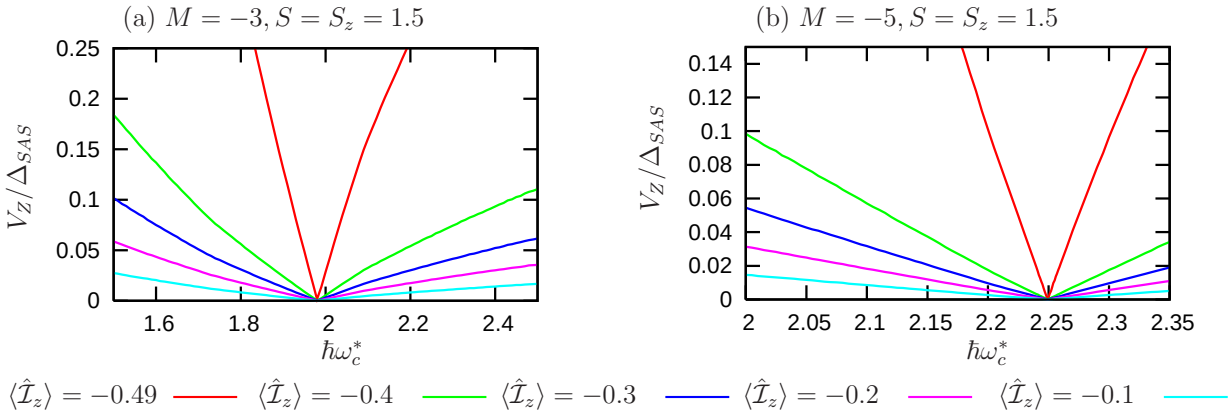

Figure 3.3: *Contours of constant vertical polarization, $\langle\hat{\mathcal{I}}_z\rangle = const$ as function of magnetic field ω_c and asymmetry V_Z between upper and lower dot. The effect of asymmetry on the polarization strongly depends on the Coulomb correlations in the dot, and thus on the magnetic field. Parameters in (a)and (b) like in Fig. 3.2 (a) and (b).*

single-particle states with consecutive angular momenta. The combination of lower level spacing and higher Coulomb interaction leads to ground-state transitions favoring states with higher angular momenta, that have a larger lateral extension and thus lower Coulomb interaction.[62, 63] Of particular is the angular momentum corresponding to the maximum density droplet, realized by the occupation of single-particle states with successive angular momenta.[57, 67] For three electrons confined to the double dot this results in $M = -3$. The magnetic field where the ground state turns into the maximum density droplet, is often called the 'regime of filling factor $\nu = 1$', which originates from the similarity of a quantum dot with a finite Quantum Hall system [46]. Even though the maximum density droplet state is more stable in single dots than in double dots, we note that the steps corresponding to $M = -3, S = S_z = 1.5$ in Fig. 3.2 are extraordinarily broad.

In the intermediate and strong coupling regime $\Delta_{sas} \geq \hbar\omega_0$, transitions in the lateral degree of freedom are often accompanied by transitions in the vertical direction [53, 55, 56, 57]. In that regime an increasing magnetic field favors transitions where an electron leaves an antibonding level of low angular momentum and enters a bonding level of higher angular momenta, thus flipping the x-component of its pseudospin. The electron thus gains tunneling energy (since more bonding levels are occupied) and simultaneously reduces the Coulomb energy (due to the larger lateral extension).[47, 50] This kind of transitions leads in our definition to an increase of the x-component of the pseudospin with increasing magnetic field and cannot lead to a charge localization connected with the z-component of the pseudospin. Furthermore the spontaneous charge localization discussed here is not related with a change in the lateral degree of freedom.

We emphasize that the asymmetry V_Z chosen in Fig. 3.2 is much smaller than the interdot coupling and therefore only at a critical magnetic field a significant charge localization is found, while the ground state is delocalized over both dots at general magnetic fields. This

is in sharp contrast to the single electron states. For a single electron the polarization is independent of the magnetic field and only depends on the vertical level asymmetry and the interdot coupling. It is given by $\langle I_z \rangle = 1/2 * V_Z/(\sqrt{V_Z^2 + \Delta_{sas}^2})$. For the many-particle states this is not longer true as shown in Fig. 3.3, where we plot the contours of constant vertical polarization as function of the magnetic field and the vertical asymmetry V_Z between the dots. We find that the charge-polarization at constant asymmetry strongly depends on the magnetic field and that there are critical magnetic fields where already a tiny asymmetry is sufficient to strongly polarize the wavefunction.

Actually, in real experiments the asymmetry between the dots can exceeds the interdot coupling which leads to a strong charge polarization over a broad parameter regime and for all angular momenta [58]. In the situation discussed here, however, the asymmetry is much smaller than the interdot coupling and the presented charge-polarization only occurs for certain three-electron states and only at a critical magnetic fields. In the following subsection we relate the charge-localization to crossings between states only differing in parity, and we will show that these crossings are driven by Coulomb correlations.

3.3.1 Crossing between states only differing in parity

We discussed in subsection 3.2.3 that the ratio between layer distance and confinement length, d/l, determines whether electrons are mainly intradot or mainly interdot correlated. We now study how the vertical degree of freedom characterizing the few-electron molecular binding of the artifical molecule, is affected by a change of $d/l \propto d\sqrt{\omega_{eff}}$. Therefore we calculate the three-electron eigenspectrum in a fixed 'lateral' subspace characterized by M, S, S_z. For perfectly symmetric dots (i.e. $V_Z = 0$) the (pseudospin-) parity is conserved and its eigenvalues are given by $(-1)^{n_a}$ where n_a denotes the occupation of antisymmetric orbitals in z-direction. For small tunneling $\Delta_{sas} \ll \hbar\omega_0$ the energy splitting between the parity eigenstates $|P = \pm 1\rangle$ within the same set of quantum numbers (M, S, S_z) is due to their different tunneling energies, as the occupation probabilities of symmetric and antisymmetric orbitals depend on parity. However, as discussed in subsection 3.2.3 the x-component of the pseudospin is not conserved in the presence of Coulomb interaction. In particular it follows that the occupation of symmetric and antisymmetric orbitals of the parity eigenstates is a function of the magnetic field. This can lead to correlation induced crossings between states differing only in parity as depicted in Fig. 3.4 and Fig. 3.5. This parity crossing is a pure many-body effect.

While in a real experiment the interdot coupling will depend on the interlayer distance we fix it in Fig. 3.4 to a small, constant value, here $\Delta_{sas} = 0.02 Ryd^*$. We do this to highlight the effect of Coulomb correlations, while the dependence of the charge polarization on the interdot tunneling will be discussed later in the context of Fig. 3.9. However we point out that in the mapping from a realistic finite confinement potential in z-direction (see e.g. Fig 3.1) to the layer model used here, the interlayer distance does not only depend on the interdot barrier width b, which strongly changes the interdot coupling, but also on the well thickness w, which is of minor relevance for the interdot coupling. Thus it should

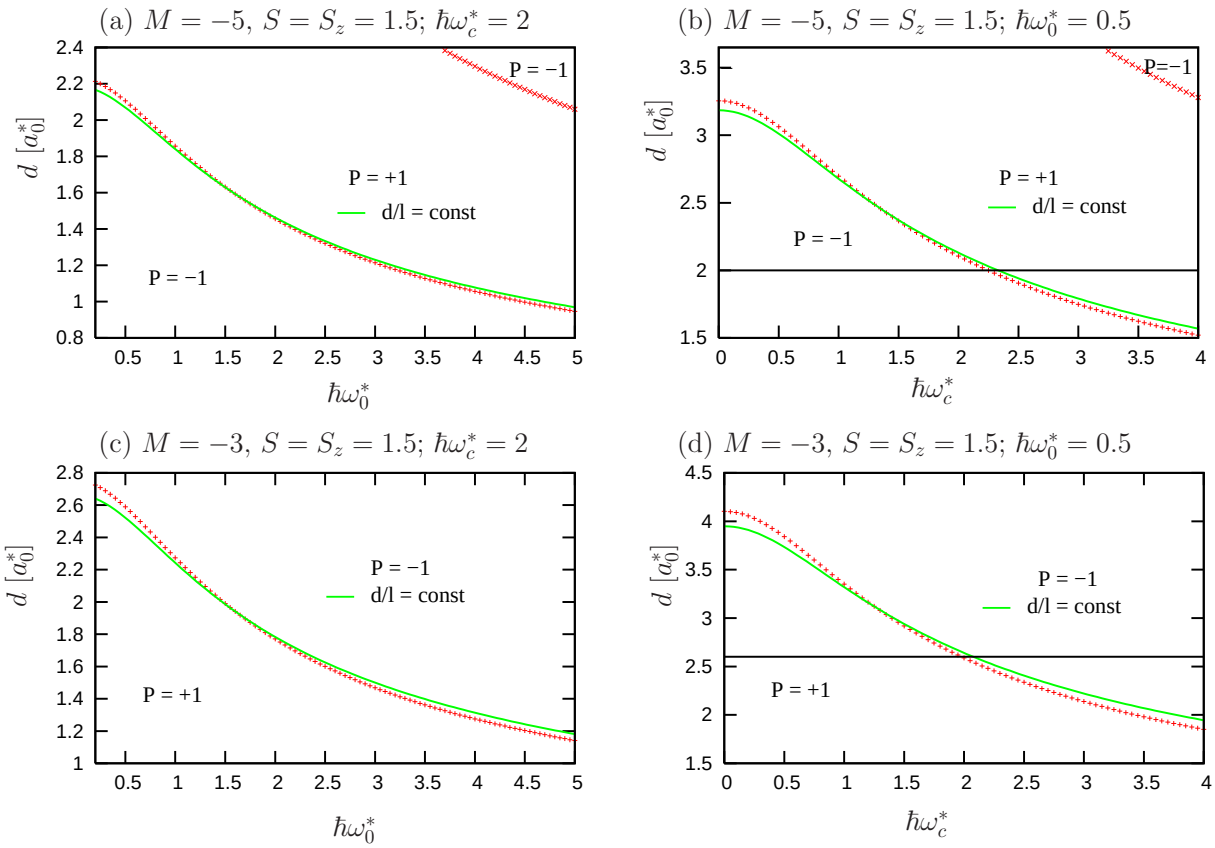

Figure 3.4: *Parity of energetically lowest state in the subspace of* $M = -5, S = S_z = 1.5$ *(upper row) and* $M = -3, S = S_z = 1.5$ *(lower row) as function of the interdot distance* d*, and either the confinement strength* $\hbar\omega_0$ *(left column) or the magnetic field* $\hbar\omega_c$ *(right column). Interdot tunneling is kept fixed at* $\Delta_{sas} = 0.02 Ryd^*$*. Calculated values for parity crossings are indicated by red points. They follow lines of constant ration* d/l *(green lines). Black lines in (b) and (d) correspond to parameters of the magnetic-field sweeps illustrated in Fig. 3.2. The spontaneous charge polarization in Fig. 3.2 takes place right at the parity crossing.*

be possible to vary the interlayer distance in some range without changing the interdot coupling. In particular we believe that the parameters chosen in Fig. 3.2 are experimentally relevant.

Fig. 3.4 shows phase/stability diagrams between states differing only in parity for the subspaces $M = -5, S = S_z = 1.5$ (upper row) and $M = -3, S = S_z = 1.5$ (lower row). In Fig. 3.4 (a) and (c) the relation between the interlayer distance and the critical confinement strength at the phase boundary are illustrated while Fig. 3.4 (b) and (d) show the relation between the interlayer distance and the critical magnetic field. The parameters used in Fig. 3.2 are marked by the black solid lines. The critical field of the charge polarization of Fig. 3.2 exactly coincides with the magnetic field, where the parity changes in Fig. 3.4.

The critical values of $d, \hbar\omega_0$ or $d, \hbar\omega_c$ depicted in Fig. 3.4 can well be fitted by a line of

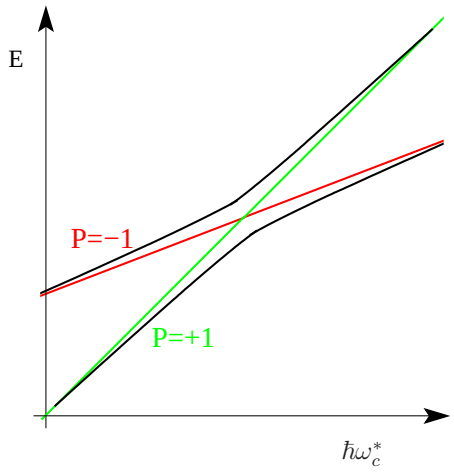

Figure 3.5: *Colored lines illustrate the parity-crossing in a symmetric double dot in a magnetic field sweep. In the presence of a slight asymmetry between the dots, the parity eigenstates are mixed and the crossing turns into an anticrossing as shown by the black lines. The depicted situation corresponds to the parity crossing in the subspace* $M = -3, S = S_z = 1.5$.

constant ratio of $d/l = const$, as indicated by the blue curves in Fig. 3.4. The constants in Fig. 3.4 (a)-(d) are used as fitting parameters, they are similar for all figures and have values of $1.5 < d/l < 2$. Even though the absolute value of the Coulomb energy for the parity eigenstates at the crossing is more than doubled in the depicted parameter regime the ratio between the interdot and the intradot Coulomb interaction for the parity eigenstates is approximately constant ($\pm 3\%$) along the transition line. Furthermore the ratios are also similar for the different figures and have values of $2 < \langle V_c^{inter} \rangle / \langle V_c^{intra} \rangle < 2.3$.

We note, that the transition of the parity is reversed in the two distinct subspaces. While with increasing ratio d/l the parity changes from $P = +1$ to $P = -1$ in the case of $M = -3, S = S_z = 1.5$, it changes from $P = -1$ to $P = +1$ in the case of $M = -5, S = S_z = 1.5$. Furthermore there is a second parity crossing in the case of $M = -5, S = S_z = 1.5$ for even higher values of d/l.

3.3.2 Spontaneous charge localization

According to Fig. 3.4 a magnetic field sweep leads to a crossing between states differing only in parity. A schematic energy profile of such a crossing is depicted in Fig. 3.5, by the colored lines. If one now breaks the parity conservation, e.g. by introducing a tiny asymmetry $\hat{\mathcal{H}}_{As}$ between the dots, then the crossing turns into an anticrossing as shown by the black lines in Fig. 3.5. Far from the crossing non-degenerate-perturbation theory can be applied and the mixing between the parity eigenstates (caused by $\hat{\mathcal{H}}_{As}$) scales like the inverse of their energy difference. Right at the critical magnetic field, the parity eigenstates are maximally superposed in order to minimize the perturbation $\hat{\mathcal{H}}_{As}$. The asymmetry between the dots thus converts the crossing into an anticrossing and leads to strongly polarized states at the critical magnetic field.

Fig. 3.6 illustrates a quantitative study of the influence of a slight asymmetry V_Z between the dots on the parity crossing schematically shown in Fig. 3.5. First of all we note, that

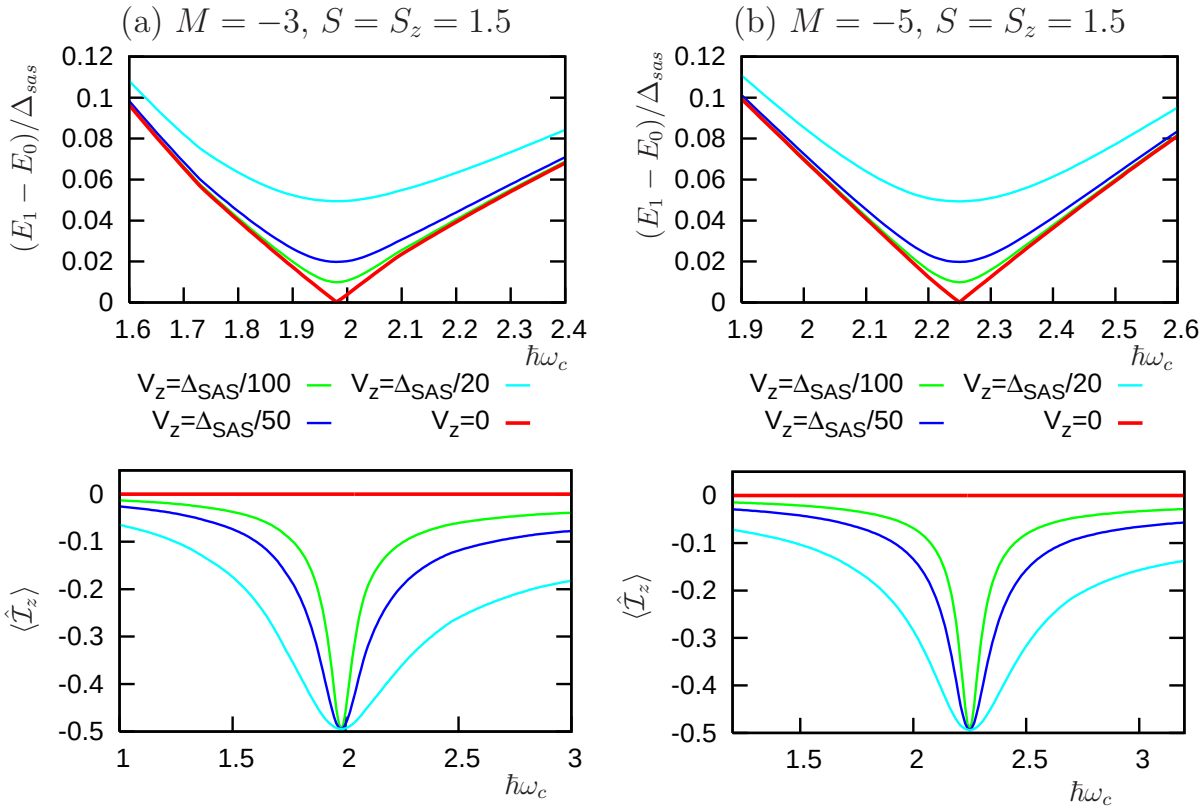

Figure 3.6: *Upper row: Energy difference between the two lowest eigenstates as function of the magnetic field for various small asymmetries V_Z. In the presence of an asymmetry the crossing turns into an anticrossing with a minimum energy difference given by V_Z. Lower panel the asymmetry strength V_Z determines the width of the charge localization peak but does not change the critical magnetic field. Parameters: $\hbar\omega_0 = 0.5$, $\Delta_{sas} = 0.02$ (a) $d = 2.6a_0^*$ (b) $d = 2.a_0^*$ Energies given in Ryd^**

the effect of the asymmetry on the crossing is qualitatively the same for both illustrated subspaces. The graphs in the upper row of Fig. 3.6 show the energy difference between the two lowest eigenstates. For perfectly symmetric dots (red line) states of different parity cross in a magnetic field sweep, which results in a vanishing energy difference at the critical magnetic field. The magnetic fields corresponding to the critical cyclotron frequencies $\hbar\omega_c = 1.98 Ryd^*$ and $\hbar\omega_c = 2.24 Ryd^*$ shown in Fig. 3.6 are $B = 6.83T$ and $B = 7.72T$ (see Table 2.1). In the presence of level asymmetry between the dots, the crossing turns into an anticrossing and the minimum energy distance is given by V_Z. Simultaneously the eigenstates are strongly polarized in opposite direction with a maximum charge polarization of $\langle \hat{\mathcal{I}}_z \rangle = \pm 0.5$ as shown in the lower row of Fig 3.6. (In Fig 3.6 only the polarization of the ground state is shown, the first excited state has just the inverse polarization.) Note, that parity eigenstates are always unpolarized, since $\langle P | \hat{\mathcal{I}}_z | P \rangle = 0$. The widths of the charge-localization peaks are proportional to the corresponding asymmetry strength V_Z,

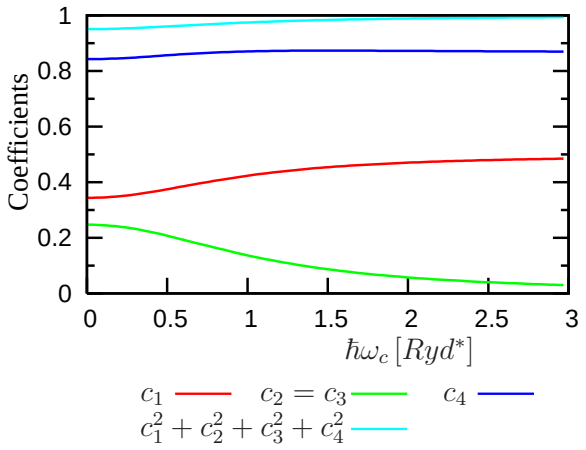

Figure 3.7: *Magnetic-field dependence of many particle states* $|I_z = \pm 1/2\rangle$. *Illustrated are the coefficients* c_1, c_2, c_3, c_4 *introduced in Eq. (3.13) corresponding to the Slater determinants given in Eq. (3.14). The magnetic-field dependence of the coefficients is exclusively caused by Coulomb correlations since all Slater determinants considered here have the same single-particle energy. Parameters:* $\hbar\omega_0 = 0.5 Ryd^*$, $d = 2.6 a_0^*$.

however all peaks are centered at the same critical magnetic field. The asymmetry thus only visualizes the parity crossing which is caused by the magnetic field dependent Coulomb correlations.

In the following we are interested in the structure of the parity eigenstates. We start our discussion by considering the limit of small interdot tunneling. In the absence of interdot tunneling the z-component of the pseudospin, $\hat{\mathcal{I}}_z$, is conserved. If furthermore the dots are perfectly symmetric, then the three-electron ground state is twofold degenerate with $I_z = \pm 1/2$. The states $|I_z = \pm 1/2\rangle$ mainly occupy Slater determinants that minimize the lateral confinement. As an example we note that in the subspace $M = -3, S = S_z = 1.5$ the structure of each of the three-electron states $|I_z = \pm 1/2\rangle$ is mainly given by a superposition of four Slater determinants:

$$\begin{aligned} |I_z = -0.5\rangle &\approx c_1 |1\rangle + c_2 |2\rangle + c_3 |3\rangle + c_4 |4\rangle \\ |I_z = 0.5\rangle &\approx c_1 |\bar{1}\rangle + c_2 |\bar{2}\rangle + c_3 |\bar{3}\rangle + c_4 |\bar{4}\rangle \ . \end{aligned} \tag{3.13}$$

The coefficients c_1, c_2, c_3, c_4 are only determined by the Coulomb interaction, since all Slater determinants have the same single-particle energy. In the following we label an electron orbital only by its angular m and its pseudospin $\alpha = \pm$. The additional quantum numbers are always $n = 0$ and $\sigma = 0.5$ since we describe the energetically lowest Slater determinants and consider fully spin-polarized states. Within this notation the Slater determinants of Eq. (3.13) are represented by:

$$\begin{aligned} |1\rangle &= |0-, 0+, -3-\rangle \quad ; \quad |\bar{1}\rangle &= |0+, 0-, -3+\rangle \ ; \\ |2\rangle &= |0-, -1-, -2+\rangle \quad ; \quad |\bar{2}\rangle &= |0+, -1-, -2-\rangle \ ; \\ |3\rangle &= |0-, -1+, -2-\rangle \quad ; \quad |\bar{3}\rangle &= |0+, -1-, -2+\rangle \ ; \\ |4\rangle &= |0+, -1-, -2-\rangle \quad ; \quad |\bar{4}\rangle &= |0-, -1+, -2+\rangle \ . \end{aligned} \tag{3.14}$$

The two Slater determinants in each row are connected to each other by flipping all pseudospin quantum numbers.

The magnetic field dependence of the coefficients c_1, c_2, c_3, c_4 is shown in Fig. 3.7. First of all we note, that the approximate form of the eigenstates $|I_z = \pm 1/2\rangle$ of Eq. (3.13) seems justified since the sum of the occupation probabilities of the four Slater determinants is always above 95%. Furthermore Fig. 3.7 illustrates that the weight of each of these Slater determinants changes with the magnetic field. Since the Slater determinants have the same single-particle energy for all magnetic field strengths, the change of the coefficients shown in Fig. 3.7 is exclusively caused by a change of the Coulomb correlations.

If now the interdot tunneling is switched on, then $\hat{\mathcal{I}}_z$ is no longer conserved and the degenerate ground state splits in two non-degenerate parity eigenstates. For a small tunneling energy Δ_{sas}, the structure of the parity eigenstates is approximated by applying lowest-order perturbation theory:

$$|P = \pm 1\rangle \approx \frac{1}{\sqrt{2}}(|I_z = 1/2\rangle \pm |I_z = -1/2\rangle) \; . \tag{3.15}$$

Such a presentation for the parity eigenstates is justified if states $|I_Z = \pm 1/2\rangle$ are separated from excited states (within the same subspace) by an energy gap ΔE which is larger than the interdot tunnel energy Δ_{sas}.

We now apply Eq. (3.15) to the parity crossing in the subspace $M = -3, S = 1.5 = S_z$. Using Eq. (3.13) and (3.14) and changing to the symmetric s and antisymmetric a pseudospin representation defined by $|s/a\rangle = (|+\rangle \pm |-\rangle)/\sqrt{2}$ we rewrite the parity eigenstates in the following form:

$$\begin{aligned} |P = +1\rangle &\approx a_I\,|I\rangle + a_{II}\,|II\rangle + a_{III}\,|III\rangle + a_{IV}\,|IV\rangle + a_V\,|V\rangle \\ |P = -1\rangle &\approx a_I|\bar{I}\rangle + a_{II}|I\bar{I}\rangle + a_{III}|I\bar{I}I\rangle + a_{IV}|I\bar{V}\rangle + a_V|\bar{V}\rangle \; . \end{aligned} \tag{3.16}$$

Here we used:

$$\begin{array}{llllllllllll} a_I & = & c_1 & ; & |I\rangle & = & |0a, 0s, -3a\rangle & ; & |\bar{I}\rangle & = & |0s, 0a, -3s\rangle \\ a_{II} & = & \frac{1}{2}(c_2 + c_3 + c_4) & ; & |II\rangle & = & |0s, -1s, -2s\rangle & ; & |I\bar{I}\rangle & = & |0a, -1a, -2a\rangle \\ a_{III} & = & \frac{1}{2}(c_2 - c_3 - c_4) & ; & |III\rangle & = & |0a, -1a, -2s\rangle & ; & |I\bar{I}I\rangle & = & |0s, -1s, -2a\rangle \\ a_{IV} & = & \frac{1}{2}(-c_2 + c_3 - c_4) & ; & |IV\rangle & = & |0a, -1s, -2a\rangle & ; & |I\bar{V}\rangle & = & |0s, -1a, -2s\rangle \\ a_V & = & \frac{1}{2}(-c_2 - c_3 + c_4) & ; & |V\rangle & = & |0s, -1a, -2a\rangle & ; & |\bar{V}\rangle & = & |0a, -1s, -2s\rangle \; . \end{array}$$

The two Slater determinants within each row are connected to each other by exchanging symmetric with antisymmetric orbitals. This representation of the parity eigenstates illustrates two facts. First, the occupation of symmetric and antisymmetric wavefunctions depends on the parity. Second, Coulomb correlations change the occupation of symmetric and antisymmetric orbitals in a magnetic field sweep, since the coefficients $a_I, .., a_V$ are magnetic field dependent.

Consequently the energy splitting between the parity states caused by the interdot tunneling is also magnetic field dependent. Using Eq. (3.15) the energy splitting between the parity states can be approximated by:

$$\begin{aligned} E_{|P=1\rangle} - E_{|P=-1\rangle} &\approx \langle P = 1|\,\hat{\mathcal{H}}_T\,|P = 1\rangle - \langle P = -1|\,\hat{\mathcal{H}}_T\,|P = -1\rangle \\ &\approx 2\,\langle P = 1|\,\hat{\mathcal{H}}_T\,|P = 1\rangle \approx -2\Delta_{sas}\,\langle I_z = 1/2|\,\hat{\mathcal{I}}_x\,|I_z = -1/2\rangle \; . \end{aligned} \tag{3.17}$$

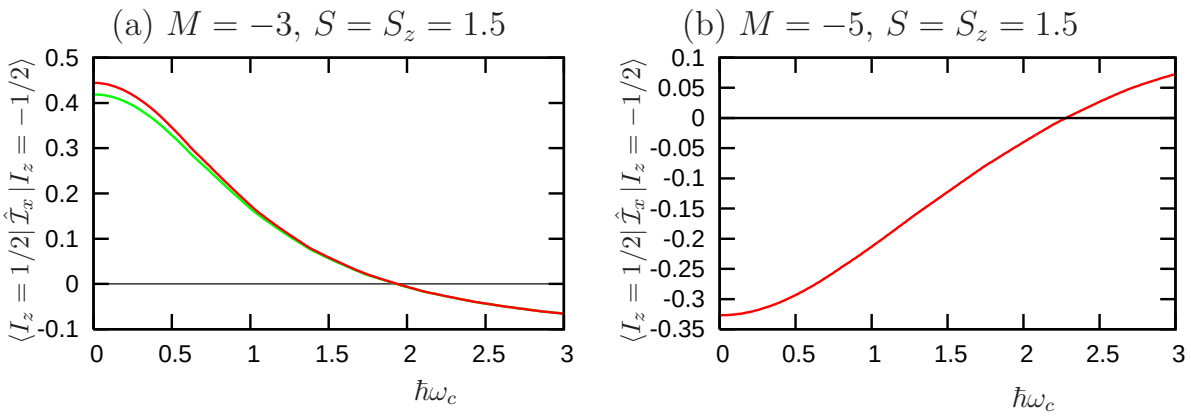

Figure 3.8: *Magnetic-field dependence of the matrix element* $\langle I_z = 1/2|\,\hat{\mathcal{I}}_x\,|I_z = -1/2\rangle$ *indicated by the red line. The green line in left graph shows the approximation given in Eq. (3.18). The plotted matrix element is proportional to the tunnel coupling between the states* $|I_z = \pm 1/2\rangle$. *Parameters: (a)* $\hbar\omega_0 = 0.5 Ryd^*$, $d = 2.6 a_0^*$; *(b)* $\hbar\omega_0 = 0.5 Ryd^*$, $d = 2 a_0^*$.

Using Eq. (3.16) and (3.17) we now get a perturbative expression for the energy splitting between the energetically lowest parity eigenstates in the subspace $M = -3, S = S_z = 1.5$. Noting that according to the data shown in Fig. 3.7 the coefficients c_2 and c_3 are equal, i.e. $c_2 = c_3$, we obtain:

$$\langle I_z = 1/2|\,\hat{\mathcal{I}}_x\,|I_z = -1/2\rangle \quad \approx \quad -\frac{1}{2}c_1^2 + c_2^2 + 2c_2c_4\ . \tag{3.18}$$

Fig. 3.8 (a) shows the magnetic field dependence of $\langle I_z = 1/2|\,\hat{\mathcal{I}}_x\,|I_z = -1/2\rangle$, together with the perturbative result given in Eq. (3.18). Fig. 3.8 illustrates that the tunnel coupling between the states $|I_z = \pm 1/2\rangle$ strongly depends on the magnetic field which is explained by the change of Coulomb correlations. While Fig. 3.8 together with Eq. (3.17) explains the parity crossing and the charge polarization in the isolated double dot, we will show in section 3.4 that the disappearance of the tunnel coupling also suppresses the current through the double dot. We emphasize that Eqs. (3.15) and (3.17) hold for any subspace of quantum numbers N_e, M, S, S_z, if the electron number N_e is odd. However, a further condition for the parity crossing and the corresponding spontaneous charge polarization is, that the matrix element $\langle I_z = 1/2|\,\hat{\mathcal{I}}_x\,|I_z = -1/2\rangle$ vanishes at a critical magnetic field. For the case $N_e = 3, M = -5, S = S_z = 1.5$ this is shown in Fig. 3.8 (b). In that case the positive parity is favored for low magnetic fields. The mechanism presented here also occurs at higher particle numbers, e.g. we found it for $N_e = 5, M = -7, S = S_z = 2.5$. Parity crossings also occur for an even number of electrons on the double dot. However in that case the crossings are in general not accompanied by a vanishing interdot tunneling and often they also occur in the absence of interdot coupling. Thus a charge localization at arbitrarily small asymmetries is only possible for an odd number of electrons on the double dot.

Finally we note that for vertically coupled double dots the (single-particle) interdot tunnel

energy Δ_{sas} is independent of the magnetic field, so that the disappearance of the interdot coupling shown in Fig. 3.8 is purely a many-body effect. This is in contrast to lateral double dots. There an increasing vertical magnetic field not only changes the Coulomb correlations but also reduces the (single-particle) tunnel energy Δ_{sas}, since it effectively decreases the overlap between electrons in the left and right dot.[68, 69]

In Eq. (3.17) the interdot tunneling is treated as small perturbation, however, with increasing interdot coupling this perturbative description of the parity eigenstates fails. This is visible in two aspects. First, the critical magnetic field where the parity crossing occurs depends on the interdot tunneling and second, due to the different structure of the parity eigenstates, the maximum of the charge localization decreases in general with increasing interdot tunneling.

In Fig. 3.9 (a) and (b) we plot the parity of the energetically lowest eigenstate of the specified subspace (i.e. $M = -3, S = S_z = 1.5$ for (a) and $M = -5, S = S_z = 1.5$ for (b)) as function of the interdot coupling and the magnetic field. In the limit $\Delta_{sas} \to 0$, the parity crossing appears at the critical magnetic field predicted by Eq. (3.17) and shown in Fig. 3.8, that is at $\hbar\omega_c = 1.935 Ryd^*$ and $\hbar\omega_c = 2.275 Ryd^*$, respectively.

Right at this critical magnetic field and for vanishing interdot tunneling the ground state is degenerate with $|I_z = \pm 1/2\rangle$ and is separated from the lowest excited state by the excitation energy $\Delta E = 0.141 Ryd^*$ (for $M = -3, S = S_z = 1.5$) and $\Delta E = 0.075 Ryd^*$ (for $M = -5, S = S_z = 1.5$). These excitation energies set an upper limit for the validity regime of Eq. (3.17) as function of the interdot coupling.

The interplay between interdot coupling and Coulomb interaction shifts the critical magnetic fields in Fig. 3.8 a) and b). In the subspace specified by $M = -5, S = S_z = 1.5$ and depicted in Fig. 3.9 (b), the parity crossings even disappear completely for interdot couplings larger than $\Delta_{sas} > 0.094 Ryd^*$, while in the subspace $M = -3, S = S_z = 1.5$ depicted in Fig. 3.9 (a) the transition continuously shifts to higher magnetic fields.

The lower column of Fig. 3.9 shows that the parity crossings of the symmetric double dot cause strong spontaneous charge localizations in the presence of a tiny asymmetry. We see that the maximum height of the polarization peak decreases with increasing interdot tunneling, due to the different structure of the parity eigenstates. Furthermore the width of the polarization peaks shrinks with increasing interdot tunneling, which is also explained by Eq. (3.17), since the energy splitting between the parity eigenstates scales with Δ_{sas} and hence the regime, where the asymmetry effectively couples the parity eigenstates, depends on the ratio V_Z/Δ_{sas}. Thus the decrease of the polarization width with increasing interdot tunneling is complementary to Fig. 3.6 where we studied the polarization as function of the asymmetry V_Z. Finally we note that due to the subtle interplay between interdot coupling and Coulomb interaction there is a small regime of interdot tunnel couplings for $M = -5, S = S_z = 1.5$, where the parity eigenstates cross twice. This leads to two localization peaks in the presence of a slight asymmetry in Fig 3.9 d) for $\Delta_{SAS} = 0.0932$.

In the last part of this subsection we show how the magnetic-field dependent charge localization is manifest in the electron density $\rho_\pm(\vec{r}_0) = \langle\, |\pm\rangle \langle\pm|\, \delta(\vec{r} - \vec{r}_0)\, \rangle$ which specifies the

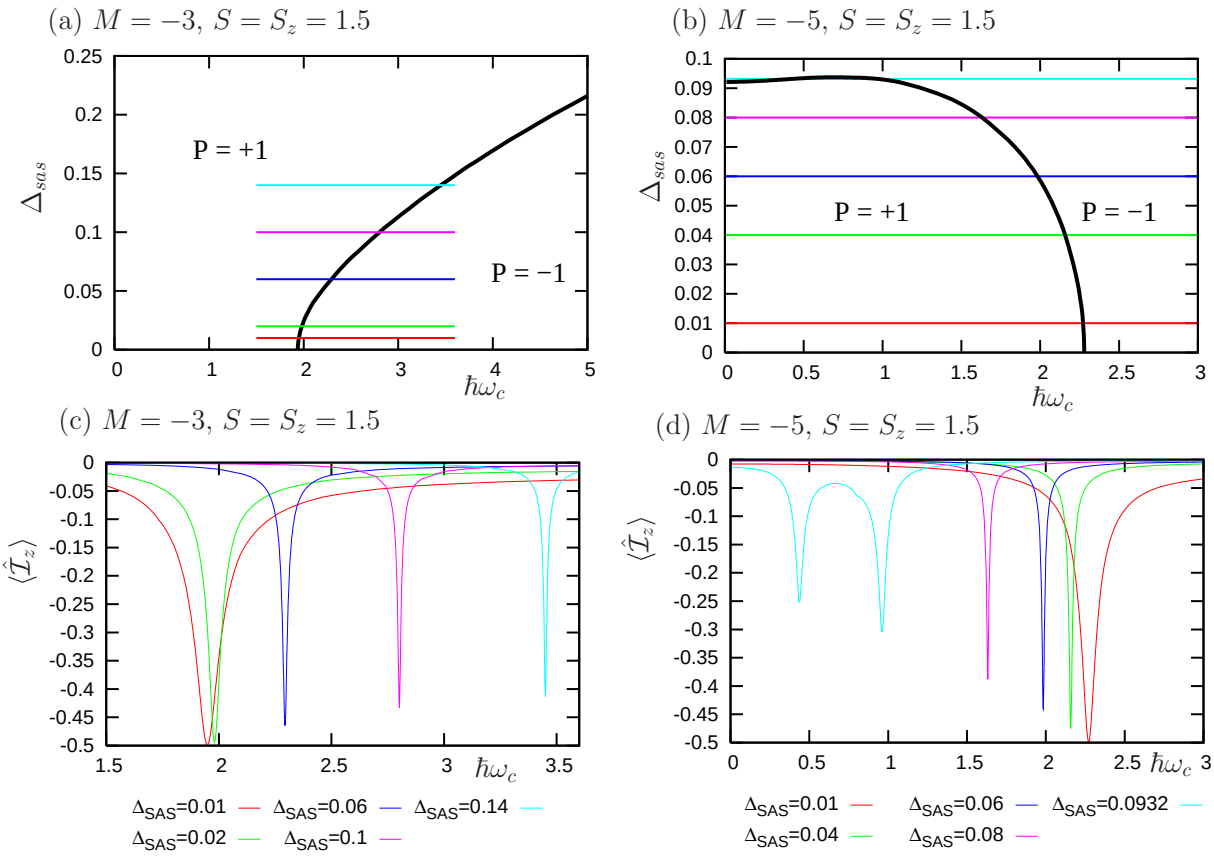

Figure 3.9: *(a) Black line shows the dependence of the critical magnetic field (defined by the parity-crossing) on the interdot coupling in the subspace $M = -3$, $S = 1.5 = S_z$. (c) Magnetic field sweep of the average charge polarization in the presence of a tiny level asymmetry between the dots. At the critical magnetic field a strong charge polarization builds up. Parameters of the magnetic field sweeps are shown by colored lines in (a). Fig. (b),(d) show the corresponding data for subspace $M = -5$, $S = 1.5 = S_z$. Parameters: $\hbar\omega_0 = 0.5$, (a) $d = 2.6a_0^*$, $V_Z = 0$ (b) $d = 2.a_0^*$, $V_Z = 0$ (c) $d = 2.6a_0^*$, $V_Z = 10^{-4}$ (d) $d = 2.a_0^*$, $V_Z = 10^{-4}$. Energies given in units of Ryd*.*

probability density to find an electron at the position $\vec{r}_0$ in dot $\pm$. Each row of Fig. 3.10 shows the electron densities in the upper dot (i.e $\rho_+(r/l)$) and the lower dot (i.e. $\rho_-(r/l)$) for three different magnetic fields. Due to the rotational symmetry of the double dot, the electron density only depends on the radial coordinate r that measures the distance from the center. The norm of the electron density is $2\pi l^2 \int (\rho_+(r^*) + \rho_-(r^*))dr^* = N_e$ where N_e is the electron number and $r^* = r/l$. We see from Fig. 3.10 that at magnetic fields far away from the anticrossing, the electron densities in the upper and lower dot are approximately the same (which is exactly true for parity eigenstates) while at the anticrossing crossing they differ strongly. At the critical magnetic field two electrons are in the lower dot and the upper dot is only singly occupied. The two electrons in the lower dot try to avoid each other which yields a torus-like density in the lower dot and the single electron in the

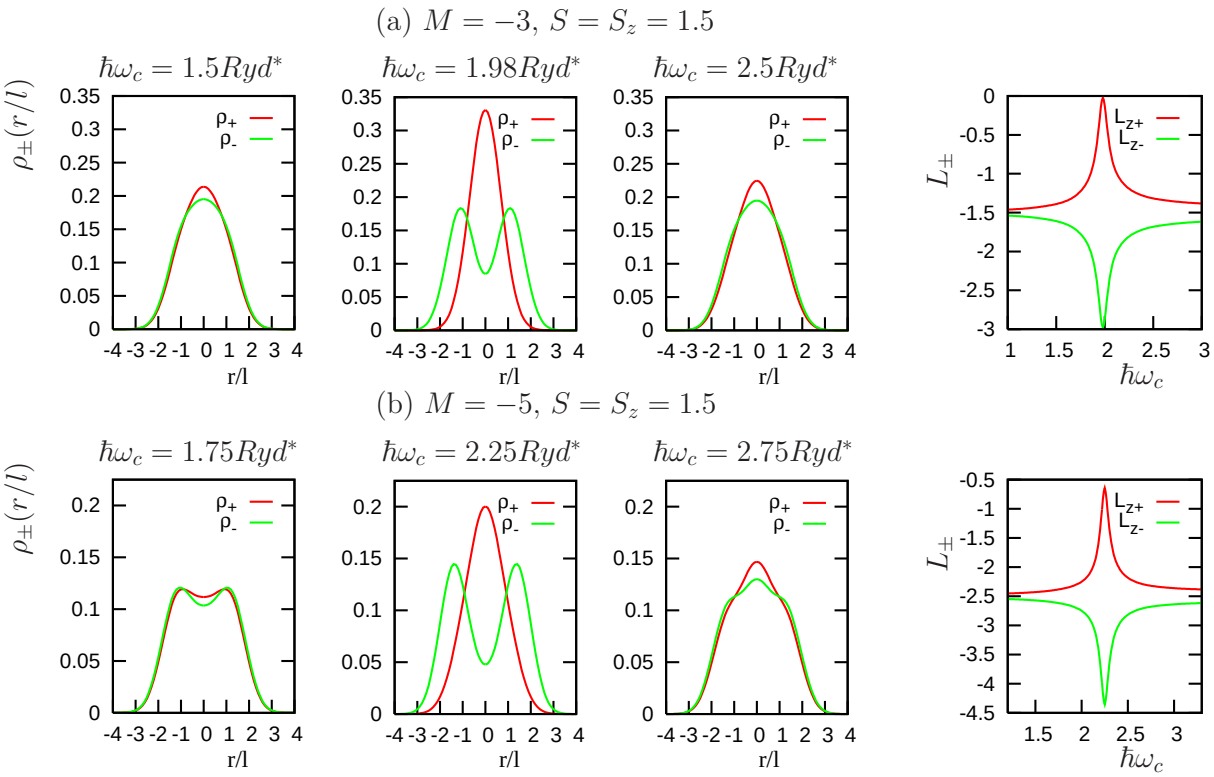

Figure 3.10: *The electron densities of the three-electron ground state for the lower ρ_- and upper ρ_+ dot before, right at, and after the localization peak. The right column shows the expectation value of the angular momentum in the lower L_- and the upper L_+ dot as function of the magnetic field. Parameters $\hbar\omega_0 = 0.5 Ryd^*$, $\Delta_{sas} = 0.02 Ryd^*$, $V_Z = \Delta_{sas}/100$ and $d = 2.0 a_0^*$ for $M = -5$ and $d = 2.6 a_0^*$ for $M = -3$.*

upper dot sits in the potential minimum. This is also visible in the expectation values of the angular momentum per dot, which obey the relation $L_+ + L_- = M$. The two electrons sitting in the same dot carry nearly all the angular momentum available in order to reduce the Coulomb interaction by increasing their mutual distance.

3.3.3 Charge localization in the three-electron ground state

In this subsection we discuss for which parameters the parity crossing arising in symmetric dots (or respectively the charge localization found in slightly asymmetric dots) appears in the three-electron ground state. Therefore we determine for different confinement strengths the quantum numbers (M, S, S_z, P) of the three-electron ground state of a symmetric double dot as function of the layer distance d and the magnetic field $\hbar\omega_c$. The result is depicted in Fig. 3.11. Like in Fig. 3.4 we fix the interdot tunneling energy to a small value, here $\Delta_{sas} = 0.02 Ryd^*$, independent of the layer distance. Within this assumption transitions in the eigenspectrum are mainly determined by the Coulomb interaction, which

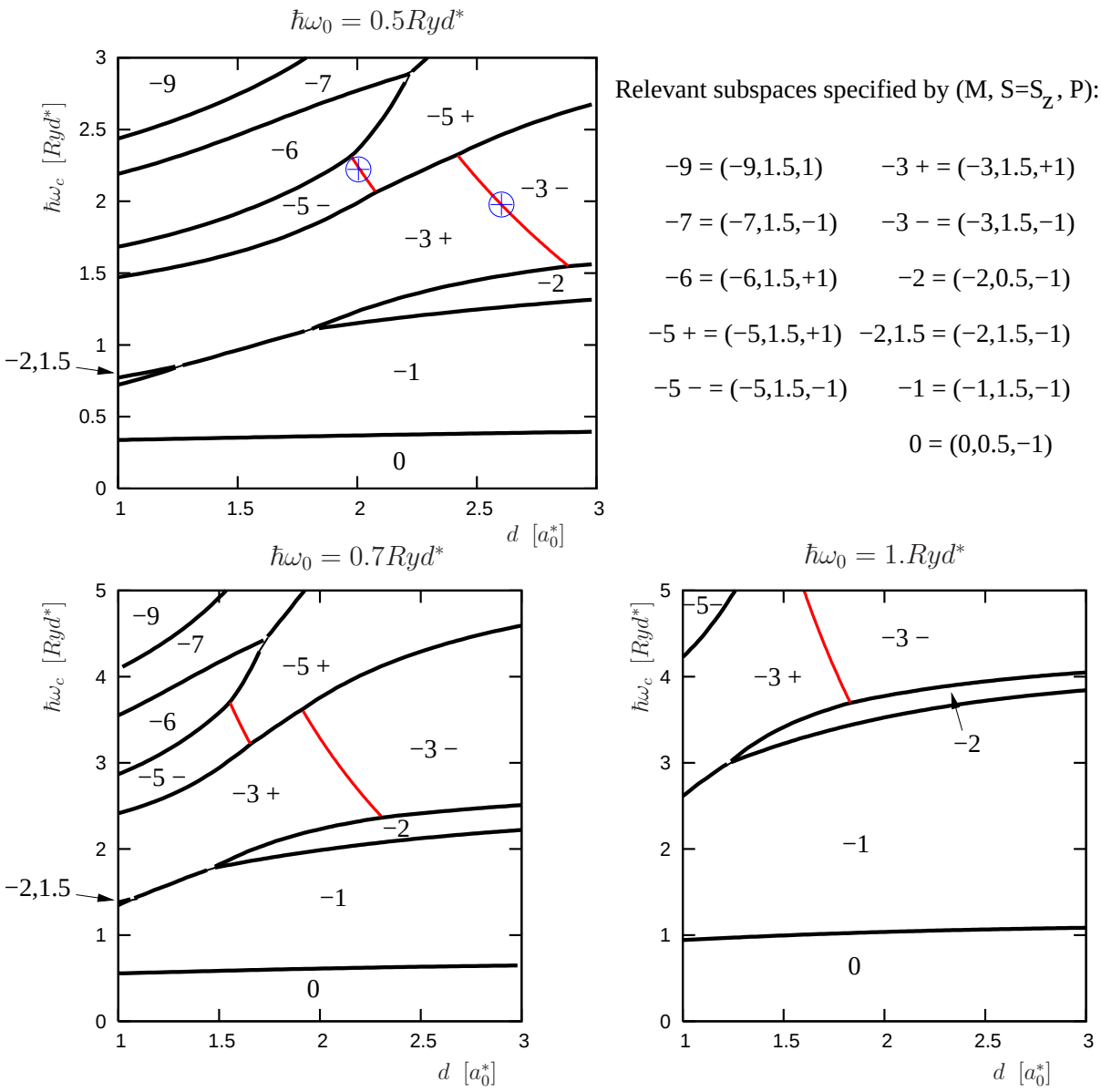

Figure 3.11: *Quantum numbers $(M, S = S_z, P)$ of the three-electron ground state for various confinement strengths and perfectly symmetric dots as function of the magnetic field and layer distance. The labeling of the subspaces is explained in the upper right corner. The black lines separate regions belonging to different subspaces M, S, S_z, while the red lines indicate ground state transitions where only the parity P is changed. The blue crosses for $\hbar\omega_0 = 0.5Ryd^*$ indicate the parameters where the charge localization occurs in Fig. 3.2. The interdot coupling is fixed to $\Delta_{sas} = 0.02Ryd^*$.*

is always much larger than the interdot coupling. The small interdot coupling chosen in Fig. 3.11 is maybe unrealistic for small layer distances, however, the parity crossing appears

in a broad region of the layer distance with values of $1.5a_0^* < d < 2.8a_0^*$ depending on the confinement strength.

The black lines in Fig. 3.11 illustrate transitions where the angular momentum is increased with increasing magnetic field, while the red lines indicate transitions where only the (pseudospin) parity is changed. As explained at the beginning of this section (see page 48) transitions to states with higher angular momentum are based on the effect that the Coulomb energy increases with increasing magnetic field while the single-particle level spacing decreases. At some critical magnetic field, it is therefore favorable to increase the angular momentum in order to reduce the Coulomb energy by increasing the extension of the wavefunction. Since the Coulomb energy (mainly interdot Coulomb energy) decreases with the layer distance d these transitions shift to higher magnetic fields for increasing layer distance.

We note that with increasing confinement the ground-state transitions move to higher magnetic fields and lower layer distances, since the competition between the single-particle spacing and the Coulomb energy depends also on the ratio ω_c/ω_0 in addition to ω_{eff}. Furthermore, the layer distance has to be compared with the characteristic confinement length $l \propto 1/\sqrt{\omega_{eff}}$. Thus the critical magnetic fields of lateral transitions increase with increasing confinement while the critical layer distances decrease.

We have already shown in Fig. 3.2 that parity crossings (for symmetric dots) or anticrossings (for slightly asymmetric dots) found in a subspace of fixed M, S, S_z in a magnetic field sweep can occur in the three-electron ground state. Fig. 3.11 shows a systematic determination of the range of layer distances where the parity crossings found in the subspaces with $M = -3$ or $M = -5$ and $S = S_z = 1.5$ take place in the three-electron ground state. The condition that the crossing has to occur in the ground state restricts the possible parameters of the spontaneous localization as illustrated in Figs. 3.12 and 3.13.

Fig. 3.12 characterizes the charge polarization in the three-electron ground state for different confinement strengths $\hbar\omega_0$ and interdot tunneling energies Δ_{sas}. The lengths of the lines depicted in Fig. 3.12 are defined by the condition that the ground state is in the subspace $M = -3, S = 1.5 = S_z$ at the critical magnetic field. The polarized three-electron states are therefore the lowest eigenstates of the double dot and are separated from the excited states (which can be in any subspace M, S, S_z) by the energy gap depicted in the central row of Fig. 3.12. Finally the lowest row in Fig. 3.12 illustrates the charge polarization of the three-electron ground state at the critical magnetic fields. The upper row of Fig. 3.12 combines the information presented in Figs. 3.4 and 3.9. The critical magnetic field decreases with increasing interlayer distance and increases with increasing interdot tunnel coupling. However, the additional information of Fig. 3.12 is that the charge polarization occurs in the three-electron ground state for a broad regime of interdot couplings and in particular for significantly larger interdot tunneling than the one used in Fig. 3.2. Furthermore the charge localization $\langle \hat{\mathcal{I}}_z \rangle$ at the critical fields shown in the lowest row of Fig. 3.12 is always close to $-\frac{1}{2}$ although it slightly decreases with increasing interdot tunneling as discussed in the context of Fig. 3.9. Important to note is the relative large value of the excitation gap shown in the second row of Fig. 3.12. Its maximum value is given by

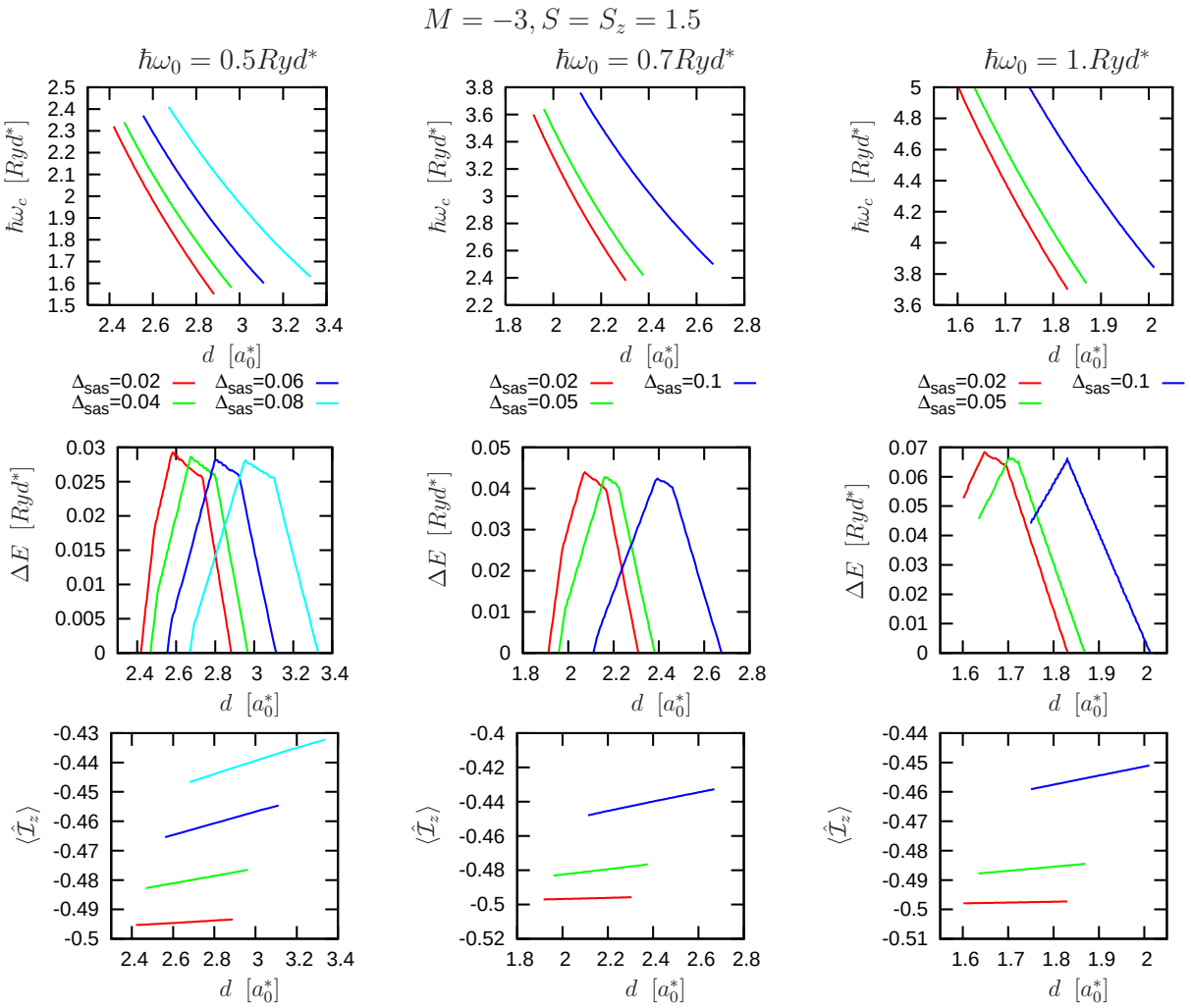

Figure 3.12: *Closer look at parity crossings and charge polarizations in the three-electron ground state. Length of lines defined by the condition that the ground state is in the subspace* $M = -3, S = 1.5 = S_z$ *at the critical magnetic field (compare with Fig. 3.11). Upper row: Dependence of critical magnetic field on layer distance for various coupling strengths* Δ_{sas} *and confinements. Central row: Lowest excitation energy at the critical magnetic field from the polarized states to a three-electron state in any subspace* (M, S, S_z)*. Lowest row: Charge polarization at the critical magnetic field in the presence of a tiny asymmetry* $V_Z = 5 * 10^{-4}$.

$0.03 - 0.07 Ryd^*$ depending on the confinement. This corresponds to voltages of $0.18 - 0.42$ meV or temperatures of $2.0 - 4.8$ Kelvin (see Table 2.1), so that the manifestation of the charge-polarized ground state in the transport characteristics of the double dot is well accessible as will be discussed in the next section. The stability of the $M = -3, S = S_z = 1.5$ state can be argued by its special meaning as realization of the maximum density droplet [57].

Fig. 3.13 is closely related to Fig. 3.12. The lengths of the lines in Fig. 3.13 are now defined

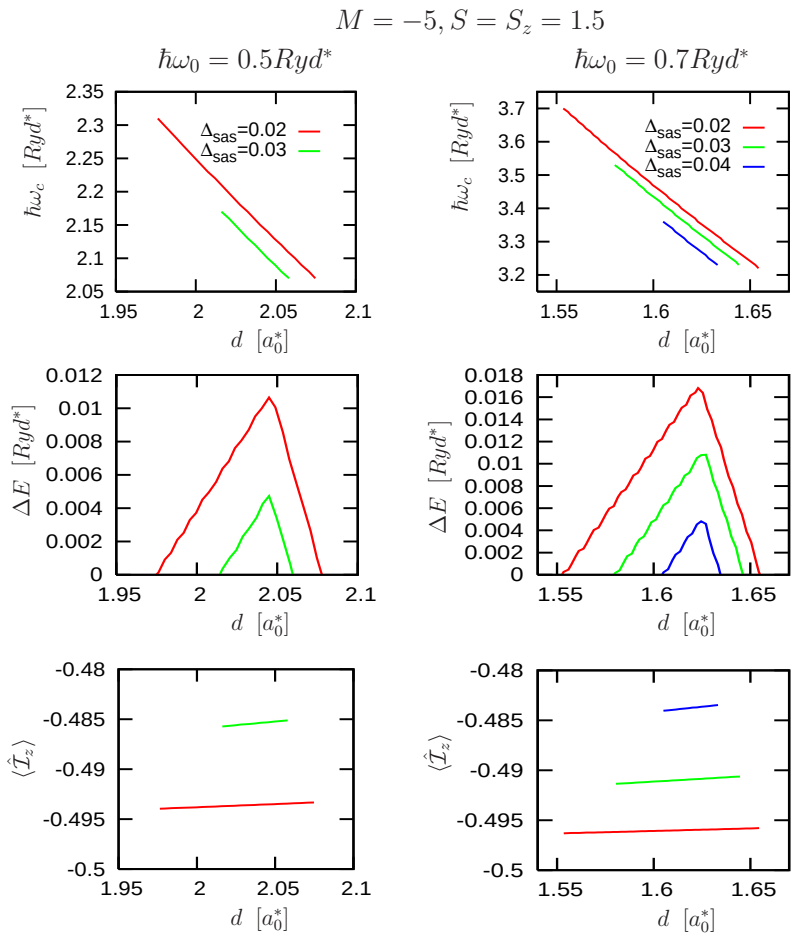

Figure 3.13: *Same as in Fig. 3.12, but for ground state transitions where the lateral quantum numbers are left unchanged at* $M = -5, S = 1.5 = S_z$. *The values of the interdot couplings are specified in the upper graph of each column. Small wiggles are only due to finite numerical precision.*

by the condition that the ground-state is in the subspace $M = -5, S = 1.5 = S_z$ at the critical magnetic field. The major difference to the results depicted in Fig. 3.12 is the much smaller excitation gap. It is already about three times smaller at $\Delta_{sas} = 0.02 Ryd^*$ than in the case of $M = -3, S = 1.5 = S_z$ and furthermore it decreases rapidly with increasing interdot tunneling in contrast to the case of $M = -3, S = 1.5 = S_z$. For $\Delta_{sas} > 0.04$ Ryd^* ($\Delta_{sas} > 0.06$ Ryd^*) the parity crossings does no longer appear in the ground state for $\hbar\omega_0 = 0.5 Ryd^*$ ($\hbar\omega_0 = 0.7 Ryd^*$). For the parameters chosen in Fig. 3.2 (a) and (b) the energy gap at the parity-anticrossing is about $0.004 Ryd^*$ and $0.03 Ryd^*$, respectively.

3.4 Pseudospin blockade

Transport spectroscopy is a powerful tool to study the eigenspectrum of quantum dot systems. In the regime of weak external coupling the effect of the contacts on the eigenspectrum of the interacting dot system can be neglected and the transport through the double dot can be described by a master equation with transition rates obtained by Fermi's golden rule as shown for a single dot in subsection 2.4.1.

For a double dot coupled in series to the external reservoirs and with a rather weak interdot tunnel coupling, the left reservoir couples only to the left and the right dot couples only to the right reservoir, respectively. Thus the external coupling will be strongly modified by the charge polarization discussed in the last section. We will show, that transitions including a strongly charge-polarized state effectively decouple from one of the reservoirs leading to a pseudospin blockade of the current through the double dot. The mechanism is closely related to the spin blockade found in single dots [29] and has been published in references [3, 4].

In the next subsection we discuss how the serial geometry and the eigenspectrum of the double dot can be included in the master equation introduced in subsection 2.4.1. In subsection 3.4.2 we then show how the current through the double dot is strongly suppressed at the critical magnetic fields where the three-electron ground state is polarized. Furthermore we discuss how an increasing transport voltage increases the asymmetry between the dots and thus leads to negative differential conductances.

3.4.1 Master equation for transport through a serial double dot

In fact, transport through a double dot coupled in series to external contacts is described by the master equation and the current formula introduced for a single dot in subsection 2.4.1 in Eqs. (2.35), (2.39) and (2.41). However in the calculation of the transition rates given in Eq. 2.35 one now has to take into account the serial transport geometry and the eigenspectrum of the double dot.

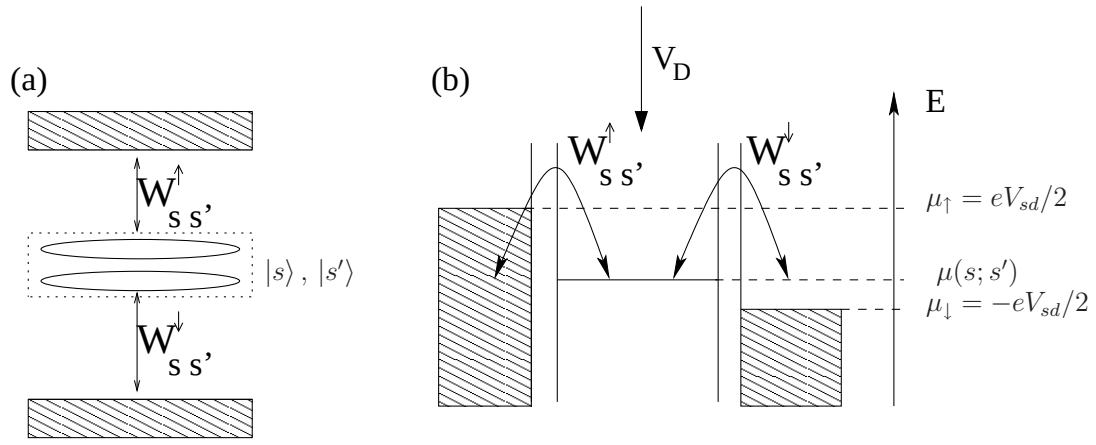

Figure 3.14: *Visualization of the serial transport through double dot.* $|s\rangle$, $|s'\rangle$ *denote eigenstates of the double dot including the interdot coupling, and hatched areas denote the contacts. (a) Different treatment of external coupling and interdot tunneling. (b) Energy profile for transport through double dot including a single transport channel. Transport channels are continously shifted in energy by changing the electrostatic potential* V_D *on the double dot.*

Within our approach we thus start with the eigenspectrum of the double dot including in-

terdot tunneling and then we include the external coupling to lowest order. This approach is visualized in Fig. 3.14. Fig. 3.14 (a) illustrates the different treatment for the interdot coupling and the external coupling. In a first step the eigenstates of the double dot (including the interdot tunnel coupling exactly) are determined. They are called $|s\rangle$, $|s'\rangle$ in the following. Then a lowest order expansion in the external coupling is performed, leading to the transition rates $W^r_{s\,s'}$, where $r \in \{\uparrow, \downarrow\}$ labels the dot and due to the serial geometry also its corresponding reservoir. Within this approach it is assumed that the double dot is never in a coherent superposition of eigenstates, but is described by a mixture of eigenstates. Superpositions of eigenstates are neglected since the external coupling is several orders of magnitude smaller than the interdot coupling as we will discuss in context of Fig. 3.17 in the following subsection. (In the next chapter we study the case when the external coupling exceeds the interdot coupling and discuss the evolution of superpositions of eigenstates there.) Fig. 3.14 (b) shows the energy profile for transport through the double dot. In analogy to the case of single dots, the eigenspectrum of the double dot determines the discrete energies of the transition channels $\mu(s;s') = E_{s'} - E_s$ corresponding to transitions between the N-electron state $|s\rangle$ and the (N+1)-electron state $|s'\rangle$. As discussed in the context of Fig. 3.1 a side gate around the double dot structure can be used to continuously change the electrostatic potential V_D on the double dot, which is assumed to be the same on both dots. Therefore the eigenstates of the double dot are unaffected by the constant electrostatic potential, V_D, while the eigenenergies shift proportionally to V_D, i.e. $E_s(V_D) = E_s(V_D = 0) - eV_D N(s)$, where $N(s)$ describes the number of electrons of state $|s\rangle$. Thus the transport channels $\mu(s;s') = E_{s'}(V_D = 0) - E_s(V_D = 0) - eV_D$ can be continuously shifted by the electrostatic potential V_D on the dot, as indicated in Fig. 3.14.

We now show how the serial geometry enters the transition rates. For the double dot discussed here a single-particle orbital l is specified by $l = n, m, \alpha$, where n, m are respectively the principal quantum number and the angular momentum of the Fock-Darwin states describing the lateral motion, while α denotes the pseudospin, which labels the dot. The single-particle orbitals l enter the spectral functions $\Gamma^r_{l_1 l_2}(\omega)$ and $\Gamma^r_{ss's's}(\omega)$ defined in Eq. (2.34). For a double dot coupled in series, the reservoir index also represents a pseudospin since only the upper (lower) reservoir couples to the upper (lower) dot, so that we will label the reservoirs now by $r \in \{\uparrow, \downarrow\}$ and will use either r or α to denote the vertical degree of freedom. The mapping on the lateral geometry used in subsection 2.4.1 is done by replacing $L \leftrightarrow \uparrow$ and $R \leftrightarrow \downarrow$. With the assumptions leading to Eq. (2.36) we obtain for the spectral functions of the coupling strengths:

$$\begin{aligned} \Gamma^r_{l_1 l_2}(\omega) &= \Gamma^r \delta_{l_1 l_2} \delta_{\alpha(l_1) r} \\ \Gamma^r_{ss's's}(\omega) &= \Gamma^r S^r_{s\,s'} \\ S^r_{s\,s'} &= \sum_{n,m,\sigma} \left| \langle s| \, c_{nmr\sigma} \, |s'\rangle \right|^2 = \sum_{n} \left| \langle s| \, c_{n\bar{m}r\bar{\sigma}} \, |s'\rangle \right|^2 . \end{aligned} \tag{3.19}$$

Here $\alpha(l_1)$ denotes the pseudospin of the orbital l_1. Furthermore, $\bar{m} = M(|s'\rangle) - M(|s\rangle)$ and $\bar{\sigma} = S_z(|s'\rangle) - S_z(|s\rangle)$ denote angular momentum and the spin orientation of the tunneling electron, that are determined by the conserved total angular momenta $M(|s\rangle), M(|s'\rangle)$ and

spins $S_z(|s\rangle), S_z(|s'\rangle)$ of the states $|s\rangle$ and $|s'\rangle$. The important difference to the transition rates given in Eq. (2.36) is, that now the spectral weight $S^r_{s\,s'}$ depends on the reservoir/dot index $r = \alpha$.

In conclusion we obtain the following master equation and current formula [70]:

$$\begin{aligned} W_{ss'} &= \sum_\alpha (W^{\alpha+}_{s\,s'} + W^{\alpha-}_{s\,s'}) \\ W^{\alpha+}_{s's} &= \Gamma^\alpha f_\alpha(E_{s'} - E_s) S^\alpha_{s\,s'}\,; \quad W^{\alpha-}_{s's} = \Gamma^\alpha f^-_\alpha(E_s - E_{s'}) S^\alpha_{s'\,s} \\ 0 &= \frac{d}{dt}P_s = \sum_{s'} (W_{ss'}P_{s'} - W_{s's}P_s) \qquad (3.20) \\ 1 &= \sum_s P_s \\ I &:= -e\frac{dN_\uparrow}{dt} = e\sum_{s,s'} \left(W^{\uparrow+}_{s's} P_s - W^{\uparrow-}_{ss'} P_{s'} \right)\,. \qquad (3.21) \end{aligned}$$

3.4.2 Manifestations of charge localization in transport spectra

We start with the discussion of linear transport through the double dot corresponding to an occupation of the double dot varying between two and three electrons.

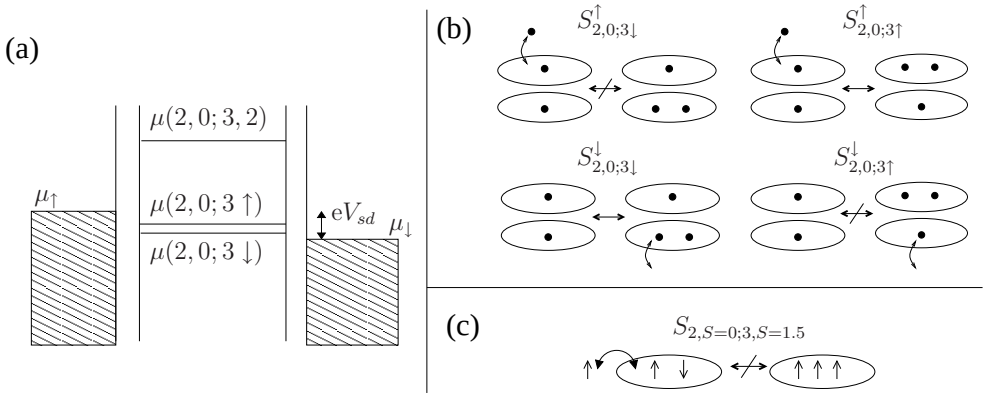

Figure 3.15: *(a) Energy profile for the transport through the double dot at the critical magnetic field, where the three-electron ground state and first excited state are strongly charge-polarized. Even though the two transport channels $\mu(2,0;3\downarrow)$, $\mu(2,0;3\uparrow)$ are inside the transport window the current through the double dot is blocked. (b) The blocking mechanism is based on a pseudospin blockade, which leads to a decoupling of the transport channel from one of the reservoirs due to a vanishing spectral weight. (c) Analogy to the spin blockade of single dot by identifying the meaning of real spin and pseudospin for selection rules.*

Fig. 3.15 (a) illustrates the energy profile at the critical magnetic field where the three-electron ground state (first excited state) is strongly charge-polarized in the lower (upper)

dot. According to their polarization we call these states $|3\downarrow\rangle$ and $|3\uparrow\rangle$, respectively. According to Fig. 3.15 (a) both transition channels $\mu(2,0;3\downarrow)$ and $\mu(2,0;3\uparrow)$ are inside the transport window. However even though the transitions are energetically allowed, the current through the double dot is blocked which is explained by the pseudospin blockade depicted in Fig. 3.15 (b). Essential for the blocking mechanism is the serial geometry and the fact that already for very weak asymmetry the relevant three-electron states are strongly polarized at the critical field, while the two-electron ground state is completely unpolarized. In this situation the spectral weights $S^{\uparrow}_{2,0;3\downarrow}$ and $S^{\downarrow}_{2,0;3\uparrow}$ vanish and thus also the transition rates $W^{\uparrow}_{2,0;3\downarrow}$ and $W^{\downarrow}_{2,0;3\downarrow}$. For the situation depicted in Fig. 3.15 (a) a current can only flow through the double dot, if it alternately occupies the two-electron ground-state $|2,0\rangle$ and either of the three-electron states $|3\downarrow\rangle, |3\uparrow\rangle$. In order to explain the pseudospin blockade depicted in Fig. 3.15 (b) we assume for a moment that the double dot is in the two-electron ground state $|2,0\rangle$. An electron entering the upper dot cannot cause a transition to the three-electron ground state $|3\downarrow\rangle$ since this state has only one electron in the upper dot, see Fig. 3.15 (b). Therefore, the electron entering the upper dot can only cause a transition to the nearly degenerate first excited state $|3\uparrow\rangle$ which is separated in energy by the small asymmetry V_Z. For a current to flow, the electron in the lower dot should leave the state $|3\uparrow\rangle$ and enter the lower reservoir. However, this is again impossible, since this would leave the double dot in a two-electron state with both electrons in the upper dot, which is forbidden for energy reasons. Mathematically, this transition is forbidden by the vanishing spectral weight $S^{\downarrow}_{2,0;3\uparrow} = 0$ indicated in Fig. 3.15 (b). Since the state $|3\uparrow\rangle$ is an eigenstate of the double dot it will not evolve into state $|3\downarrow\rangle$, so that the double dot is stuck in state $|3\uparrow\rangle$ and current is blocked. The blocking mechanism described here for serial transport through double dots resembles strongly the spin blockade found for single dots, which is depicted in Fig. 3.15(c). This is an additional advantage of the pseudospin description of the vertical motion.

We now comment on the different treatment of interdot tunnel coupling on the one side and tunnel coupling to the external reservoirs on the other side, as discussed previously in the context of Fig. 3.14 in the previous subsection. In particular we emphasize that the blocking mechanism discussed here also occurs if both tunnel couplings, the interdot coupling as well as the external coupling, are treated in lowest order perturbation theory. In that case an electron passes the double dot in three sequent processes. First it enters the upper dot, causing a transition from the two-electron state $|N_e = 2, I_z = 0\rangle$ to the three-electron state $|N_e = 3, I_z = 1/2\rangle$. In the second step, it tunnels from the upper to the lower dot thus causing a transition from $|N_e = 3, I_z = 1/2\rangle$ to $|N_e = 3, I_z = -1/2\rangle$. This process is caused by the interdot tunneling $\hat{\mathcal{H}}_T$ and is governed by the matrix element $\langle N_e = 3, I_z = -1/2|\,\hat{\mathcal{I}}_x\,|N_e = 3, I_z = 1/2\rangle$. Finally the electron leaves the lower dot to the lower reservoir, causing a transition from $|N_e = 3, I_z = -1/2\rangle$ to $|N_e = 2, I_z = 0\rangle$. Now as illustrated in Fig. 3.8 the matrix element $\langle N_e = 3, I_z = -1/2|\,\hat{\mathcal{I}}_x\,|N_e = 3, I_z = 1/2\rangle$ disappears at the critical magnetic field, leading to a complete suppression of the interdot tunneling. Consequently the current through the double dot vanishes. In the following we apply the master equation approach to study the dependence of the blocking mechanism

on the external magnetic field and on the applied transport voltage.

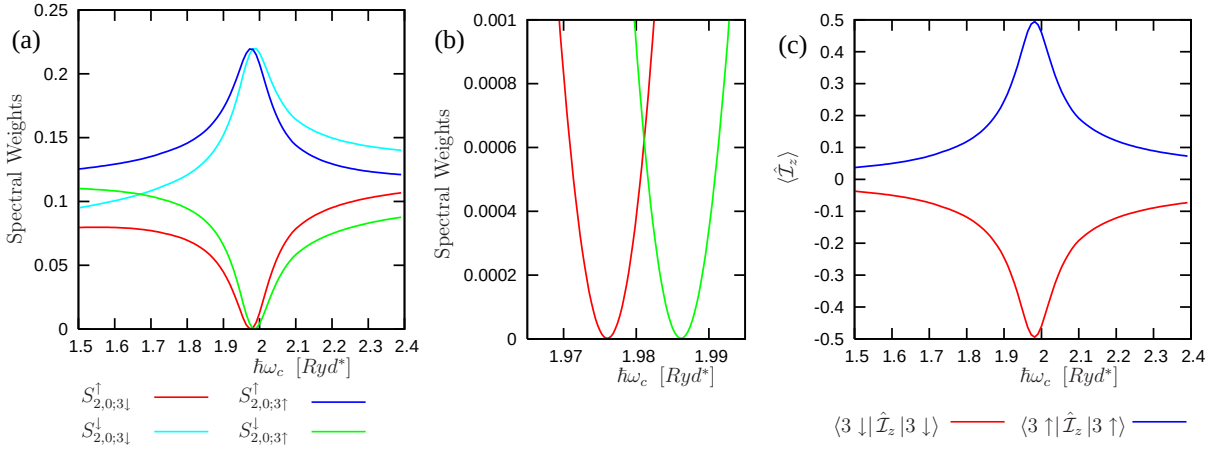

Figure 3.16: *(a) Magnetic field dependence of spectral weights shown in Fig 3.15(b). The charge polarization of the three-electron states* $|3,\downarrow\rangle$, $|3,\uparrow\rangle$ *at* $\hbar\omega_c \approx 1.98 Ryd^*$ *leads to a complete suppression of the coupling between reservoir and the singly occupied dot. (b) Spectral weights vanish at slightly different magnetic fields. (c) Expectation of the z-component of the pseudospin in the ground and first excited three-electron state (see Fig. 3.6). Parameters:* $\hbar\omega_0 = 0.5 Ryd^*, d = 2.6 a_0^*, \Delta_{SAS} = 0.02 Ryd^* = 100 V_Z$.

The blocking mechanism as depicted in Fig 3.15 (b) relies on the strong charge polarizations of the three-electron ground state $|3\downarrow\rangle$ and first excited state $|3\uparrow\rangle$ at a critical magnetic field. In order to understand the magnetic-field dependence of the blocking mechanism we first discuss the situation sufficiently far away from the critical magnetic field, where the eigenstates are only weakly disturbed by the slight asymmetry. For symmetric dots the spectral weights $S^{\uparrow/\downarrow}_{s\,s'}$ (defined in Eq. (3.19)) - characterizing the coupling of a transport channel $\mu(s,s')$ to the upper and lower reservoir respectively - are always the same. Mathematically this follows from the parity conservation in symmetric dots which allows to transform the spectral weights into each other. Using Eq. (3.19) we obtain for a symmetric double dot:

$$\begin{aligned} S^{\uparrow}_{s\,s'} &= \sum_n \left|\langle s|\, c_{n\bar{m}\uparrow\bar{\sigma}}\, |s'\rangle\right|^2 = \sum_n \left|\langle s|\, c_{n\bar{m}\uparrow\bar{\sigma}}\hat{\mathcal{P}}\, |s'\rangle\right|^2 = \sum_n \left|\langle s|\, \hat{\mathcal{P}} c_{n\bar{m}\downarrow\bar{\sigma}}\, |s'\rangle\right|^2 = \\ &= \sum_n \left|\langle s|\, c_{n\bar{m}\downarrow\bar{\sigma}}\, |s'\rangle\right|^2 = S^{\downarrow}_{s\,s'}\,. \end{aligned} \tag{3.22}$$

Fig. 3.16 a) shows the magnetic-field dependence of the spectral weights in presence of a slight asymmetry. With increasing charge-polarization of the three-electron states, depicted in Fig. 3.16 c), the singly occupied dot decouples more and more from the corresponding reservoir while the doubly occupied dot couples stronger to its reservoir. Zooming closer to the critical magnetic field of the charge polarization, one observes that for each channel

the singly occupied dot decouples completely at a characteristic field as illustrated in Fig. 3.16 b). These characteristic fields are slightly different for the two channels.

We note that - since the suppression of the spectral weights is determined by the polarization of the three-electron states - the magnetic field regime of the blockade is determined by the ratio V_Z/Δ_{sas}, which determines the width of the polarization peak (see discussion of Figs. 3.6 and 3.9).

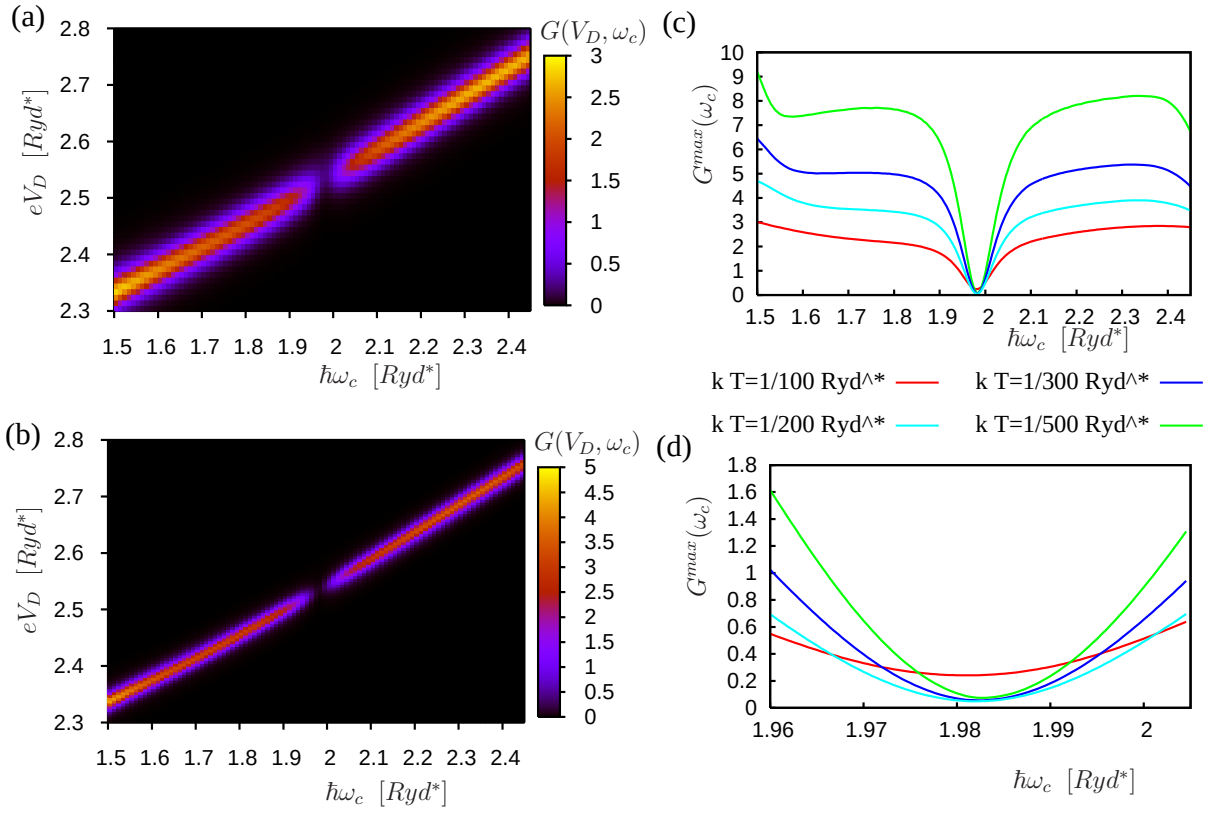

Figure 3.17: *Magnetic field dependence of Coulomb peak in conductance $G = I/V_{sd}$ in units of $e^2\Gamma/\hbar Ryd^*$ for small applied transport voltage $eV_{sd} = 1/200 Ryd^*$. Charge polarization of the three-electron states at $\hbar\omega_c = 1.98 Ryd^*$ leads to a strong suppression of the conductance. Parameters like in Fig. 3.16 and $V_{sd} = 1/200 Ryd^*$, $k_BT = 1/100 Ryd^*$ in (a) and $k_BT = 1/200 Ryd^*$ in (b).*

Fig. 3.17 shows the magnetic field dependence of the Coulomb peak in the conductance through the double dot, corresponding to a transition between the two- and three-electron ground state. The main message of this figure is the strong suppression of the conductance peak around $\hbar\omega_c = 1.98 Ryd^*$, which is due to the pseudospin blockade as explained above. The width of the dip in the conductance is directly connected with the width of the polarization and is therefore determined by the ratio V_Z/Δ_{sas} (see discussion of Fig. 3.6

and 3.9). Fig. 3.17 (c) and (d) show the maximum of the conductance as function of the magnetic field which is reduced by a factor of 10-100 at the critical magnetic field depending on temperature .

According to table 2.1 the temperatures used in the calculation correspond to 140-700 mK and the applied transport voltage corresponds to $V_{sd} = 30\mu$V. Fig. 3.17 illustrates that in the linear transport regime an increase in temperature generally causes a broadening and lowering of the conductance peak as function of the gate voltage [70, 71]. However, this is not the case close to the pseudospin blockade where the broadening of the Fermi-function also allows transitions to excited states which circumvent the blocking mechanism. Therefore, right at the crossing the conductance even increases with increasing temperature as soon as the broadening of the Fermi distribution is of the order of the excitation gap to excited states. According to the data plotted in Fig. 3.12 the excitation gap from the strongly charge-polarized three-electron states to the lowest excitation is given by $\Delta E = 0.03 Ryd^*$ and according to Fig. 3.17 (d) the conductance increases for temperatures above $1/200 k_B T = \Delta E/6$.

In Fig. 3.17 we assume symmetric coupling constants to the left and right reservoir and set the coupling constants to $\Gamma = \Gamma_L = \Gamma_R$. Concerning the magnitude of Γ we note that typical currents through vertical double dots are in the range between picoampère and nanoampère [42, 59, 72] and the average tunneling times $\hbar/\Gamma$ in vertical dot structures are of the order $1 - 100$ns [40]. This corresponds to an external coupling strength in the order of $\Gamma \approx 1 - 100\mu Ryd^* = 10^{-6} - 10^4 Ryd^*$, which is much smaller than the interdot tunneling $\Delta_{sas} > 10^{-2} Ryd^*$ considered here, so that the master equation approach is applicable.

It is important to note that also the next conductance peak - belonging to an occupation on the double dot varying between three and four electrons - will be suppressed at the same critical magnetic field. The selection rules for the transition between the unpolarized four-electron ground state $|4, 0\rangle$ and the strongly polarized three-electron states $|3, \downarrow\rangle, |3, \uparrow\rangle$ lead to $S^{\uparrow}_{3\uparrow;4,0} = S^{\downarrow}_{3\downarrow;4,0} = 0$, which again blocks the linear transport through the double dot, according to the same arguments as stated above.

Fig. 3.18 shows the charge diagrams of the double dot at the critical magnetic field $\hbar\omega_c = 1.985 Ryd^*$ (upper row) and at $\hbar\omega_c = 1.7 Ryd^*$ (lower row). In the left column we assumed that all transport voltage drops across the outer barriers, so that the asymmetry V_Z between the dots is independent of the transport voltage. In contrast, the data shown in the right colum, are obtained by assuming a linear dependence between asymmetry between the dots and the applied voltage $V_Z = eV_{sd}/20$ which is closer to the experimental situation [59]. In a first step we explain the charging diagrams for constant asymmetry (left column). In general a stationary current can flow through the double dot when the ground state channel enters the transport window see Fig. 3.18 (c). However, as we already explained above this is not the case at the critical magnetic field shown in Fig. 3.18 (a) since a pseudospin blockade strongly suppresses the transition rate of the two lowest transport channels. However, with increasing transport voltage, transitions to excited states become possible, which may weaken the blocking mechanism. This happens first when the transport channel $\mu(2, 4; 3, 1)$ aligns with the source reservoir. This improves the exit from

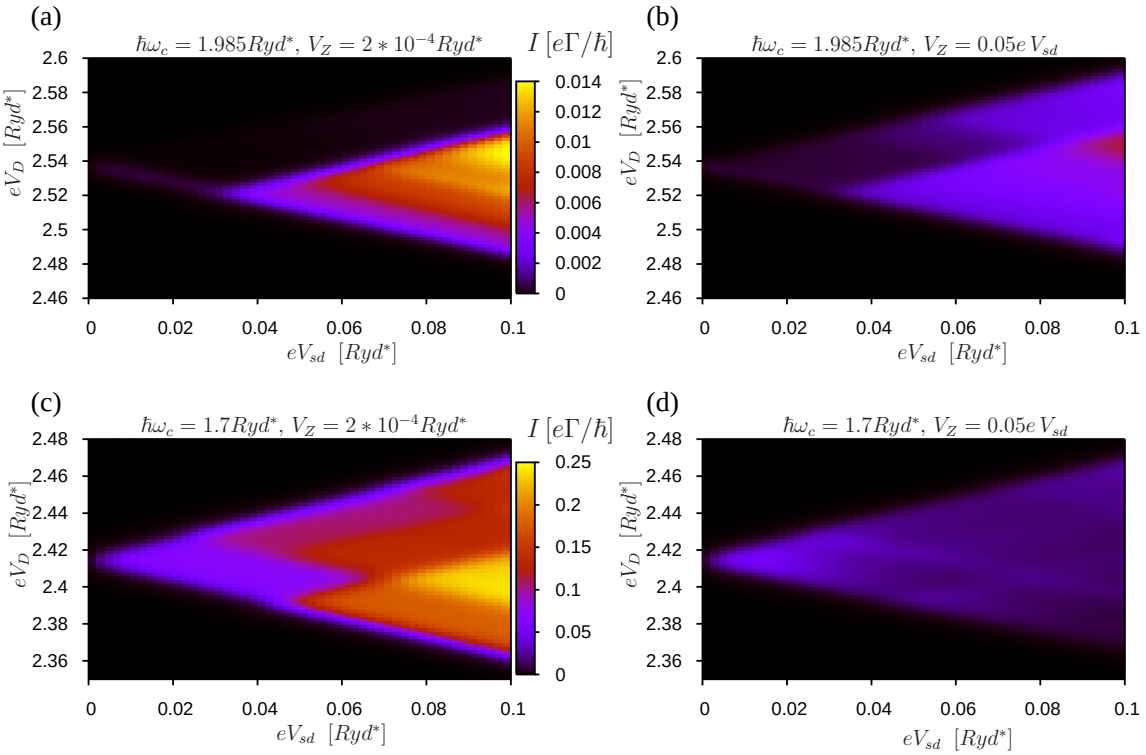

Figure 3.18: *Charge diagrams at the critical magnetic field* $\hbar\omega_c = 1.985 Ryd^*$ *(upper row) and at* $\hbar\omega_c = 1.7 Ryd^*$ *(lower row). In the left column a constant asymmetry is assumed* $V_Z = 2 * 10^{-4} Ryd^*$ *while in the right column the asymmetry is assumed to be proportional to the transport voltage* $V_Z = eV_{sd}/20$*. At the critical magnetic field the current is strongly suppressed (please that scaling differs by factor 20 between upper and lower row). At finite transport voltages the blockade is canceled since transitions to excited states are possible. Left column: (d) The induced asymmetry continuously turns on the pseudospin blockade and leads to regimes of negative differential conductance. Parameters like in Fig 3.16 with* $kT = 0.002 Ryd^*$*.*

the state $|3,1\rangle$ to the drain reservoir since the spectral weight $S^{\downarrow}_{2,4;3,1}$ is more than 2 orders of magnitude larger than $S^{\downarrow}_{2,0;3,1}$. The state $|2,4\rangle$ has $N_e = 2$, $M = -1$, $S = S_z = 1$. We note similarity between the charge diagram Fig. 3.18 (a) revealing the pseudospin blockade and the charge diagrams for spin blockade (see e.g. Ref. [29]) which highlights again the similarity of both blocking mechanisms.

Considering the asymmetry induced by the transport voltage (right column) of Fig. 3.18, we find that it generally reduces the current through the double dot. In Fig. 3.19 (a) we show a line scan of the current plotted in Fig 3.18 (d) at $eV_D = 2.415 Ryd^*$. We find that the current decreases with increasing transport voltage. The reason for this negative differential conductance is not the entry of a new badly conducting channel but rather a continuous decoupling of the ground-state channel due to an increasing polarization of the

three-electron states. The dependence of the relevant spectral weights on the transport voltage are shown in Fig. 3.19 b).

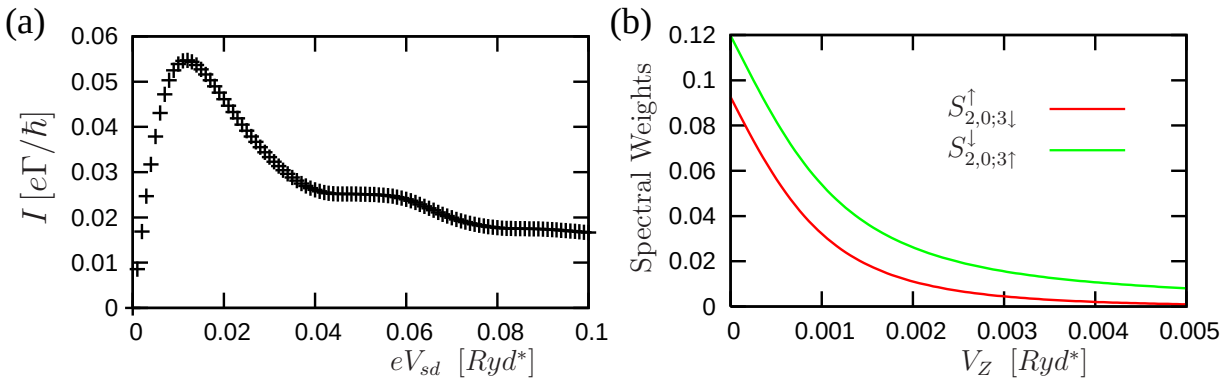

Figure 3.19: *(a) Current as function of the transport voltage at $\hbar\omega_c = 1.7 Ryd^*$ as obtained from a trace of Fig. 3.18 (d) at $eV_D = 2.415 Ryd^*$. The asymmetry V_Z between the dots increases with the transport voltages $V_Z = eV_{sd}/20$ and causes a strong suppression of the spectral weights and the transition rates. Other parameters like in Fig. 3.18 (d).*

3.4.3 Stability of pseudospin blockade

The pseudospin blockade is based on the orbital degree of freedom in vertical direction. In single dots the lateral degree of freedom is strongly affected by relaxation processes due to coupling with acoustic phonons, and the corresponding transition rates are often larger than the external tunnel rate.[40] Therefore, we need to check if the pseudospin blockade can be canceled by phonon induced transitions between the polarized states $|3,\uparrow\rangle$ and $|3,\downarrow\rangle$. In contrast to the lateral motion, where electrons occupy the same volume, the pseudospin orbitals $|\pm\rangle$ describing the vertical motion have no (significant) spatial overlap. We therefore expect that phonons cannot move electrons from the upper to the lower dot and that therefore direct phonon-induced transition between states $|3,\uparrow\rangle$ and $|3,\downarrow\rangle$ are absent.

In the following we substantiate this argument following reference [73]. We assume that the perturbation potential induced by an acoustic phonon with the three-dimensional wave vector $\vec{q}$ is modeled by:

$$V_{ep}(\vec{q}) = e^{i\vec{q}\vec{r}}\lambda_{\vec{q}}(b_{\vec{q}} + b^{\dagger}_{-\vec{q}}) \; .$$

Here $b_{\vec{q}}$ and $b^{\dagger}_{-\vec{q}}$ denote the phonon operators, $\lambda_{\vec{q}}$ a coupling parameter, and $\vec{r}$ a three-dimensional spatial vector. According to Fermi's golden rule the phonon induced transition rate $W^{ph}_{s',s}$ from a state $|s\rangle$ to an energetically lower state $|s'\rangle$ is given by :

$$W^{ph}_{s',s} = \frac{V}{2\pi^2\hbar}\int d^3q |\langle s'|\, V_{ep}(\vec{q})\,|s\rangle\,|^2 \delta(E_s - E'_s - \hbar\omega_{\vec{q}}) \; .$$

Here $\omega_{\vec{q}}$ denotes the phonon frequency and V the volume of the system. If we now come back to the vertical double dot and define the single-particle states $|s\rangle = |nm\alpha\sigma\rangle$ and $|s'\rangle = |n'm'\alpha'\sigma'\rangle$ we find that the matrix element $|\langle s'| V_{ep}(\vec{q}) |s\rangle|^2$ vanishes, if the two states differ in the vertical degree of freedom, $\langle s'| e^{i\vec{q}\vec{r}} |s\rangle = \delta_{\sigma\sigma'}\delta_{\alpha\alpha'} \langle nm| e^{i\vec{q}\vec{r}} |n'm'\rangle$. Thus within the applied approximations a phonon cannot push an electron from the upper to the lower dot or vice versa, so that the pseudospin blockade is stable against electron-phonon interaction. We note that in real structures there is a finite spatial overlap between the "localized" states $|\alpha = \pm 1\rangle$, and the selection rule discussed here is not strictly applicable. However, since we discuss the regime of weak interdot-tunnel coupling this overlap is always small, so that direct phonon induced transitions between the localized states will also be small due to the above considerations. A quantitative study about the influence of phonons on the eigenspectra of a double dot can e.g. be found in reference [74].

3.5 Conclusion

The three-electron ground state of two vertically coupled dots can show a spontaneous charge polarization in a magnetic field sweep. The origin of this effect is the different magnetic field dependence of intra- and interdot Coulomb interaction. At the critical magnetic field the Coulomb interaction effectively turns off the interdot coupling, so that any small level asymmetry between the dots leads to a strongly polarized ground state with two electrons in one dot and only one electron in the other dot. This charge polarization is a pure many-body effect and it strongly influences the transport characteristics of the double dot in a serial geometry. In the linear transport regime the corresponding Coulomb peaks of the current vanish due to a pseudospin-blockade. Additionally broad voltage regions of negative differential conductance appear in the nonlinear transport regime in the vicinity of the critical magnetic field.

In this chapter we clearly identified Coulomb correlations as the driving force for the charge polarization. Our discussion on the electronic structure of parity eigenstates as well as the dependence of the phase diagram as function of the magnetic field and interdot distance indicates that the type of correlations leading to the charge polarization are probably not contained in a Hartree-Fock or density functional approximation. It could be interesting to check this hypothesis by Hartree-Fock or density functional calculations.

4 Probing level renormalization by sequential transport through double quantum dots

In this chapter we investigate the transport properties of a double dot coupled in series to external reservoirs. In contrast to the previous chapter we assume the external coupling to be of the same order as or even larger than the interdot coupling or the level asymmetry between the dots. In that regime a simple master equation approach as used in subsections 2.4.1 and 3.4.1 fails to describe the interplay between the external coupling to reservoirs and the internal dynamics on the double dot.

The main outcome of our studies is that the external coupling renormalizes the level asymmetry between the dots already in the sequential transport regime, where incoherent tunneling events dominate transport. We show that the renormalization is manifest in the current voltage characteristics and in the stability diagram of the double dot. The main results are published in reference [5].

The chapter is organized as follows: In the first section we present the theoretical description of quantum transport in the framework of the real time diagrammatic approach developed by Schoeller *et al.* It allows a systematic expansion of the non-equilibrium dynamics in the order of the external coupling.[22, 26, 75, 76, 77] In the second part of this chapter we apply this approach to the transport through serial double dots.

4.1 Theory of quantum transport

In order to emphasize the general applicability of the presented theory we use the terminology 'local system' in the following as substitute for any interacting quantum dot system. Except of this change in notation the general setup is the same as in Fig. 2.9 on page 24. The real time transport theory generalizes the master equation and the current formula derived in subsections 2.4.1 and 3.4.1 to the intermediate and strong coupling regime. The reduced density operator for the local region and the electric current are again determined by kinetic equations, where the generalized transition rates or self-energies can be expressed by a (rapidly growing) number of irreducible diagrams, which allows a systematic expansion of the current in powers of the external coupling. Recently this technique was applied to study the fingerprints of the excitation spectrum on the Co-tunneling current inside the Coulomb blockade,[78] the noise spectrum and the counting statics of single quantum

dots [79, 80] and chains of dots,[81] as well as the partially coherent dynamics of a single dot, which is weakly coupled to ferromagnetic leads.[82]

The starting point of this approach is again the Hamiltonian (2.26) in subsection 2.4.1 describing a local strongly interacting system which is tunnel-coupled to reservoirs. Similar to Fermi's golden rule, this formalism treats the external coupling as perturbation while the Coulomb interaction on the local system is taken into account exactly. The power of the formalism is that it allows to systematically include contributions of higher orders in the external coupling and that it can be applied for general transport voltages. This approach is thus the complement of a scattering formalism, where the noninteracting problem is solved including all orders of external coupling [83, 84].

4.1.1 Objectives

Our objective is to obtain the quantum statistical expectation values of the current I through the local system and of the matrix elements $P^{s_1}_{s_2} := \langle s_1 | \, p \, | s_2 \rangle$ of the reduced density matrix p of the local system.

At a given time t the expectation values of these quantities are defined by:

$$\begin{aligned} p(t) &= Tr_{res}(\rho(t)) \\ P^{s_1}_{s_2}(t) &:= \langle P_{s_2\, s_1} \rangle(t) = Tr(\rho(t) P_{s_2\, s_1}) \\ \langle I \rangle(t) &= Tr(\rho(t) I) \; . \end{aligned} \tag{4.1}$$

Here $\rho(t)$ denotes the total density matrix including the reservoirs and the local system, Tr_{res} denotes the trace over the reservoir, Tr without any subindex denotes the traces over the reservoirs as well as over the local system, and $P_{s_2 s_1} = |s_2\rangle \langle s_1|$ is defined as in Eq. (2.31).

Expressed by its matrix elements the reduced density $p(t)$ at a time t has the following form:

$$p(t) = \sum_{s_1,\, s_2} P^{s_1}_{s_2}(t) P_{s_1\, s_2} = \sum_{s_1,\, s_2} P^{s_1}_{s_2}(t) \, |s_1\rangle \langle s_2| \; .$$

In our notation $|s_i\rangle$ denote the eigenstates of the stationary Schrödinger equation of the local system, so that $|s_i\rangle$ and also the projection operator (in the Schrödinger picture) are time independent. The off-diagonal matrix elements $P^{s_1}_{s_2}(t)$ of the reduced density matrix are therefore time-dependent already in the absence of the external coupling. This is described by the factor $exp(-i(E_{s_1} - E_{s_2})t/\hbar)$, which gives rise to coherent oscillations within the local system.

The definition for the current through the local system was introduced already in subsection 2.4.1 in Eq. (2.41) as $I := -e\frac{dN_R}{dt}$. Since $\frac{dN_R}{dt} = \frac{i}{\hbar}[H, N_R]$ we can rewrite the current

operator in the following form:

$$\begin{aligned} I &:= -e(\frac{d}{dt}N_R) = -e\frac{i}{\hbar}[H, N_R] = \frac{ie}{\hbar}\sum_{k,s,s'}(T^R_{k\sigma ss'}a^\dagger_{Rk\sigma}P_{ss'} - T^{R*}_{k\sigma ss'}P_{s's}a_{Rk\sigma}) \\ &= -e(-\frac{i}{\hbar}H^R_{T,out} + \frac{i}{\hbar}H^R_{T,in}) \ . \end{aligned} \tag{4.2}$$

The current operator can thus be expressed by the tunneling-in $H^R_{T,in}$ and tunneling-out $H^R_{T,out}$ operators arising due to the coupling to the right reservoir. Since we are always interested in the stationary current through the system, we note that due to charge conservation the following relation holds: $-e(\frac{d}{dt}N_R) = e(\frac{d}{dt}N_L)$. Therefore the current can equivalently be defined by $I := -e/2(\frac{d}{dt}N_R - \frac{d}{dt}N_L)$.[85]

According to Eq. (4.1) the transport properties are determined by the total density matrix $\rho(t)$. Its time evolution is governed by the Hamiltonian (2.26) and is given by:

$$\rho(t) = e^{-\frac{i}{\hbar}H(t-t_i)}\rho(t_i)e^{\frac{i}{\hbar}H(t-t_i)} \ . \tag{4.3}$$

Here t_i denotes an initial time. The time dependence in Eq. (4.3) can be summarized in the time-evolution operator $U(t, t_i) = e^{-\frac{i}{\hbar}H(t-t_i)}$ and its hermitian conjugate. It describes the time evolution of a wavefunction from time t_i to t under the Hamiltonian H. The stationary limit is obtained by shifting the initial time t_i to minus infinity.

It is assumed that the coupling to the external reservoirs is adiabatically switched on at time t_i and that the initial density matrix separates in three parts corresponding to the two reservoirs, $\rho_{res} = \rho_L\rho_R$ and the local density matrix, $p(t)$ respectively.

$$\rho(t_i) = p(t_i)\rho_{res} \ . \tag{4.4}$$

As discussed in subsection 2.4.1 each of the large reservoirs is assumed to stay always in thermal equilibrium with a fixed chemical potential, so that the density matrices ρ_L, ρ_R are given by:

$$\rho_r = e^{-\beta(H_r - \mu_r N_r)}/Z_r \ . \tag{4.5}$$

Here $r \in \{L, R\}$ labels the reservoir, $\beta = 1/(k_B T)$ is the inverse temperature, $N_r = \sum_{k\sigma} a^\dagger_{rk\sigma}a_{rk\sigma}$ denotes the number of particles in the reservoir and the applied bias voltage V is modeled by different chemical potentials in the left and right contact, $\mu_L = eV/2 = -\mu_R$. The grand-canonical potentials Z_r are determined by $Tr(\rho_r) = 1$.

In the stationary limit the initial reduced density matrix $p(t_i)$ is of less importance. The statistics of the local region represented by $p(t) = Tr_{res}(\rho(t))$ are in general strongly affected by the external tunnel coupling, in contrast to fixed statistics of the huge reservoirs. Thus in the stationary limit, the reduced density matrix of the local system will be determined by a self-consistent kinetic equation, which is independent of the initial conditions. However, assuming that the initial density matrix is diagonal in spin and particle number,

it never acquires off-diagonal matrix elements, since the Hamiltonian (2.26) is independent of the spin orientation and is conserving the particle number of the whole system. Mathematically this follows from the fact that the reduced propagator Π introduced below always contains the same number of tunneling-in and tunneling-out processes, as we will see later.

In the following two subsections we continue with the calculation of the reduced density matrix. Thereafter we show in subsection 4.1.4, how the stationary current can be obtained by the same type of calculations.

4.1.2 Kinetic equation

We are interested in the dynamics of the local system, in the presence of the external tunnel coupling. Therefore we study the time evolution of the reduced density matrix described by the time dependence of its matrix elements $P_{s_2}^{s_1}(t)$ defined in Eq. (4.2). According to Eq. (4.2) and Eq. (4.4) we set the initial density matrix to $\rho(t_i) = p(t_i)\rho_{res} = \left(\sum_{s_3,s_4} P_{s_4}^{s_3}(t_i) P_{s_3 s_4}\right) \rho_{res}$ and obtain:

$$\begin{aligned} P_{s_2}^{s_1}(t) = Tr(\rho(t) P_{s_2 s_1}) &= Tr(e^{-\frac{i}{\hbar}H(t-t_i)}(\sum_{s_3,s_4} P_{s_4}^{s_3}(t_i) P_{s_3 s_4})\rho_{res} e^{\frac{i}{\hbar}H(t-t_i)} P_{s_2 s_1}) \\ &= \sum_{s_3,s_4} Tr(P_{s_3 s_4}\rho_{res} e^{\frac{i}{\hbar}H(t-t_i)} P_{s_2 s_1} e^{-\frac{i}{\hbar}H(t-t_i)}) P_{s_4}^{s_3}(t_i) \\ &= \sum_{s_3,s_4} \Pi(t,t_i)_{s_2,s_4}^{s_1,s_3} P_{s_4}^{s_3}(t_i) \quad . \end{aligned} \tag{4.6}$$

In the second line we used the invariance of the trace under permutation. With the above equation we derived a mathematical expression for the matrix elements $\Pi(t,t_i)_{s_2,s_4}^{s_1,s_3}$ of the propagator $\Pi(t,t_i)$.

$\Pi(t,t_i)$ describes the time evolution of the reduced density matrix from time t_i up to time t.

$$p(t) = \Pi(t,t_i) p(t_i) \; . \tag{4.7}$$

Thus $\Pi(t,t_i)$ acts on the reduced density $p(t_i)$ just as the time-evolution operator $U(t,t_i)$ on a wavefunction. Since the reduced density matrix p is already an operator, $\Pi(t,t_i)$ is called a superoperator. If $\Pi(t,t_i)$ is represented in a basis of wavefunctions it becomes a 4-th order tensor, in contrast to $U(t,t_i)$, which is represented by a 2nd-order tensor.[86, 87]

A systematic expansion of the matrix elements of the propagator $\Pi(t,t_i)$ in the external coupling is possible by switching to the interaction picture:

$$\Pi(t,t_i)_{s_2\, s_4}^{s_1\, s_3}(t,t_i) = \mathrm{Tr}\left(P_{s_3 s_4}^I(t_i)\rho_{res}\tilde{T} e^{\frac{i}{\hbar}\int_{t_i}^t dt' H_T^I(t')} P_{s_2 s_1}^I(t) T e^{-\frac{i}{\hbar}\int_{t_i}^t dt'' H_T^I(t'')}\right) . \tag{4.8}$$

Here we introduced the time ordering operator T (operator with later time goes left) and the reversed time ordering operator $\tilde{T}$ (operator with later time goes right).[88] Both T

and $\tilde{T}$ order the following operators without sign change. The label I is used for operators in the interaction representation where the time evolution determined by the unperturbed Hamiltonian H_0 is carried by the operators:

$$A^I(t) = e^{\frac{i}{\hbar}H_0 t} A e^{-\frac{i}{\hbar}H_0 t} \; . \tag{4.9}$$

The nontrivial part of the time evolution forward in time i.e. $U^I(t,t_i)$ is now given by $U^I(t,t_i) = Te^{-\frac{i}{\hbar}\int_{t_i}^{t} dt'' H_T^I(t'')}$ and respectively for the backward propagator $U^I(t_i,t) = (U^I(t,t_i))^\dagger = \tilde{T}e^{\frac{i}{\hbar}\int_{t_i}^{t} dt' H_T^I(t')}$.[88]

Expanding the exponentials of the time-evolution operators in Eq. (4.8), a systematic perturbative calculation of the propagator $\Pi(t,t_i)$ in the external coupling is possible. We call the order of the expansion of the forward and backward propagator f and b and denote the time-variables by $t_1,...,t_f$ and $\tilde{t}_1,...,\tilde{t}_b$, so that we obtain:

$$\begin{aligned}\Pi(t,t_i)^{s_1,s_3}_{s_2,s_4}(t,t_i) \;=\; & \sum_{b,f=0}^{\infty} (-\frac{i}{\hbar})^f (\frac{i}{\hbar})^b \int_{t_i}^{t} d\tilde{t}_1 \int_{\tilde{t}_1}^{t} d\tilde{t}_2 ... \int_{\tilde{t}_{b-1}}^{t} d\tilde{t}_b \int_{t_i}^{t} dt_1 \int_{t_1}^{t} dt_2 ... \int_{t_{f-1}}^{t} dt_f \\ & Tr(\rho_{res} P^I_{s_3 s_4}(t_i) H_T^I(\tilde{t}_1) H_T^I(\tilde{t}_2) .. H_T^I(\tilde{t}_b) P^I_{s_2 s_1}(t) H_T^I(t_f) .. H_T^I(t_2) H_T^I(t_1)) \; .\end{aligned} \tag{4.10}$$

The actual calculation of these matrix elements will be performed with a diagrammatic technique developed by Schoeller *et al* [26, 75, 76, 77], which will be presented in the next subsection.

Now we illustrate the structure of the propagator $\Pi(t,t_i)$ when it is expanded in the external coupling. The idea is to split the time evolution of the reduced density matrix in sub intervals of free propagation alternating with sub intervals where the time evolution is always affected by the external coupling. Thus the propagator $\Pi(t,t_0)$ is expressed by a sum of sequences consisting of the free local propagator, Π^0, alternating with irreducible blocks Σ, which we identify with the self-energy below. The complement "irreducible" means that if the time evolution from t_1 to t_2 is characterized by $\Sigma(t_2,t_1)$, then it is always affected by the external coupling and contains no subinterval of free time evolution. Dropping time indices leads to the Dyson equation for the propagator:

$$\begin{aligned}\Pi &= \Pi^0 + \Pi^0\Sigma\Pi^0 + \Pi^0\Sigma\Pi^0\Sigma\Pi^0 + ... \\ &= \Pi^0 \sum_{n=0}^{\infty} (\Sigma\Pi^0)^n \\ &= \Pi^0 + \Pi^0\Sigma(\Pi^0 \sum_{n=0}^{\infty} (\Sigma\Pi^0)^n) \\ &= \Pi^0 + \Pi^0\Sigma\Pi \; .\end{aligned} \tag{4.11}$$

Including the time indices in Eq. (4.11) again results in the integral form of the kinetic

equation for the reduced density matrix:

$$\Pi(t,t_0) = \Pi^0(t,t_0) + \int_{t_0}^{t} dt_2 \Pi^0(t,t_2) \int_{t_0}^{t_2} dt_1 \Sigma(t_2,t_1)\Pi(t_1,t_0) \tag{4.12}$$

$$p(t) = \Pi(t,t_0)p(t_0) = \Pi^0(t,t_0)p(t_0) + \int_{t_0}^{t} dt_2 \Pi^0(t,t_2) \int_{t_0}^{t_2} dt_1 \Sigma(t_2,t_1)p(t_1) \tag{4.13}$$

In order to derive the differential form of Eq. (4.13), we express the free propagator $\Pi^0(t,t_1)$ by $\Pi^0(t,t_1) = exp(-i/\hbar L_0(t-t_1))$. [86, 87] Here L_0 is the Liouville operator for the unperturbed local system. It is again a superoperator, and is defined by its action on an operator A, $L_0 A := [H_{local}, A]$. This representation of the free propagator follows from the Baker-Hausdorff relation [88]:

$$\begin{aligned}
\Pi^0(t,t_1)p(t_1) &= e^{-\frac{i}{\hbar}H_{local}(t-t_1)} p(t_1) e^{\frac{i}{\hbar}H_{local}(t-t_1)} \\
&= p(t_1) + \sum_{n=1}^{\infty} \frac{(-\frac{i}{\hbar}(t-t_1))^n}{n!} [H_{local}, [...[H_{local}, p(t_1) \underbrace{]...]]}_{n\ times} = \\
&= \sum_{n=0}^{\infty} \frac{(-\frac{i}{\hbar}(t-t_1)L_0)^n}{n!} p(t_1) = e^{-\frac{i}{\hbar}L_0(t-t_1)} p(t_1) \ .
\end{aligned} \tag{4.14}$$

We now differentiate Eq. (4.13) with respect to time and get the following kinetic equation for the reduced density:

$$\frac{d}{dt}p(t) = -\frac{i}{\hbar}\left[H_{local}, p(t)\right] + \int_{t_0}^{t} dt_1 \, \Sigma(t,t_1)\, p(t_1) \ . \tag{4.15}$$

The first term of Eq. (4.15) represents the time evolution due to the internal dynamics of the local system, while the second term describes the effect of the external coupling.

We close this subsection by considering the stationary case, which is defined by $\frac{d}{dt}p^{st} = 0$. In the stationary case one can set $t_0 \to -\infty$ and $t = 0$, which leads to the stationary kinetic equation:

$$0 = \frac{d}{dt}p^{st} = -\frac{i}{\hbar}\left[H_{local}, p^{st}\right] + \int_{-\infty}^{0} dt_1 \, \Sigma(0,t_1)\, p^{st}(t_1) \ . \tag{4.16}$$

Since in the stationary reduced density is by definition time independent, the time integral in Eq. (4.16) can be comprised in the definition $\Sigma = i\hbar(\int_{-\infty}^{0} dt_1 \Sigma(0,t_1))$. Eq. (4.16) thus becomes:

$$0 = i\hbar\frac{d}{dt}p^{st} = \left[H_{local}, p^{st}\right] + \Sigma\, p^{st} \ . \tag{4.17}$$

Expressed in the eigenbasis of the local system Eq. (4.17) has now the form:

$$\begin{aligned}
0 &= i\hbar\frac{d}{dt}P^{s_1}_{s_2} = \langle s_1| \left[H_{local}, p^{st}\right] |s_2\rangle + \sum_{s_3\, s_4} \Sigma^{s_1\, s_3}_{s_2\, s_4} P^{s_3}_{s_4} \\
&= (E_{s_1} - E_{s_2})P^{s_1}_{s_2} + \sum_{s_3\, s_4} \Sigma^{s_1\, s_3}_{s_2\, s_4} P^{s_3}_{s_4} \quad .
\end{aligned} \tag{4.18}$$

Σ has the meaning of a self-energy. Its imaginary part describes the energy width of transport channels, while its real part adds up to the coherent time evolution and renormalizes the energies [5]. The effect of energy renormalization on the transport characteristics will be discussed in detail in section 4.2. Instead of introducing the quantity Σ it is sometimes preferred to define $W = (\int_{-\infty}^{0} dt_1 \Sigma(0, t_1)) = -i/\hbar\Sigma$. Expressed in an eigenbasis, the elements of the tensor W have the meaning of transition rates. In particular if the external coupling is the lowest energy scale of the system, then the elements of W are just the transition rates $W_{ss'}$ presented in subsections 2.4.1 and 3.4.1.[22, 89]

The following subsection is rather technical and illustrates how the irreducible self-energy Σ can be expanded in powers of the external coupling strength by means of a diagrammatic technique based on Eq. (4.10).

4.1.3 Diagrams

The matrix elements of the propagator $\Pi(t, t_i)$ written in the eigenbasis of the local system have been formally derived in Eq. (4.10).

We proceed with the following steps: First the different time orderings of the forward and backward propagator are unified on the Keldysh contour. Then the traces over the reservoir and the local system are performed. Finally the time is integrated out. During these calculations we introduce a diagrammatic description and identify the relevant diagrams needed to calculate the irreducible self-energy Σ, which according to the kinetic equation (4.17) is sufficient to calculate the reduced density matrix. At the end of this subsection we summarize the different steps and list the diagrammatic rules needed to calculate the self-energy up to a given order in the external coupling.

1) Keldysh time and real time

Eq. (4.10) contains two different time ordering operators. Both orderings can be unified by introducing the "Keldysh" time, t_K, which increases along the Keldysh contour as illustrated in Fig. 4.1. Each tunnel Hamiltonian that arises due to the expansion of the forward (backward) time evolution causes a vertex on the upper (lower) time branch and is symbolized by a dot. We denote the number of vertices on the forward and backward time branch by f and b respectively and the total number of vertices by $n = f + b$. The corresponding mathematical expression of the ordered product of operators depicted in Fig. 4.1 is $H_T^I(\tilde{t}_1)H_T^I(\tilde{t}_2)P^I_{s_2 s_1}(t)H_T^I(t_2)H_T^I(t_1)$.

In the next step we perform the trace in Eq. (4.10) and explain the diagrammatic visualization of the result. We perform a trace over the local system as well as over the reservoirs, $Tr = Tr_{res}Tr_{local}$. They can be performed independently since the free time evolution $H_{res} + H_{local}$ does not couple the local system with the reservoirs.[77] Furthermore due to the quadratic structure of creation and annihilation operators in the Tunnel Hamiltonian (that only contains terms like $a^\dagger_{kr\sigma}c_{l\sigma}$ or $c^\dagger_{l\sigma}a_{kr\sigma}$) no additional minus sign arises during this separation, as long as each subsystem keeps its time ordering. We start by tracing out the reservoir.

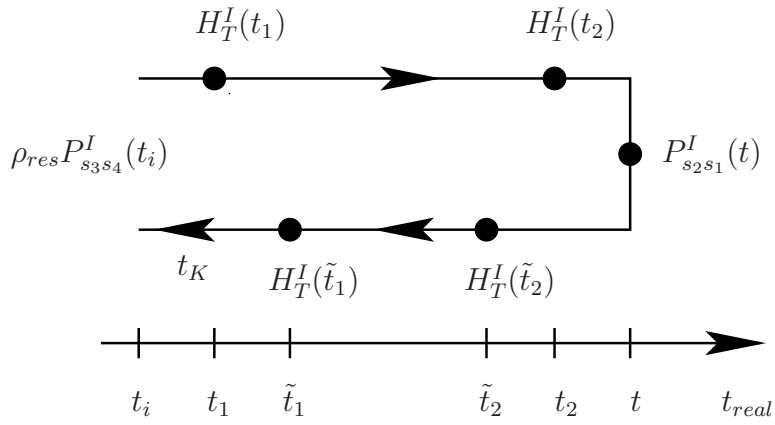

Figure 4.1: The Keldysh contour runs from the initial time t_i along the forward propagator to time t (upper time branch) and then along the backward operator back to t_i (lower time branch). The Keldysh time t_k increases along the Keldysh contour. We define the symbols $>_k$ and $<_k$ for the time order along the Keldysh contour, e.g. with this figure we find: $t_2 <_k \tilde{t}_2$ and $\tilde{t}_1 >_k \tilde{t}_2$. The vertices on the contour represent the mathematical expression: $H_T^I(\tilde{t}_1)H_T^I(\tilde{t}_2)P^I_{s_2s_1}(t)H_T^I(t_2)H_T^I(t_1)$. The real time t_{real} increases from the left to the right.

2) Tracing out the reservoir

Since the reservoirs are noninteracting the trace over the reservoirs can be performed using Wick's theorem.[88] As an illustration of Wick's theorem we look at $\langle a_1^\dagger a_2^\dagger a_3 a_4\rangle$:

$$\begin{aligned}\langle a_1^\dagger a_2^\dagger a_3 a_4\rangle &:= Tr_{res}(\rho_{res} a_1^\dagger a_2^\dagger a_3 a_4) = \\ &= -\langle a_1^\dagger a_3\rangle\langle a_2^\dagger a_4\rangle + \langle a_1^\dagger a_4\rangle\langle a_2^\dagger a_3\rangle \ . \end{aligned} \tag{4.19}$$

Due to the Fermi statistics each interchange of two operators results in a minus sign.

Applying Wick's Theorem to the trace over the reservoirs, each creation operator $(a^\dagger_{kr\sigma})^I(t_1)$ appearing in a tunneling-out Hamiltonian is contracted with the respective annihilation operator $a^I_{kr\sigma}(t_2)$ of a tunneling-in Hamiltonian. The contraction is only non-zero if the reservoir operators coincide in all quantum numbers r, k, σ. Including the relevant tunnel-matrix elements (e.g. $T^r_{k\sigma s_1 s_1'}$ and $T^{r*}_{k\sigma s_2' s_2}$ for the creation and annihilation operator respectively) the contraction results in the factor:

$$\gamma^r_{s_1 s_1' s_2 s_2'}(t_1, t_2) := \sum_{k\sigma} T^r_{k\sigma s_1 s_1'} T^{r*}_{k\sigma s_2' s_2} \langle T_K((a^\dagger)^I_{kr\sigma}(t_1) a^I_{kr\sigma}(t_2))\rangle \ . \tag{4.20}$$

The order of the subscripts $\gamma^r_{s_1 s_1' s_2 s_2'}(t_1, t_2)$ is useful later. We distinguish the two possible time orderings:

$$\langle T_K((a^\dagger)^I_{kr\sigma}(t_1) a^I_{kr\sigma}(t_2))\rangle_{\rho_r} = \begin{cases} e^{\frac{i}{\hbar}\varepsilon_{kr}(t_1-t_2)} f_r(\varepsilon_{kr}) & \text{for} \quad t_1 >_k t_2 \\ e^{\frac{i}{\hbar}\varepsilon_{kr}(t_1-t_2)}(1-f_r(\varepsilon_{kr})) & \text{for} \quad t_1 <_k t_2 \end{cases} \ . \tag{4.21}$$

The symbols $>_k$ and $<_k$ compare times on the Keldysh contour as discussed in the caption of Fig. 4.1. For the following we introduce the notations $f_r^+(\varepsilon) = f_r(\varepsilon)$ and $f_r^-(\varepsilon) =$

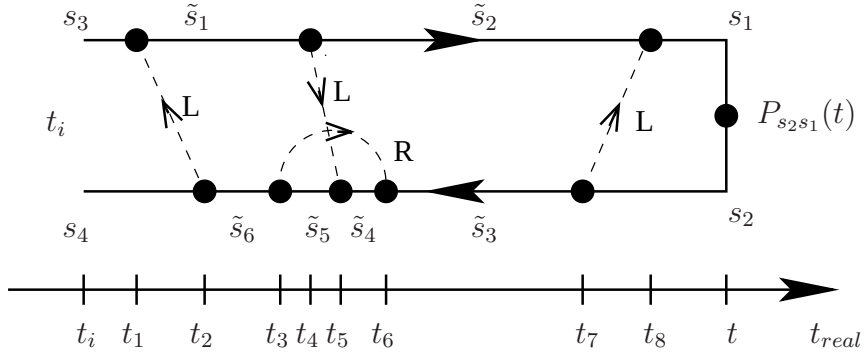

Figure 4.2: Example of a diagram contributing to the propagator element $\Pi(t,t_i)^{s_1\,s_3}_{s_2\,s_4}$. Each tunnel Hamiltonian is represented by a vertex, and the vertices are numerated with increasing numbers for increasing real times (regardless on which time branch). Vertices are connected by directed tunneling lines. Each segment of the Keldysh contour is labeled by an eigenstate of the local system. Time intervals where always at least one tunneling line is present (e.g. $[t_1,t_2]$ or $[t_3,t_6]$) represent irreducible self-energy blocks Σ, while time intervals without tunneling line (e.g. $[t_2,t_3]$ or $[t_6,t_7]$) represent the free propagation Π^0.

$1-f_r(\varepsilon)$. We denote the case of $t_1 >_k t_2$ ($t_1 <_k t_2$) by $\gamma^{r\pm}_{s_1 s_1' s_2 s_2'}(t_1,t_2)$. Together with Eq. (2.34) this results in:

$$\gamma^{r\pm}_{s_1 s_1' s_2 s_2'}(t_1,t_2) \;=\; \frac{1}{2\pi}\int d\varepsilon \Gamma^r_{s_1 s_1' s_2 s_2'}(\varepsilon) f_r^{\pm}(\varepsilon) e^{\frac{i}{\hbar}\varepsilon(t_1-t_2)}\,. \tag{4.22}$$

We visualize the contraction in the diagrams by a dashed tunneling line symbolizing the tunneling electron as shown in Fig. 4.2. The tunneling line starts at a tunneling-out vertex and enters again at the corresponding tunneling-in vertex. Furthermore we label the tunneling line with a reservoir label $r \in \{L,R\}$. According to the diagrammatic rules listed below we finally sum over all possible reservoir labels. To illustrate these rules we note that the factor corresponding to the first (left most) tunneling line in Fig. 4.2 is given by $\gamma^{L+}_{s_4 \tilde{s}_6 \tilde{s}_1 s_3}(t_2,t_1)$ while the tunneling line running from t_4 to t_5 results in the factor $\gamma^{L-}_{\tilde{s}_2 \tilde{s}_1 \tilde{s}_5 \tilde{s}_4}(t_4,t_5)$.

Having introduced the tunneling lines in Fig. 4.2 we note that there are time intervals of the propagator, where a vertical line through the diagram always cuts at least one tunneling line. In these time intervals the propagation of the density matrix is always affected by the external coupling. The corresponding blocks of the propagator therefore contribute to the irreducible self-energy Σ as introduced in Eq. (4.11). We distinguish the different self-energy blocks in Fig. 4.2 according to their number of tunneling lines. For example Fig. 4.2 includes two blocks contributing to the self-energies $\Sigma^{(1)}$ (i.e. expanding up to lowest order in the external coupling), namely in the time-intervals $[t_1,t_2]$ and $[t_7,t_8]$. Additionally there is a contribution to $\Sigma^{(2)}$ in the time-interval $[t_3,t_6]$. According to the kinetic equation (4.18) the self-energy completely determines the reduced density matrix.

3) Tracing out the local system

Now we perform the trace over the local system. According to equation (4.10) there are projection operators at the initial and final time t_i and t respectively and furthermore each tunnel Hamiltonian represented by a vertex in Fig. 4.2 contains a projection operator (see Eq. (2.29) and (2.30)) . Thus each time segment of the Keldysh contour is sandwiched between two projection operators. The outgoing state of the projection operator at the beginning t_1 of a time segment has to coincide with the incoming state of the projection operator at the end of the time interval t_2, $t_1 <_k t_2$. Therefore the time segment can be labeled by an eigenstate s (see Fig. 4.2) and it contributes to the trace over the local system by a factor $e^{-\frac{i}{\hbar}E_s(t_2-t_1)}$ due to the free time evolution. If a time segment is limited by two vertices (i.e. two tunnel Hamiltonians) then the corresponding eigenstate is called intermediate. Therefore, the trace over the local system is performed by labeling all time segments of the contour by an eigenstate s yielding to a factor $\exp(-\frac{i}{\hbar}E_s)(t_2 - t_1)$ for a segment limited by the times $t_1 <_K t_2$, followed by a summation over all intermediate states.

4) Time integration

Before we formulate the diagrammatic rules for the calculation of the self-energies $\Sigma^{(n)}$, where n labels the order in the external coupling, we explain how the time integration is performed. While in equation (4.10) only the vertices on the same time branch keep their time ordering, the diagrams fix the time order also with respect to the real time. Thus the time integration is performed by keeping the time ordering of the vertices regardless on which time branch they are, see Fig. 4.2. Mathematically the integration over the time thus results in a product of resolvents:

$$\begin{aligned} & \lim_{\nu\to 0^+} \int_{-\infty}^{0} dt_1 \int_{t_1}^{0} dt_2 ... \int_{t_{n-1}}^{0} dt_n e^{(-ix_1+\nu)t_1} e^{(-ix_2+\nu)t_2} ... e^{(-ix_n+\nu)t_n} \\ = \; & i^n \frac{1}{x_1 + i0^+} \frac{1}{x_1 + x_2 + i0^+} .. \frac{1}{x_1 + x_2 + ... + x_n + i0^+} . \end{aligned} \tag{4.23}$$

Here the factor $exp(\nu(t_1 + t_2 + ... + t_n))$ arises since the external coupling is adiabatically switched on. While it is useful to fix the order of the vertices with respect to the real time for the calculation of the diagrams, it leads to an exponential increase of the number of topologically different diagrams that have to be calculated, since there are already 2^n possibilities to distribute the n vertices over the two time contours. Furthermore all possibilities of connecting the vertices with directed tunneling lines (including the direction of the line) have to be considered, which leave the diagram irreducible.

There are 8 topologically different diagrams contributing to the sequential tunneling regime i.e. to $\Sigma^{(1)}$, but already 128 diagrams are needed to calculate the self-energy $\Sigma^{(2)}$ in the Co-tunneling regime.

Diagrammatic rules

We now summarize the diagrammatic rules for the calculation of the n-th order contribution to the irreducible self-energy: $\Sigma^{(n)} = i\hbar \int_{-\infty}^{0} dt_1 \Sigma^{(n)}(0, t_1)$.[22, 26, 75, 76, 77]

The self-energy $\Sigma^{(n)}$ is given by the sum of all topologically different irreducible diagrams with $2n$ vertices on the contour. (The topology of a diagram was explained below Eq. (4.23)). The value of each diagram is obtained according to the following rules:

1. Assign to each segment of the Keldysh contour an eigenstate s, and to each tunneling line the reservoir index r and energy ω of the tunneling electron.

2. The times of the vertices cut the diagrams in $2n-1$ succeeding time intervals. Write to each time interval $j = 1, ..2n-1$ the resolvent $1/[\Delta E_j + i0^+]$, where ΔE_j is the difference of 'left going' minus 'right going' energies (consisting of the energies of the eigenstates labeling the contour segments and of the energy of the tunneling lines).

3. Each occurring reservoir line running from a vertex at time t_1 to a vertex at time t_2 gives rise to the factor $1/(2\pi)\Gamma^r_{s_1 s_1' s_2 s_2'}(\varepsilon) f_r^{\pm}(\varepsilon)$. r is the index of the reservoir, $f_r^+(\varepsilon) = \frac{1}{1+exp((\varepsilon-\mu_r)/kT)}$ corresponds to $t_1 >_K t_2$ and $f_r^-(\varepsilon) = 1 - f_r^+(\varepsilon)$ to $t_1 <_K t_2$. $s_{1,2}$ ($s'_{1,2}$) are the outgoing (incoming) dot states at each vertex.

4. The diagram obtains a factor of $(-1)^{b+c}$ where b is the number of vertices on the lower time branch, and c the number of crossings of the tunneling lines. This factor arises due to the different prefactors of the forward and backward time-evolution operator in Eq. (4.10) and due to Wick's theorem applied to the reservoir operators in Eq. (4.19).

5. Sum over all reservoir indices and intermediate local states and integrate over all energies of the tunneling electrons.

4.1.4 Electric current

The current operator is expressed in Eq. (4.2) by the tunneling-in $H^R_{T,in}$ and tunneling-out $H^R_{T,out}$ operators arising due to the coupling to the right reservoir.
Most of the work for the calculation of the expectation value of the current $\langle I\rangle(t) = Tr(\rho(t)I)$ was already done in deriving the irreducible self-energies Σ needed for the kinetic equation. This becomes clear by rewriting the expectation value of the current in analogy to Eq. (4.8):

$$\begin{aligned} -1/e\langle I\rangle(t) &= Tr(\rho(t)(-\frac{i}{\hbar}H^R_{T,out} + \frac{i}{\hbar}H^R_{T,in})) \\ &= Tr(\rho(t_i)\tilde{T}e^{\frac{i}{\hbar}\int_{t_i}^{t} dt' H^I_T(t')}(-\frac{i}{\hbar}(H^R_{T,out})^I(t) + \frac{i}{\hbar}(H^R_{T,in})^I(t))Te^{-\frac{i}{\hbar}\int_{t_i}^{t} dt'' H^I_T(t'')}) \end{aligned}$$

The superscript "I" again denotes the interaction representation. We note that $-\frac{i}{\hbar}(H^R_{T,out})^I(t)$ is presented in a diagram as a tunneling-vertex at time t on the upper contour with an outgoing tunneling line corresponding to the right reservoir. Respectively, $\frac{i}{\hbar}(H^R_{T,in})^I(t)$ can be represented by vertex at time t on the lower branch of the Keldysh contour with an incoming tunneling line corresponding to the right reservoir.

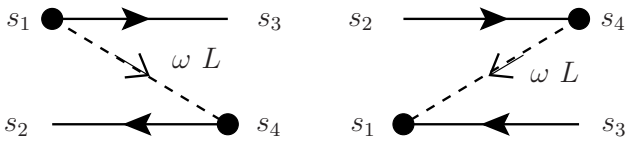

Figure 4.3: Illustration of the mirror rule for a diagram of first order in the external coupling. The right diagram is obtained by reflecting the left diagram horizontally and by changing the directions of the tunneling lines. Its value is given by the complex conjugate of left one multiplied by -1.

This correspondence leads to the following expression for the stationary current:

$$\begin{aligned} I &= -e\,Tr_{local}\left(\left(\int_{-\infty}^{0} dt'\Sigma^I(0,t')\right)p^{st}\right) \\ &= \frac{ie}{\hbar}\,Tr_{local}\left(\Sigma^I p^{st}\right) . \end{aligned} \tag{4.24}$$

Here p^{st} is the stationary reduced density matrix (determined by the kinetic equation (4.18) and the normalization condition $\sum_s P_s^s = 1$) and $\Sigma^I = \int_{-\infty}^{0} dt'\Sigma^I(0,t')$ denotes the irreducible self-energy for the current. Σ^I is given by a lower sum of the diagrams contributing to Σ. The relevant diagrams are the ones, where the tunneling line of the right most vertex (at $t = 0$) corresponds to the right reservoir and is an outgoing (incoming) line if the vertex is on the upper (lower) time branch.
Written in the eigenbasis of the local system, equation (4.24) turns into:

$$I = \frac{ie}{\hbar}\sum_{s,s_1,s_2}(\Sigma^I)^{ss_1}_{ss_2}\,p^{s_1}_{s_2} . \tag{4.25}$$

In the following subsection we show some properties of the diagrams, which reduce the number of diagrams that need to be calculated and that assure e.g. the hermiticity of the density matrix and the probability conservation.

4.1.5 Conservation Laws

We present two important symmetries of the irreducible self-energies Σ and Σ^I, namely the mirror rule and the sum rule. Both rules hold for each order in the external coupling separately. The mirror rule states that:

$$\Sigma^{s_2 s_1}_{s_2' s_1'} = -\left(\Sigma^{s_2' s_1'}_{s_2 s_1}\right)^* \;;\; (\Sigma^I)^{s_2 s_1}_{s_2' s_1'} = -\left((\Sigma^I)^{s_2' s_1'}_{s_2 s_1}\right)^* .$$

This relation can be proven by identifying to each diagram its mirror diagram as illustrated in Fig. 4.3. The mirror diagram is obtained by reflecting the original diagram horizontally and by changing the directions of all tunneling lines. Looking at the diagrammatic rules

in energy space we find that the expressions for the mirror diagram only differs in the resolvents. According to rule 2 the resolvents $1/[\Delta E_j + i0^+]$ of the original diagram turn to $1/[-\Delta E_j + i0^+] = -(1/[\Delta E_j + i0^+])^*$ in the mirror diagram. By construction the number of resolvents is always odd, so that the mirror diagram is given by the complex value of the original diagram multiplied by -1. The mirror rule reduces the number of diagrams that have to be calculated by a factor of two. Furthermore it assures the hermiticity of the reduced density matrix and guarantees a real current.

The sum rule states that:

$$\sum_s \Sigma^{ss_1}_{ss'_1} = 0 \; ; \;\; \sum_s (\Sigma^I)^{ss_1}_{ss'_1} = 0 \; .$$

It relies on the fact that the sum over the diagrams with the latest vertex at $t = 0$ on the upper time branch just cancel the sum of all diagrams with the latest vertex on the lower time branch, due to rule 4 on page 85 . The sum rule guarantees the probability conservation since $\frac{d}{dt}\sum_s P_{ss} = \sum_{s,s_1,s'_1} \Sigma^{ss_1}_{ss'_1} P_{s_1,s'_1} = 0$. Furthermore it guarantees that the equations that determine the occupation probabilities of the eigenstates of the local system are linearly dependent. Therefore there must exist a nontrivial solution for the reduced density matrix as demanded.

4.1.6 Coherent tunneling processes and off-diagonal density matrices

In the first part of this subsection we motivate why a large ratio kT/Γ , with $\Gamma = \Gamma^L + \Gamma^R$ denoting the external coupling strength, suppresses coherent tunneling events and thus justifies the sequential tunnel approximation, which is valid to first order in the coupling Γ and assumes independent tunneling events. In a higher-order tunneling process at least two tunneling events are present at the same time, so that they are no longer independent of each other. In the diagrammatic language this corresponds to self-energy diagrams where at least two tunneling lines partially overlap. In order to identify the parameter regime, in which diagrams with partially overlapping tunneling lines can be neglected we need to compare the coherence time of tunneling with the average time between two tunneling events. The latter is estimated by $\hbar/\Gamma$.

The coherence time is given by the average time-duration of a tunneling process. It is visualized in the diagrams by the finite (time-)extend of the tunneling lines. According to Eq. (4.22) a tunneling line running from time t to time $t + \Delta t$ gives rise to a factor $\gamma^{r\pm}_{s_1 s'_1 s_2 s'_2}(t, t + \Delta t)$. Assuming a constant density of states the coupling strength, Γ^r and also the spectral function $\Gamma^r_{s_1 s'_1 s_2 s'_2}$ (see Eq. (2.34), (2.36)) are independent of energy and one obtains [86, 90]:

$$\begin{aligned} \gamma^{r\pm}_{s_1 s'_1 s_2 s'_2}(t, t + \Delta t) &= \frac{1}{2\pi} \int d\varepsilon \Gamma^r_{s_1 s'_1 s_2 s'_2}(\varepsilon) f^{\pm}_r(\varepsilon) e^{-\frac{i}{\hbar}\varepsilon(\Delta t)} \\ &= \frac{i\Gamma^r_{s_1 s'_1 s_2 s'_2} e^{\mp \frac{i}{\hbar}\mu_r(\Delta t)}}{2\beta sinh[\pi(\Delta t + i0^+)/(\beta\hbar)]} \; . \end{aligned} \tag{4.26}$$

Here $\beta = 1/(k_B T)$ denotes the inverse temperature. For a time duration $\Delta t \gg \pi/(\beta\hbar)$ this expression is exponentially damped with the characteristic time $\hbar\beta$. Thus the appearance of higher order tunneling events will be strongly suppressed for $\Gamma \ll kT$.

These qualitative arguments are exclusively based on the coherence time of tunneling, while the influence of the eigenspectrum of the local system on the self-energies (transition rates) has not been considered. An inclusion of these effects may lead to a strong suppression of the sequential tunneling rates, even below the higher order rates. As discussed in subsections 2.4.1, 3.4.1 the sequential tunneling rates are e.g. exponentially suppressed within the Coulomb blockade regime. Furthermore for particular parameters sequential tunneling is spin or pseudo-spin blocked. Since higher order tunneling events are less affected by the Coulomb blockade or the selection rules, they may be relevant in these cases. However, anyway, the fingerprints of higher order tunneling events will be strongly suppressed for $\Gamma \ll kT$.

In the second part of this subsection we discuss the meaning of off-diagonal entries $P^{s_1}_{s_2}$ of the reduced density matrix[1]. While a diagonal density matrix represents an incoherent mixture of eigenstates, an off-diagonal density matrix is at least partially coherent, since its off-diagonal elements represent coherent superpositions of the eigenstates and coherently oscillate in time due to the local dynamics. One should be careful not to mix the two different meanings of the word "coherent" either used in the context of coherent reduced density matrices or in the context of coherent tunneling. Coherent tunneling processes imply that tunneling events are no longer independent of each other, but in general they do not imply that the reduced density matrix acquires off-diagonal elements. Complementary off-diagonal (thus coherent) density matrices can also arise in sequential transport (thus for incoherent tunneling processes). A prominent example for the latter case is sequential transport through a double dot in a parameter regime, when the external coupling exceeds the interdot tunneling. This system will be discussed in detail in section 4.2.

Now we clarify under which conditions off-diagonal entries of the reduced density matrix are absent or can be neglected. One reason for a diagonal reduced density matrix are symmetries of the Hamiltonian. For example if the Hamiltonian is independent of the spin orientation and conserves the particle number of the whole system, then the stationary reduced density matrix will be diagonal in spin and particle number of the local system. Another reason for the absence of an off-diagonal matrix element becomes evident by looking at its kinetic equation:

$$0 \;=\; i\hbar\frac{d}{dt}P^{s_1}_{s_2} = (E_{s_1} - E_{s_2})P^{s_1}_{s_2} + \sum_{s_3\, s_4} \Sigma^{s_1\, s_3}_{s_2\, s_4} P^{s_3}_{s_4} \quad . \tag{4.27}$$

If the energy difference $(E_{s_1} - E_{s_2})$ is much larger than the tunnel coupling Γ then the second term of the above equation can be neglected in comparison with the first one and the off-diagonal matrix element disappears. This effect can also be understood by noting that

[1] Here, we always assume that the basis of the reduced density matrix is given by the eigenbasis of the local system

the coupling strength characterizes the intrinsic broadening of levels due to the external coupling. A superposition of different levels only occurs if the broadening Γ exceeds the level spacing $(E_{s_1} - E_{s_2})$ while is can be neglected for $\Gamma \ll E_{s_1} - E_{s_2}$.

Thus, by applying the master-equation approach in subsections 2.4.1, 3.4.1 we not only assumed sequential tunneling (justified e.g. by $\Gamma \ll kT$), but we also assumed the external coupling to be much smaller than all relevant excitation energies, so that off-diagonal density matrix elements could be neglected. In the following section we drop the second assumption and study features of sequential transport through a serial double dot in a parameter regime, where the reduced density matrix acquires off-diagonal entries.

4.2 Probing level renormalization by sequential transport through double quantum dots

In this section we study electron transport through double quantum dots in series. In contrast to the master equation approach applied in subsection 3.4.1 we now focus on the case, when the interdot coupling and the level asymmetry between the dots are of the same order of magnitude as or smaller than the external coupling strength. In this regime it is no longer possible to describe the double dot as a single object, being in a mixture of its eigenstates. Now superpositions of eigenstates play a relevant role and it is essential to take the off-diagonal elements of the reduced density matrix into account (see discussion in subsection 4.1.6).

The interplay of the coherent dynamics on the double dot on the one hand and the coupling to external reservoirs on the other hand leads to energy shifts of the dot levels. This energy renormalization of the dot levels already arises at relatively high temperature, where transport is described by incoherent sequential tunneling processes. The presented results contrast the standard description of sequential tunneling by a master equation approach as introduced in subsection 2.4.1 and 3.4.1, where the local system remains unchanged by the external coupling. Interestingly the current through a double dot coupled in series is highly sensitive to the induced asymmetry between the dots and signatures of the level renormalization are visible in either the current-voltage characteristics or in the stability diagram.

4.2.1 Introduction

In chapter 3 we studied many-particle effects and in particular the molecular binding in vertical double dots. In this section we focus on lateral double dots defined by top gates as shown in Fig. 4.4 a), since they allow to scan a rich parameter space in a single sample by only changing external voltages. Now the coupling of the dots to the external leads as well as the interdot coupling can be adjusted by external voltages, while in vertical structures these quantities are defined by the growth process. Furthermore one can detune the levels in the right and left dot independent of the transport voltage due to a more

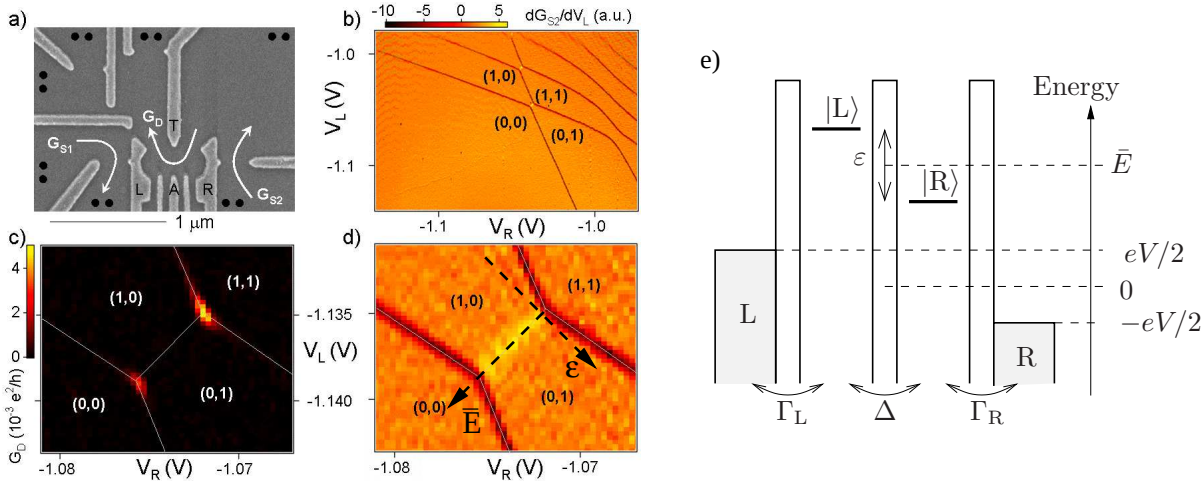

Figure 4.4: a)-d) Experimental data taken from reference[91], e) Theoretical model. a) Image of a lateral double dot device. Electron numbers on the dots and interdot coupling are tunable by gates L,R and T. Current through the double dot can be measured directly i.e. via conductance G_D or via the quantum point conductances G_{S1} or G_{S2} serving as charge sensors. b) and d) Differential conductances dG_{S2}/dV_L as function of gate voltages V_R, V_L in linear transport regime. Charge states are labeled by (M,N) corresponding to the number of electrons in the left (M) and right (N) dot. c) G_D as function of gate voltages V_R, V_L. e) Schematic energy profile for a double dot coupled in series to two reservoirs. Each reservoir is coupled to the dot of the corresponding side by the coupling strength Γ^r, $r \in \{\mathrm{L}, \mathrm{R}\}$. The interdot coupling is determined by Δ. The energies of the dot levels are characterized by the mean energy $\bar{E}$ and their relative distance ε, indicated by dashed lines in d).

complex gate structure. Finally the measurement of the current through the double dot is often complemented by charge sensing each dot by quantum point contacts as indicated in Fig. 4.4 a). Recent experiments on lateral double dots include the measurements of quantum mechanical level repulsion due to interdot coupling [69] as well as due to external magnetic fields,[92] the detection of molecular states in a double dot dimer,[93] and the observation of coherent time evolution of the dot states.[94] Another reason for the intense study of lateral multi-dot structures is their possible use for quantum information. Recent theoretical proposals on quantum computing based on dot structures can be found e.g. in references [95, 96, 97, 98], and corresponding experimental achievements towards a charge and/or spin qubit realized in double dots are reported in references [91, 94, 99, 100].

Transport through serial double dots, as depicted in Fig. 4.4 e), inherently visualizes the basic quantum mechanical concept of coherent superposition of charge states.[101] The states that are coupled to the left and right lead, the localized states in the left and right dot, respectively, are not energy eigenstates of the double dot. This leads to oscillations of the electron in the double dot as it was shown in recent experiments.[94, 99] To account for this internal dynamics, descriptions using classical rates only, are insufficient. For this

reason approaches including non-diagonal density matrix elements for the double dot have been developed.[102, 103, 104, 105, 106, 107].

In this section, we propose to use a serial double quantum dot to probe another consequence of quantum mechanics: the energy level renormalization of the quantum dot levels due to tunnel coupling to a reservoir. This idea is based on two properties of a serial double dot system. First, the left and right dot levels are tunnel-coupled to different reservoirs. The energy shift of the left and right dot levels is, in general, different, since the level renormalization is a function of level energy, lead chemical potential, and external tunnel coupling. Second, the conductance through the double dot is very sensitive to the difference of the energy levels and shows a resonant behavior with the width given by the tunnel couplings.[108] This width can be much smaller than temperature. This sharpness of the resonance makes the conductance a valuable experimental tool, for example to measure the shell structure of quantum dots.[109]

It is well known[76, 110, 111] that tunnel coupling to reservoirs renormalizes the energy levels. In single-dot geometries such an energy renormalization is only accessible in transport of higher order in the tunnel coupling strength. We show, that this is different for the serial double dot geometry, for which renormalization effects are visible in the conductance also for weak dot-lead coupling (in comparison with temperature). This regime is still well described by transport to first order (sequential tunneling) in the tunnel-coupling strength $\Gamma = \Gamma^{\mathrm{L}} + \Gamma^{\mathrm{R}}$.

The section is organized as follows: In subsection 4.2.2 we present the model Hamiltonian for the double dot. Then we derive the stationary density matrix and the $dc-$current for arbitrary bias voltages in subsection 4.2.3, based on the transport theory introduced in the previous chapter. Furthermore we give an illustrative reformulation of the master equation in terms of a pseudospin. In subsection 4.2.5 we point out the similarity of the present system and a quantum dot coupled to ferromagnetic leads with antiparallel magnetization.

4.2.2 Model

We consider a double quantum dot, contacted in series, which is described by the Hamiltonian: [102, 103]

$$H = \sum_{r=\mathrm{L,R}} H_r + H_{\mathrm{D}} + H_{\mathrm{T}} \,. \tag{4.28}$$

Here $r \in \{\mathrm{L}, \mathrm{R}\}$ labels the contacts, $H_{\mathrm{L/R}}$ describe the electric contacts on the left (L) and right (R) side, H_{D} describes the double dot and H_{T} the serial coupling of the double dot to the external contacts.

As discussed in subsection 2.4.1 we model the external contacts by large reservoirs of noninteracting electrons $H_r = \sum_{k,\sigma} \varepsilon_{rk} a^\dagger_{rk\sigma} a_{rk\sigma}$ where $a_{rk\sigma}, a^\dagger_{rk\sigma}$ denote the annihilation and creation operators for electrons in the reservoir $r \in \{\mathrm{L}, \mathrm{R}\}$ with spin σ. Furthermore it is assumed that the reservoirs are in equilibrium, so that they are characterized by

the Fermi distribution $f_{\mathrm{L/R}}(\omega) = f(\omega - \mu_{\mathrm{L/R}})$, where $\mu_{\mathrm{L/R}} = \pm eV/2$ denote the chemical potential in the reservoirs and with $f(x) = 1/(exp(\beta x) + 1))$, $\beta = 1/(k_B T)$.

We restrict the eigenspectrum of each dot to a single spin-degenerate level, so that the Hamiltonian H_{D} for the double dot is given by:

$$H_{\mathrm{D}} = \sum_{r=\mathrm{L,R}} E_r n_r - \frac{\Delta}{2} \sum_{\sigma} \left(c^{\dagger}_{\mathrm{L}\sigma} c_{\mathrm{R}\sigma} + c^{\dagger}_{\mathrm{R}\sigma} c_{\mathrm{L}\sigma} \right) + U n_{\mathrm{L}} n_{\mathrm{R}} + U'(n_{\mathrm{L}\uparrow} n_{\mathrm{L}\downarrow} + n_{\mathrm{R}\uparrow} n_{\mathrm{R}\downarrow}) \,. \quad (4.29)$$

Here $c_{i\sigma}, c^{\dagger}_{i\sigma}$ are again the annihilation and creation operators of an electron on dot i with spin σ, and $n_{i\sigma} = c^{\dagger}_{i\sigma} c_{i\sigma}$, $n_i = \sum_{\sigma} c^{\dagger}_{i\sigma} c_{i\sigma}$ are the occupation number operators for dot $i \in \{\mathrm{L}, \mathrm{R}\}$. The other parameters are the energies $E_{\mathrm{L,R}}$ of the electronic level in the left and right dot, the interdot tunnel energy Δ and the intra- and interdot Coulomb energies called U' and U respectively.

The first term of H_{D} describes the energy needed to occupy the electronic levels of the left and right dot characterized by the energies $E_{\mathrm{L/R}}$. We parameterize the levels by their average energy $\bar{E} = (E_{\mathrm{L}} + E_{\mathrm{R}})/2$ and their difference $\varepsilon = E_{\mathrm{L}} - E_{\mathrm{R}}$, so that $E_{\mathrm{L/R}} = \bar{E} \pm \varepsilon/2$. The second term describes the interdot tunneling by the real and positive parameter Δ. The energy profile of the electronic levels is illustrated in Fig. 4.4 e). The single-particle eigenstates of the double dot subsystem are the bonding and anti-bonding states with energies $E_{\mathrm{b/a}} = \bar{E} \mp \Delta_{\mathrm{ab}}/2$ where $\Delta_{\mathrm{ab}} = \sqrt{\Delta^2 + \varepsilon^2}$ denotes their energy splitting. This identifies Δ as minimum distance between the bonding and anti-bonding eigenstates as function of the left and right energy level.[69] The last two terms of H_{D} describe the Coulomb interaction on the double dot. Electrons on different dots interact via the interdot Coulomb interaction U while a double occupation of one individual dot is associated with the intradot charging energy U'. We assume $U' \gg U$ (in particular $U' - U \gg \Delta$), so that the two-particle ground state has the form $|\mathrm{L}\sigma\mathrm{R}\sigma'\rangle$ and its energy is independent of spin.[107] We assume that the intradot charging energy always exceeds the lead Fermi energies. Therefore the states with three or more electrons in the double dot or with two electrons in the same dot will have a vanishing occupation probability. However, we allow the states $|\mathrm{L}\sigma\mathrm{L}\bar{\sigma}\rangle$ and $|\mathrm{R}\sigma\mathrm{R}\bar{\sigma}\rangle$ as intermediate (virtual) states in our calculation, since they provide a natural high-energy cut-off, as discussed below.

It turns out that our calculations trivially include the case of spin-polarized electrons. In this case the spin quantum number is fixed and a double occupation of a dot level is forbidden by the Pauli principle. By introducing the spin-degeneracy $g_\sigma \in \{1, 2\}$, we are able to present the case of spin-polarized electrons ($g_\sigma = 1$) as well as the spin-degenerate ($g_\sigma = 2$) one. We mainly focus on the case $g_\sigma = 2$ which results in the Hamiltonian H_{D} given above.

The third part of the total Hamiltonian (4.28) describes the coupling between the double dot and the external leads and is given by:

$$H_{\mathrm{T}} = \sum_{k\sigma} t_{\mathrm{L}k} a^{\dagger}_{\mathrm{L}k\sigma} c_{\mathrm{L}\sigma} + t_{\mathrm{R}k} a^{\dagger}_{\mathrm{R}k\sigma} c_{\mathrm{R}\sigma} + \mathrm{h.c.} \quad (4.30)$$

Due to the serial geometry, an electron from the right (left) reservoir can only tunnel to the right (left) dot. The tunnel coupling of reservoir r to the corresponding dot is characterized by the coupling strength $\Gamma^r(\omega) = 2\pi \sum_k |t_{rk}|^2 \delta(\varepsilon_{rk} - \omega)$ (see Eq. (2.33)). We consider only spin conserving tunneling processes, and assume a constant density of states in the reservoirs, which yields energy independent couplings $\Gamma^r(\omega) = \Gamma^r$.

4.2.3 Kinetic equation

Following the transport theory introduced in the previous section, the reduced density matrix p of the double dot is obtained from the density matrix of the whole system by integrating out the reservoir degrees of freedom. According to Eq. (4.17) the kinetic equation for the reduced density matrix is given by:

$$0 = i\hbar \frac{d}{dt} p \quad = \quad [H_{\mathrm{D}}, p] + \Sigma p \,. \tag{4.31}$$

The first part in Eq. (4.31) represents the coherent internal dynamics on the double dot, which depends on the level separation ε and the interdot coupling Δ. Non-eigenstates of the double dot arising due to the sequential tunneling perform charge oscillations with the characteristic frequency $\Delta_{\mathrm{ab}}/\hbar$.[94, 99]

The second part of Eq. (4.31) accounts for the tunnel coupling between double dot and external reservoirs. The fourth-order tensor Σ contains imaginary and real parts, associated with particle transfer processes and with tunnel induced energy shifts of the dot levels, respectively. The latter has been neglected in previous works.[102, 103, 105, 106, 107] We calculate Σ using the real-time diagrammatic approach introduced in the previous section.[22, 26, 75, 76, 77] The technical details of the calculation of Σ are described in Appendix B. Also alternative methods for the calculation of Σ are available such as Bloch-Redfield theory.[112, 113, 114]

In the following we concentrate on the regime of weak tunnel coupling between double dot and leads. Therefore, we calculate Σ to lowest order in the tunnel-coupling strength $\Gamma = \Gamma^{\mathrm{L}} + \Gamma^{\mathrm{R}}$, which defines the so-called sequential-tunneling approximation. This approximation implies that all tunneling events are independent from each other, which is fulfilled for $k_{\mathrm{B}}T \gg \Gamma$. As discussed in subsection 4.1.6 , the condition $k_{\mathrm{B}}T \gg \Gamma$ guarantees, that the correlations generated in the contacts during a tunnel process decay fast in comparison to the average time between consecutive tunneling events. Therefore higher order, coherent tunneling events are suppressed and may be neglected.

As shown in subsection 4.1.6 off-diagonal density matrix elements disappear for $\Delta_{\mathrm{ab}} \gg \Gamma$, so that for $\Delta_{\mathrm{ab}} \gg \Gamma$ transport through the double-dot system takes place through two separate incoherent levels. In the sequential tunneling regime the kinetic equation (4.31) then reduces to the master equation used in subsection (3.4.1), where the double dot is always described by an incoherent mixture of eigenstates.

Now we are interested in the opposite regime, i.e. in $\Delta_{\mathrm{ab}} \lesssim \Gamma$, where the external coupling strongly modifies the internal dynamics captured in the off-diagonal elements of the reduced

density matrix.[102, 103, 107] The validity condition for sequential tunneling, i.e. $\Gamma \ll k_{\mathrm{B}}T$ then implies $\Delta_{\mathrm{ab}} \ll k_{\mathrm{B}}T$. In section 4.1.6 we showed that the average time duration of a tunneling event is given by $\hbar/kT$. In the regime discussed here, $\hbar/kT$ is much shorter than the period of internal oscillations on the double dot given by $\hbar/\Delta_{\mathrm{ab}}$. Consequently, the localized states $|\mathrm{L}\sigma\rangle$ and $|\mathrm{R}\sigma\rangle$ can be used as eigenstates of the double dot in the calculation of Σ, which facilitates the interpretation of the dynamics.[102, 103, 105, 106, 107] Another consequence of the condition $\Delta_{\mathrm{ab}} \ll k_{\mathrm{B}}T$ is that the Fermi functions of the reservoirs do not resolve energies of the order of the interdot tunneling or the level separation, i.e. for any energy ω it is valid that $f_r(\omega \pm \Delta/2), f_r(\omega \pm \varepsilon/2) \approx f_r(\omega)$ and in particular $f_r(E_{a/b}) \approx f_r(E_{L/R}) \approx f_r(\bar{E})$. The formulas we derive for the current therefore contain the Fermi functions at the average single-particle level $f_r(\bar{E})$.

Since the Hamiltonian (4.28) is independent of the spin orientation, each spin-realization of a charge state is equiprobable. We can therefore define $P_0 = \langle 0|\, p\, |0\rangle$, $P^{\mathrm{r}}_{\mathrm{r}'} = \sum_\sigma \langle \mathrm{r}\sigma|\, p\, |\mathrm{r}'\sigma\rangle$, $P_2 = \sum_{\sigma,\sigma'} \langle \mathrm{L}\sigma\mathrm{R}\sigma'|\, p\, |\mathrm{L}\sigma\mathrm{R}\sigma'\rangle$. Furthermore the stationary density matrix is diagonal in spin and particle number. Thus the reduced density matrix p describing the double dot is given by the 4×4 matrix

$$p = \begin{pmatrix} P_0 & 0 & 0 & 0 \\ 0 & P^{\mathrm{L}}_{\mathrm{L}} & P^{\mathrm{L}}_{\mathrm{R}} & 0 \\ 0 & P^{\mathrm{R}}_{\mathrm{L}} & P^{\mathrm{R}}_{\mathrm{R}} & 0 \\ 0 & 0 & 0 & P_2 \end{pmatrix} . \tag{4.32}$$

The diagonal elements of the density matrix are the probabilities to find the double dot empty (P_0), the left ($P^{\mathrm{L}}_{\mathrm{L}}$) or the right dot ($P^{\mathrm{R}}_{\mathrm{R}}$) singly occupied, or the two dots simultaneously occupied by one electron (P_2). Furthermore superpositions of the two singly occupied states are possible $P^{\mathrm{L}}_{\mathrm{R}} = \left(P^{\mathrm{R}}_{\mathrm{L}}\right)^\star$.

Instead of working with the off-diagonal density matrix (4.32) we prefer to switch to a pseudospin representation. As any two level system, the 2×2 hermitian submatrix of the singly occupied states can be treated as $SU(2)$ representation of a pseudospin Bloch vector $\boldsymbol{I} = (P^{\mathrm{L}}_{\mathrm{R}} + P^{\mathrm{R}}_{\mathrm{L}}, iP^{\mathrm{L}}_{\mathrm{R}} - iP^{\mathrm{R}}_{\mathrm{L}}, P^{\mathrm{L}}_{\mathrm{L}} - P^{\mathrm{R}}_{\mathrm{R}})^T/2$. For a complete set of variables, we further introduce $P_1 = P^{\mathrm{L}}_{\mathrm{L}} + P^{\mathrm{R}}_{\mathrm{R}}$ as the probability of a singly-occupied double dot. Such a pseudospin representation is often used in the quantum information community.[95, 96, 99]

Kinetic equation in pseudospin representation

A simplified visualization of transport through the double dot based on the pseudospin presentation is given in Fig. 4.5. Imagine the double dot is empty and $\mu_L > \mu_R$. Then, in a first step, an electron hops from the left reservoir to the left dot. Afterwards it coherently oscillates around the eigenaxis of the double dot defined by $\vec{B}_{\mathrm{DD}} = (-\Delta, 0, \varepsilon)$, which causes a finite possibility to occupy the right dot. Finally the electron hops from the right dot to the right reservoir. Such a sequence of tunneling events leads to a current through the double dot. While in a master equation approach as studied in subsection 3.4.1, one assumes that electrons directly hop from the reservoirs into the bonding or anti-bonding state, we now take into account the internal dynamics on the double dot, since the coherent

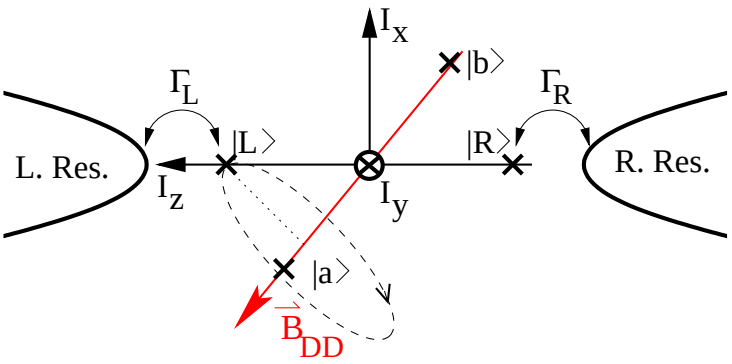

Figure 4.5: Visualization of the single-particle dynamics in a pseudospin representation, if energy renormalization is neglected. (Illustrated is the x-z plane, the y-axis points into the sheet.) Due to the serial geometry the external reservoirs couple to the localized states $|L\rangle = |I_z = 1/2\rangle$, $|R\rangle = |I_z = -1/2\rangle$ situated on the z-axis. Since the localized states are not eigenstates of the double dot, they coherently oscillate around the eigenaxis $\vec{B}_{\rm DD} = (-\Delta, 0, \varepsilon)$, leading to a motion out of the x-z plane. The characteristic frequency of these oscillations is given by $\Delta_{\rm ab}/\hbar$.

oscillations on the double dot happen on the same time scale (or are even slower) than the time between consecutive tunneling events. Keeping this picture in mind we now discuss the kinetic equations for the occupation probabilities and the pseudospin components.

Due to the serial geometry the external tunneling affects only the z-direction of the pseudospin and the left and right contacts couple with a different sign to $I_{\rm z}$. This is captured by the definitions $\hat{\mathbf{n}}_{\rm L} = (0,0,1)$ and $\hat{\mathbf{n}}_{\rm R} = (0,0,-1)$, which can be understood as pseudo-spin magnetizations of the leads. With these definitions the occupation probabilities obey the following master equations:

$$\begin{aligned} 0 = \frac{d}{dt}P_0 &= \sum_r \frac{\Gamma^r}{\hbar}(-g_\sigma f_r(\bar{E})P_0 + \frac{1}{2}f_r^-(\bar{E})P_1) + \\ &\quad + \sum_r \frac{\Gamma^r}{\hbar} f_r^-(\bar{E})\hat{\mathbf{n}}_{\rm r}\cdot\mathbf{I}\,, \qquad (4.33) \\ 0 = \frac{d}{dt}P_2 &= \sum_r \frac{\Gamma^r}{\hbar}(\frac{g_\sigma}{2}f_r(\bar{E}+U)P_1 - f_r^-(\bar{E}+U)P_2) \\ &\quad - \sum_r \frac{\Gamma^r}{\hbar} g_\sigma f_r(\bar{E}+U)\hat{\mathbf{n}}_{\rm r}\cdot\mathbf{I} \qquad (4.34) \\ P_1 &= 1 - P_0 - P_2\,. \qquad (4.35) \end{aligned}$$

In equilibrium ($f_{\rm R} = f_{\rm L}$) the diagonal matrix elements fulfill the Boltzmann statistics $P_0 = 1/Z$, $P_1 = 2g_\sigma \exp[-\bar{E}/k_{\rm B}T]/Z$, $P_2 = g_\sigma^2 \exp[-(\bar{E}+U)/k_{\rm B}T]/Z$, where Z is determined by the normalization condition $1 = P_0 + P_1 + P_2$. Furthermore all components of the pseudospin vanish.

The dynamics of the single-particle state is described by a Bloch-like equation:

$$0 = \frac{d}{dt}\mathbf{I} \;=\; \left(\frac{d\mathbf{I}}{dt}\right)_{\text{acc.}} - \left(\frac{d\mathbf{I}}{dt}\right)_{\text{rel.}} + \frac{1}{\hbar}(\mathbf{B}\times\mathbf{I}) \quad . \tag{4.36}$$

The first term, $\left(\frac{d\mathbf{I}}{dt}\right)_{\text{acc.}}$ describes the accumulation of pseudospin caused by the external coupling. Due to the serial geometry this spin accumulation occurs along the z-direction. It is given by:

$$\left(\frac{d\mathbf{I}}{dt}\right)_{\text{acc.}} \;=\; \sum_r \hat{\mathbf{n}}_{\text{r}}\frac{\Gamma^r}{2\hbar}\left[g_\sigma f_r(\bar{E})P_0 + \frac{1}{2}\left(g_\sigma f_r(\bar{E}+U) - f_r^-(\bar{E})\right)P_1 - f_r^-(\bar{E}+U)P_2\right] .$$

The term $\left(\frac{d\mathbf{I}}{dt}\right)_{\text{rel.}}$ describes the isotropic relaxation of the pseudospin. It is due to transitions from a singly occupied double dot to either an empty or a doubly occupied double dot. These transition destroy all pseudospin components. The term $\left(\frac{d\mathbf{I}}{dt}\right)_{\text{rel.}}$ is given by:

$$\left(\frac{d\mathbf{I}}{dt}\right)_{\text{rel.}} \;=\; \frac{1}{2}\sum_r \frac{\Gamma^r}{\hbar}\left(f_r^-(\bar{E}) + g_\sigma f_r(\bar{E}+U)\right)\mathbf{I} .$$

Finally the third term in Eq. (4.36) describes a rotation of the pseudospin around a fictitious magnetic field given by $\vec{B} = (-\Delta, 0, \varepsilon_{\text{ren}})$. Here $\varepsilon_{\text{ren}} = \varepsilon + \Delta E_{\text{L}} - \Delta E_{\text{R}}$ denotes the renormalized level separation which does not coincide with the bare level mismatch ε. It is changed by the energy shifts $\Delta E_{\text{L/R}}$ of the level in the left or right dot, caused by the external tunnel coupling. The renormalization of the energy mismatch caused by the external coupling and its consequences for the current through the double dot are the central statement of this section. The energy shifts are determined by the real part of the self-energy as shown in Appendix B. The renormalized level mismatch ε_{ren} has the following form:

$$\varepsilon_{\text{ren}} \;=\; \varepsilon + \Delta E_{\text{L}} - \Delta E_{\text{R}} , \tag{4.37}$$

$$\Delta E_r \;=\; \phi_r(\bar{E}) - g_\sigma\phi_r(\bar{E}+U) + (g_\sigma - 1)\,\phi_r(\bar{E}+U') , \tag{4.38}$$

$$\phi_r(\omega) \;=\; \frac{\Gamma^r}{2\pi}\text{Re}\,\Psi\left(\frac{1}{2} + i\beta\frac{\omega-\mu_r}{2\pi}\right) . \tag{4.39}$$

Here, Re denotes the real part, Ψ is the digamma function, and $\mu_{\text{L/R}} = \pm eV/2$ the leads' chemical potentials. The intradot charging energy U' (which we usually treat as infinite to avoid double occupation of one dot) serves as a natural cut off for the energy renormalization in Eq. (4.37). This is the reason why we allowed the intermediate states χ_5 in App. B to occupy these states. Additionally we note that the energy shifts $\Delta E_{\text{L/R}}$ vanish in the noninteracting case $U = U' = 0$.

The term $\frac{1}{\hbar}(\mathbf{B}\times\mathbf{I})$ gives rise to coherent oscillations inside the double dot which mix the accumulated spin in z-direction with the other components. The interdot tunneling characterized by Δ leads to a precession of the isospin around the x-axis, while the energy separation between the dot levels results in a rotation around the z-axis. It is important to

note that the renormalization of the level mismatch leads to a tilting of the eigenaxis $\vec{B}_{\rm DD}$. According to Fig. 4.5 this tilting will facilitate the hopping of electrons between the dots for $|\varepsilon_{\rm ren}| < |\varepsilon|$ and respectively aggravate the hopping for $|\varepsilon_{\rm ren}| > |\varepsilon|$. This is in agreement with the fact that elastic tunneling between the dots is only possible for resonant levels, while it is strongly suppressed by increasing level asymmetry. In the following subsection we confirm this prediction quantitatively by calculating the stationary current through the double dot.

4.2.4 Discussion

We are now interested in the manifestation of the level renormalization in the stationary current I through the double dot. A generally valid method, to calculate the current was presented in subsections 4.1.1 and 4.1.4, where the current was defined as the change of the total number of electrons in the leads. Here, the current can alternatively be defined as the number of electrons hopping from the left to the right dot [102, 103]

$$I = -e\frac{i}{\hbar}\langle[H_D, n_{\rm L}]\rangle = -\frac{e}{\hbar}\Delta{\rm Im}(\sum_\sigma P^{{\rm L}\sigma}_{{\rm R}\sigma}) = \frac{e\Delta}{\hbar}I_{\rm y} \quad , \tag{4.40}$$

where Im denotes the imaginary part. Eq. (4.40) states, that the stationary current through the double dot is given by the expectation value of the y-component of the pseudospin.

The system of master equations presented in the previous subsection together with the normalization condition $P_0 + P_1 + P_2 = 1$ can be solved analytically. The current as function of bias voltage and gate voltages has the following form:

$$\frac{\hbar}{e}I = \Delta^2\frac{A}{\varepsilon_{\rm ren}^2 + B^2} \, . \tag{4.41}$$

It has a Lorentzian dependence on the renormalized level asymmetry $\varepsilon_{\rm ren}$ between left and right dot (see Eq. (4.37)) and the factors A, B are given by:

$$\begin{aligned}
A &= \frac{Z_A}{N}; \quad B^2 = \frac{Z_0^2}{4} + \frac{\Delta^2 Z_B}{N}; \\
Z_0 &= (\sum_r \Gamma^r f^-_{r1} + g_\sigma \Gamma^r f_{r2}); \\
N &= g_\sigma \sum_r \Gamma^r (f^-_{r2} + g_\sigma f_{r2})(f^-_{r1} f_{\bar{r}1} + g_\sigma f_{r1} f_{\bar{r}2}) + \sum_r \Gamma^r (f^-_{r1} + g_\sigma f_{r1})(f^-_{r2} f^-_{\bar{r}1} + g_\sigma f_{r2} f^-_{\bar{r}2}); \\
Z_A &= \frac{g_\sigma Z_0}{4}\left(g_\sigma (f_{L2} - f_{R2})(\sum_r \Gamma^r f_{r1}) + (f_{L1} - f_{R1})(\sum_r \Gamma^r f^-_{r2}) \right); \\
Z_B &= \frac{Z_0}{4}\left[\frac{\left(\sum_r (\Gamma^r)^2 \left(f^-_{r1} f^-_{r2} + 2 g_\sigma f_{r1} f^-_{r2} + g_\sigma^2 f_{r1} f_{r2} \right)\right)}{\Gamma^L \Gamma^R} \right. \\
&\quad \left. + f^-_{L2}\left(f^-_{R1} + 2 g_\sigma f_{R1}\right) + f^-_{R2}\left(f^-_{L1} + 2 g_\sigma f_{L1}\right) + g_\sigma^2 \left(f_{L1} f_{R2} + f_{R1} f_{L2}\right) \right] \, .
\end{aligned}$$

Here $\bar{r}$ denotes the opposite of r and we use the abbreviations $f_{r1} = f_r(\bar{E})$, $f_{r1}^- = 1 - f_{r1}$, $f_{r2} = f_r(\bar{E}+U)$, $f_{r2}^- = 1 - f_{r2}$, as well as the approximation $f_r(E_L) \approx f_r(E_R) \approx f_r(\bar{E})$ and $f_r(\bar{E}+U') = 0$.

First of all we compare the stationary current given in Eq. (4.41) with results of previous publications, where the current was calculated for specific transport voltages. For this we set the Fermi functions to $f_{\mathrm{L}}(\bar{E}) = 1$ and $f_{\mathrm{L}}(\bar{E}+U) = f_{\mathrm{R}}(\bar{E}) = f_{\mathrm{R}}(\bar{E}+U) = 0$. This simplifies the current to:

$$I = \frac{e}{\hbar} \frac{\Gamma^{\mathrm{R}} \Delta^2}{\Delta^2 \left(2 + \frac{\Gamma^{\mathrm{R}}}{g_\sigma \Gamma^{\mathrm{L}}}\right) + 4(\varepsilon_{\mathrm{ren}})^2 + (\Gamma^{\mathrm{R}})^2} .$$

Neglecting renormalization effects (setting $\varepsilon_{\mathrm{ren}} = \varepsilon$), this equation reproduces for $g_\sigma = 2$ Eq. (4.19) in the paper by Gurvitz,[107] or for $g_\sigma = 1$ the result presented by Stoof and Nazarov [102]. Choosing the voltages such that the double dot can also be doubly occupied, i.e. $f_{\mathrm{L}}(\bar{E}+U) = f_{\mathrm{L}}(\bar{E}) = 1$ and $0 = f_{\mathrm{R}}(\bar{E}) = f_{\mathrm{R}}(\bar{E}+U)$ one obtains for $g_\sigma = 2$ Eq. (4.18) of Ref. [107].

It is already well-known that the current through the double dot has a Lorentzian dependence on the energy separation between left and right dot level.[102, 103, 108] However, we showed in Eq. (4.37) that the external coupling causes a shift in the energy separation $\varepsilon_{\mathrm{ren}}$ with respect to the bare level mismatch ε. Thus according to Eq. (4.41) the maxima of the current will not be centered around $\varepsilon = 0$ anymore.

It is essential to note, that the energy renormalization is not due to a capacitive coupling but due to the tunnel coupling to the reservoirs. The energy shift of the localized levels is proportional to the external coupling strength and depends on the dot level positions relative to the Fermi energy. The renormalized level separation $\varepsilon_{\mathrm{ren}}$ as function of the bias voltage is plotted in Fig. 4.6 a). It reaches a (local) extremum each time, when the Fermi energy of a lead becomes resonant with the energy needed for single ($\mu_r = \bar{E}$) or double occupation ($\mu_r = \bar{E} + U$).

The solid line in Fig. 4.6 b) shows the current (given in Eq. (4.41)) as function of the transport voltage, taking the level shift into account. The effects of level renormalizations on the current-voltage characteristics are identified by a comparison between the solid and the dashed line in Fig. 4.6 b). The dashed line shows the current-voltage characteristics if level renormalization is neglected, i.e. if the renormalized level asymmetry ε_{ren} is substituted by the bare asymmetry ε in Eq. (4.41). The current plotted by the dashed line shows steps when a lead chemical potential matches the energy needed for either single ($\bar{E}$) or double occupation ($\bar{E}+U$) of the double dot. Since the bare energy level separation ε as well as the interdot tunneling Δ shall be of the order of or smaller than Γ, i.e. $\{\Delta, \varepsilon\} \leq \Gamma$, and we consider $\Gamma < k_{\mathrm{B}}T$, the different single-particle states are not resolved as individual steps in the $I-V$ staircase but become resonant simultaneously resulting in the first current step[2]. As shown by the solid line in Fig. 4.6 b) the energy shifts of the dot levels, caused by the external tunnel coupling to the reservoirs, strongly change the

[2]Within the used approximation $f_r(E_{\mathrm{L}}) \approx f_r(E_{\mathrm{R}}) \approx f_r(\bar{E})$ the energy scales $k_{\mathrm{B}}T$ and Γ become inde-

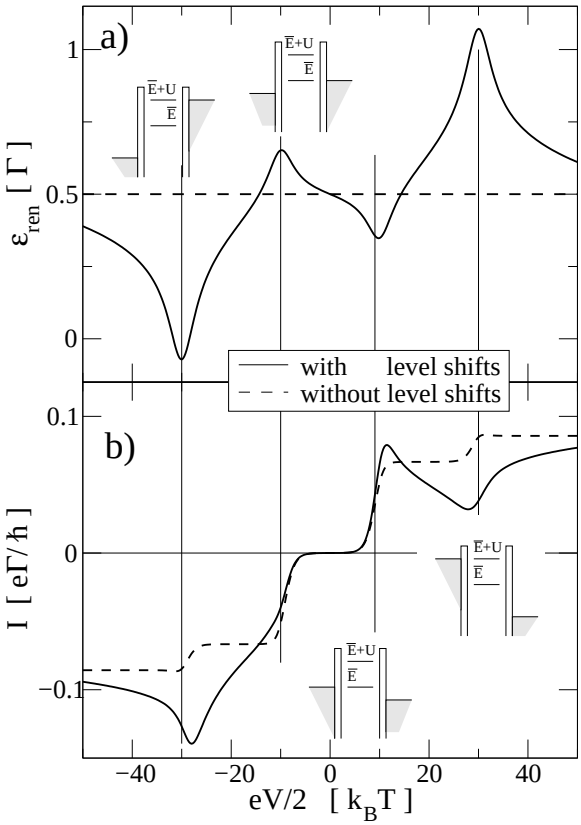

Figure 4.6: Upper part: Renormalized level spacing $\varepsilon_{\rm ren}$ (solid line) between the electronic levels in the left and right dot as function of the transport voltage V. $\varepsilon_{\rm ren}$ is extremal, when the chemical potential of a lead aligns with the energy needed for either single ($\bar{E}$) or double occupation ($\bar{E}+U$). Lower part: Current-voltage characteristics for bare (dashed line) and renormalized level spacing (solid line). Renormalization of energy levels leads to an asymmetric current-voltage characteristic. The current increases (decreases) whenever the level spacing is reduced (increased) with respect to the bare value. Plot parameters are: $\varepsilon = \Delta = \Gamma^{\rm R} = \Gamma^{\rm L} = \Gamma/2$, $\bar{E} = 10 k_{\rm B}T$, $U = 20 k_{\rm B}T$, $g_\sigma = 2$ and $U' = 100 k_{\rm B}T$.

current-voltage characteristics. Whenever the magnitude of the renormalized level spacing grows (drops) with respect to the bare asymmetry the current decreases (increases). This leads to a suppression or an enhancement of the current around the steps of the $I-V$ characteristic, leading to pronounced regions of negative differential conductance. The width of these feature is of the order of the charging energy and can exceed temperature and coupling strength significantly.

Here we comment on the assumption made in several publications, that if the lead Fermi energies are far away from the electronic states of the dots, then the renormalization of the level asymmetry can be neglected. However the energy shifts are relevant on an energy scale given by the charging energy U, as shown in Fig. 4.6 a). Therefore the assumption, that one can neglect renormalization effects and still exclude states with more than one electron occupying the double dot is not justified.

Neglecting renormalization effects and assuming symmetric coupling to the reservoirs ($\Gamma^L = \Gamma^R$), the current through the double dot is an odd function of the transport voltage (see dashed line in Fig. 4.6 b). This is not longer the case when renormalization is taken into account (see solid line in Fig. 4.6 b). The reason for this asymmetry is that

pendent. Therefore the ratio $k_{\rm B}T/\Gamma$ does not need to be specified. However, the sequential tunnel approximation still requires $k_{\rm B}T > \Gamma$.

even though the change of asymmetry, $\Delta E_{\mathrm{L}} - \Delta E_{\mathrm{R}}$, caused by level renormalization is antisymmetric with respect to the bias voltage, this in not true for the total asymmetry $\varepsilon_{ren} = \varepsilon + \Delta E_{\mathrm{L}} - \Delta E_{\mathrm{R}}$ due to the non-vanishing bare splitting ε (see Fig. 4.6 a). A comparable asymmetry in transport through two coupled dots was recently observed by Ishibashi *et al.*[115] and theoretically described by Fransson *et al.*[116, 117] However, a negative differential conductance feature cannot be uniquely linked to such renormalization effects. Due to interface capacities the level positions in the left and right dot are always affected by the transport voltage in real experiments.[70, 108]

To exclude the effect of interface capacities, we propose a complementary experiment: measuring the current at a constant transport voltage as function of the gate voltages on the dots. The resulting stability diagram is plotted in Fig. 4.7 a). Elastic sequential tunneling from the left to the right dot is possible if $E_{\mathrm{L}} \approx E_{\mathrm{R}}$ i.e. for $\varepsilon \approx 0$. Furthermore electron transport from the left to the right reservoir takes only place if the dot level for single ($\bar{E}$) or double occupation ($\bar{E}+U$) is located in the bias voltage window. Therefore the current resonance forms two stripes in the regions $-eV/2 < \bar{E} < eV/2$ and $-U - eV/2 < \bar{E} < -U + eV/2$. Away from the current stripes the occupation number of the left and right dot $(N_{\mathrm{L}}, N_{\mathrm{R}})$ is fixed, and no current crosses the structure. For a detailed discussion on stability diagrams for transport through double dots we refer to the review of van der Wiel *et al* [118].

In the absence of renormalization effects, the maxima of the current stripes would exactly coincide with the condition $E_{\mathrm{L}} = E_{\mathrm{R}}$. By plotting the current as function of the mean level position $\bar{E} = (E_{\mathrm{L}} + E_{\mathrm{R}})/2$ and the relative energy difference $\varepsilon = E_{\mathrm{L}} - E_{\mathrm{R}}$, one would therefore expect a straight horizontal line. Instead, the maximum of the current follows the renormalization shift, where the condition $\varepsilon_{\mathrm{ren}} = 0$ is fulfilled, see Fig. 4.7 b). The shift of the resonance is of order Γ as shown in Eq. (4.37) and can be small on the scale of bias voltage or temperature. The same is true for the width of the current maxima in the stability diagram in Fig. 4.7. It is not determined by temperature but in fact by the dominant coupling strength $\max(\Gamma, \Delta)$.[108] Therefore the resonance width is sharp enough for measuring the renormalization of energy levels if $\Gamma \gtrsim \Delta$ as used in Fig. 4.7. In the nonlinear transport regime ΔE_r depends on $\bar{E}$ and therefore the current stripes in Fig. 4.7 are bent and tilted against each other. This dependence can be used as a stringent experimental prove of the renormalization of energy levels. We note that the experimental challenges to perform these experiments have already been solved. For example recently Johnson *et al* measured the relevant stability diagrams for his studies on singlet-triplet spin blockade in double dots [119] and already more than 10 years ago van der Vaart and coworkers measured the linewidth of the current maxima as function of the level mismatch [108]. A detailed study of the renormalization effects should therefore be possible.

Concerning the fingerprint of the level renormalization on real experiments we note the following: First there are always internal cross capacities so that the gate voltage of one dot is a linear function of the gate voltage of the other dot. Therefore a stability diagram $I(V_{\mathrm{L}}, V_{\mathrm{R}})$ taken as function of the gate voltages at the right and left dot will experience a linear shear transformation. However straight (parallel) lines stay straight (parallel). Thus,

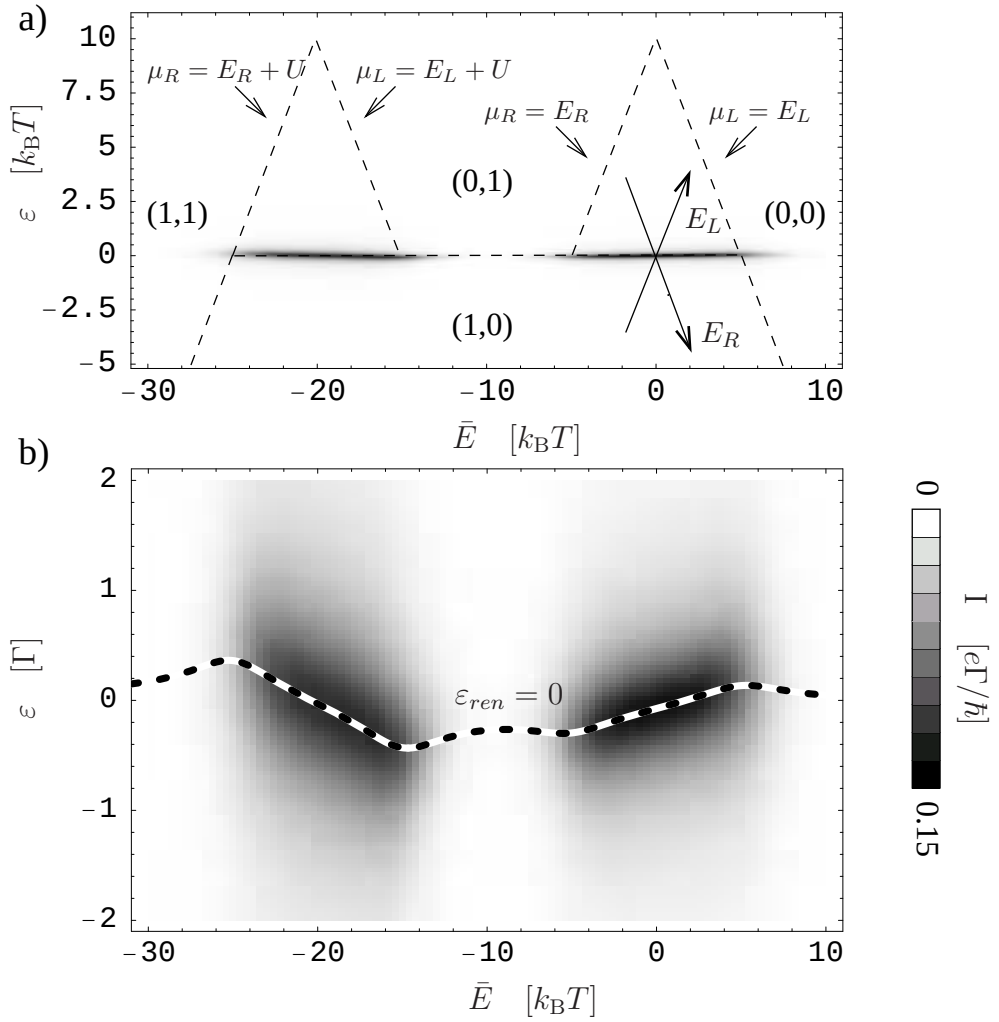

Figure 4.7: Stability diagram $I(\bar{E}, \varepsilon)$ of the current in the nonlinear transport regime. a) Elastic sequential current flows for $\varepsilon \approx 0$ and either $-eV/2 < \bar{E} < eV/2$ or $-eV/2 < \bar{E} + U < eV/2$ resulting in two current stripes. The resonances of chemical potentials $\mu_{\mathrm{L/R}}$ with the corresponding dot level are indicated and occupation of the dots is specified by ordered pairs $(N_{\mathrm{L}}, N_{\mathrm{R}})$. Also marked is the coordinate axis given by left and right dot level. b) Same as Fig. a) but for small ε. Different renormalization of left and right level shifts the current maxima by $\Delta E_{\mathrm{R}} - \Delta E_{\mathrm{L}}$ (dashed black-white line) where $\varepsilon_{\mathrm{ren}} = 0$. This leads to a tilting of the current stripes relative to each other. Parameters: $k_{\mathrm{B}}T = 5\Gamma$, $\Gamma^{\mathrm{L}} = \Gamma^{\mathrm{R}} = \Delta = \Gamma/2$, $V = 10k_{\mathrm{B}}T$, $U' = 100k_{\mathrm{B}}T$, $g_\sigma = 2$,$U = 20k_{\mathrm{B}}T$.

cross capacities cannot mimic the bending due to renormalization effects. More importantly experimental measurements of stability diagrams show in addition to the resonant current stripes explained here, further features due to inelastic or Co-tunneling processes, or due to excited levels within the bias voltage window. As discussed in references [118, 120] such effects lead to additional features within the triangles above the current strips in Fig. 4.7 a),

however, we do not expect them to interfere with our presented results.

4.2.5 Analogy to spin valve effects

In the following we outline the close analogy between the transport through a serial double dot described here and the dynamics in a spin valve described in Ref. [82, 121, 122]. Fig. 4.8

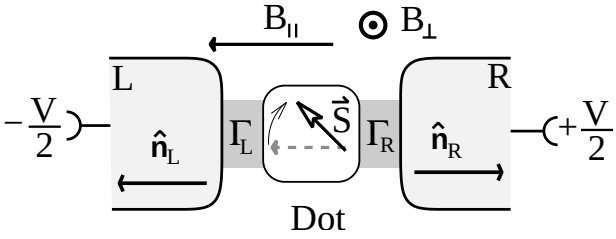

Figure 4.8: Sketch of quantum dot spin valve. A single level quantum dot is connected to two ferromagnetic reservoirs with antiparallel magnetization. The spin precesses around an external field with a component transverse ($B_\perp$) and along ($B_\parallel$) the magnetization of the leads. $B_\parallel$ is modified by an exchange field arising due to the external coupling. This exchange field is manifest in the transport properties of the spin valve.

sketches a spin valve, realized by a single level quantum dot placed between anti-aligned ferromagnets. Relating the pseudospin $\vec{I}$, in the present work with the real spin $\vec{S}$, in such a spin valve, one can perform the following mapping. The serial setup for the double dot system corresponds to the anti-aligned magnetization of the contacts in the spin valve. Furthermore the interdot tunneling translates to a transverse magnetic field in the single dot, while the level separation ε corresponds to the magnetic field component along the magnetization of the contacts. Finally the renormalization of the energy levels discussed here was introduced in the spin valve as an exchange field leading to the Hanle effect.[122]

If one extends the presented work to the parallel geometry, i.e two dots coupled in parallel to reservoirs, then four coupling strengths have to be specified, since each reservoir couples to both dots. Thus, the coupling to each reservoir can be described by a vector $\vec{\Gamma}^r$ with two components, one for each dot.[123] Alternatively on can specify the magnitude Γ^r and the angle α_r of the coupling to each reservoir. For the limiting cases $\alpha_r = 0$ or $\alpha_r = \pi$ the reservoir couples only to the upper dot or lower dot respectively. The general angle α represents the analog of arbitrary magnetizations of the leads in a spin valve.

Another interesting extension of the presented work is to look for signatures of the level shift in the noise spectrum of the double dot. Corresponding calculations for the spin valve have been recently published in reference [85].

4.3 Conclusion

If a quantum dot is connected to reservoirs, the tunnel coupling causes an energy renormalization of the electronic states. We derived the conductance of a double dot connected in series to external reservoirs for general bias voltages and temperatures, taking into account energy renormalizations. We have shown, that the conductance of such a double dot structure is affected by the energy level shifts already in a lowest order expansion in the tunnel coupling strength, which is explained by the high sensitivity of the the current through the double dot on the relative detuning of energy levels. Therefore we propose to use a double-dot system as detector for these energy renormalization effects.

We present experimental consequences of the renormalization for the current-voltage characteristics and for the stability diagram for the double dot in the nonlinear transport regime. In the current-voltage characteristics we find prominent negative differential conductances in voltage windows of the order of the charging energy. In the stability diagram of the double dot, we found that the current stripes arising as function of dot levels $E_{\mathrm{L/R}}$ are tilted against each other and are not centered at the resonance condition $E_L = E_R$, as it is the case when energy renormalization is neglected. We showed that the tilting of the current stripes is resolvable even in the sequential tunneling regime (i.e. for $\Gamma < k_{\mathrm{B}}T$) as long as the interdot tunneling, Δ, is of the same order as or smaller than the external coupling $\Gamma \geq \Delta$.

5 Conclusion

We studied the effects of Coulomb interaction on the electronic structure of semiconductor single and double dots and showed experimental consequences of these effects for optical and transport spectroscopy of the dots. Finally we reversed our perspective and did not longer restrict our studies to the fingerprints of the few-electron structure of a double dot on its transport characteristics, but showed that the electronic structure itself is changed due to the coupling to external contacts. Again we presented clear signatures of these effects in the transport characteristics of the double dot.

The excitation spectrum of a quantum dot is accessible in optical experiments and in particular in Raman spectroscopy. We calculated the charge density excitations of a self-assembled quantum dot for various numbers of electrons confined to the dot. These calculations demonstrated that charge density excitations are sensitive to the electron number and that generally low lying excitations spread over a larger energy range and shift to lower energies with increasing electron number. We explained this behavior by showing that excited states have a lower Coulomb energy than the ground state (if they are characterized by the same spin quantum numbers), so that charge density excitations appear at energies below the center of mass or single particle excitation energy. Our studies explain recently measured Raman spectra on self-assembled quantum dots.

Transport spectroscopy is another important tool to study the electronic structure of quantum dots. The current flowing through a dot coupled via high tunneling barriers to external contacts is strongly sensitive to the eigenspectrum of the dot. We presented a mechanism that completely blocks the current through a dot, even though there are allowed transitions in the transport window. This blocking mechanism only occurs if the Coulomb interaction exceeds the single-particle level spacing and is explained by a cascade of transitions leaving the dot in a fully spin-polarized state where the exit is spin blocked. An external magnetic field can switch this current blockade on and off.

The parameter space of coupled dots is further increased in compared to single dots by the interdot tunnel coupling and the splitting of the Coulomb interaction in an intradot and interdot contribution. The interdot tunneling between two identical vertically coupled dots causes an energy splitting between the symmetric and antisymmetric wavefunction. Since symmetric and antisymmetric wavefunction are delocalized, the same is expected to be true for electrons occupying the double dot. However, the Coulomb interaction prefers a maximum distance between the electrons and builds up Coulomb correlations that mix the vertical and lateral degree of freedom. We showed that the Coulomb interaction can even lead to a spontaneous charge polarization in the vertical part of the 3-electron ground state. This polarization is based on the different magnetic-field dependence of intra-

and interdot Coulomb interaction and is, thus, tuneable by an external vertical magnetic field. The strong charge polarization has severe consequences for the serial transport through the double dot. In particular the linear transport through the double dot is blocked at the critical magnetic field. Describing the spin-like degree of freedom in vertical direction (upper or lower dot) with a pseudospin, this blocking mechanism is identified as a pseudospin blockade. The magnetic field dependence and the nonlinear transport characteristics of the pseudospin are analyzed in detail.

The two presented blocking mechanisms for the transport through a single dot or a vertical double dot demonstrate the strong influence of the Coulomb interaction and Coulomb correlations on the transport characteristics of quantum dots. Reversely, it is also known that the energy spectrum of a local systems strongly coupled to reservoirs can be significantly different to the energy spectrum of the isolated local system. A prominent example is the Kondo effect in quantum dots, where the spectral density of the coupled dot shows an additional Kondo resonance at the Fermi-energy which is absent for the isolated system. While the Kondo effect can only be explained by considering higher order tunneling processes to the external reservoirs, we demonstrated that already in a consistent lowest order calculation (in the external coupling) the dynamics of a double dot connected in series to external contacts are significantly changed by the external coupling. While tunneling processes of higher order in the external coupling are suppressed at high enough temperature, already lowest order tunneling processes lead to superpositions of eigenstates. Precondition is that the coupling strength exceeds the energy difference between these states. We studied the interplay between coherent dynamics on the double dot and the incoherent external coupling and pointed out the analogy to the physics of a spin valve discussed in the context of spintronics. We demonstrated that the dot levels are shifted in energy by the external coupling and proposed an experimental verification of these effects by demonstrating clear signatures of these effects in the current-voltage characteristics and the stability diagram of the double dot.

In summary we contributed to an understanding of current experiments and presented new theoretical results together with the prediction of their experimental signatures. While the scientific community working on quantum dot spectroscopy is huge and offers a wide variety of different activities, we mention here two immediate extensions of the present work. Our discussion of the correlation induced charge-polarization in double dots presented in chapter 3 was based on results obtained by exact diagonalization of the Hamiltonian. This allowed us to take Coulomb correlation fully into account. It could be interesting to compare our results with Hartree-Fock calculations, which also include the different magnetic field dependence of intra- and interdot Coulomb interaction, but which essentially miss correlations due to quantum mechanical superpositions. We expect that the Coulomb correlations leading to the charge polarization go beyond mean field calculations. A second interesting extension of this thesis concerns the level renormalization in double dots discussed in chapter 4. There one could investigate how this effect is present in the noise power spectrum of the double dot.

A Coulomb matrix elements

A.1 Separating relative and center of mass motion

In the calculation of the Coulomb matrix elements the decomposition of a two-electron wavefunction into relative and center of mass part reduces the number of integration variables and therefore we discuss this decomposition in further detail here. The center of mass and relative coordinates are defined by:

$$\vec{R} = \frac{\vec{r}_1 + \vec{r}_2}{2}\,; \qquad \vec{P} = \vec{p}_1 + \vec{p}_2$$
$$\vec{r} = \vec{r}_1 - \vec{r}_2\,; \qquad \vec{p} = \frac{\vec{p}_1 - \vec{p}_2}{2}.$$

Here $\vec{r}_i, \vec{p}_i$ denote position and momentum of particle $i \in \{1,2\}$, while small letter (capital letters) without particle index denote the operators of the relative (center of mass) motion. Instead of defining the ladder operators for the electronic states of each electron separately as done in Eq. (2.5), we can also write the ladder operators for the center of mass and the relative motion:

$$\begin{aligned}
A_\pm &= \frac{1}{\sqrt{2}}(a_{1\pm} + a_{2\pm}) = \frac{1}{\sqrt{2}}(A_x \mp iA_y) \\
A_x: &= \frac{1}{\sqrt{2}}(\frac{X}{l_{cm}} + i\frac{l_{cm}}{\hbar}P_x)\,;\; A_y := \frac{1}{\sqrt{2}}(\frac{Y}{l_{cm}} + i\frac{l_{cm}}{\hbar}P_y) \\
a_\pm &= \frac{1}{\sqrt{2}}(a_{1\pm} - a_{2\pm}) = \frac{1}{\sqrt{2}}(a_x \pm ia_y) \\
a_x: &= \frac{1}{\sqrt{2}}(\frac{x}{l_{rel}} + i\frac{l_{rel}}{\hbar}p_x)\,;\; a_y := \frac{1}{\sqrt{2}}(\frac{y}{l_{rel}} + i\frac{l_{rel}}{\hbar}p_y)
\end{aligned}$$

Here we defined two new length scales, $l_{cm} = \frac{1}{\sqrt{2}}l$, $l_{rel} = \sqrt{2}l$. The Hamiltonian for the orbital motion of two electrons therefore has the following representations:

$$\begin{aligned}
\hat{H}^{(1)} + \hat{H}^{(2)} &= \sum_{i=1}^{2}\left(\hbar\Omega_+\left(a_{i+}^\dagger a_{i+} + \frac{1}{2}\right) + \hbar\Omega_-\left(a_{i-}^\dagger a_{i-} + \frac{1}{2}\right)\right) = \hat{H}^{(rel)} + \hat{H}^{(cm)} \\
\hat{H}^{(rel)} &= \hbar\Omega_+\left(a_+^\dagger a_+ + \frac{1}{2}\right) + \hbar\Omega_-\left(a_-^\dagger a_- + \frac{1}{2}\right) \\
\hat{H}^{(cm)} &= \hbar\Omega_+\left(A_+^\dagger A_+ + \frac{1}{2}\right) + \hbar\Omega_-\left(A_-^\dagger A_- + \frac{1}{2}\right)
\end{aligned}$$

Therefore a different representation for the normalized two-electron eigenfunctions is:

$$|N_+, N_-\rangle^{(cm)} |n_+, n_-\rangle^{(rel)} = \frac{(A_+^\dagger)^{N_+}}{\sqrt{N_+!}} \frac{(A_-^\dagger)^{N_-}}{\sqrt{N_-!}} \frac{(a_+^\dagger)^{n_+}}{\sqrt{n_+!}} \frac{(a_-^\dagger)^{n_-}}{\sqrt{n_-!}} |0,0\rangle^{(cm)} |0,0\rangle^{(rel)} . \quad \text{(A.1)}$$

The two-electron ground state is uniquely defined so that

$$|0\rangle = |0,0\rangle^{(1)} \otimes |0,0\rangle^{(2)} = |0,0\rangle^{(cm)} \otimes |0,0\rangle^{(rel)} . \quad \text{(A.2)}$$

A transformation from wavefunctions of particle coordinates to wavefunction of center of mass and relative coordinates can now be achieved by expressing the ladder operators for the single particle wavefunctions by the relative and center of mass operators:

$$a_{1\pm}^\dagger = \frac{1}{\sqrt{2}} \left(A_\pm^\dagger + a_\pm^\dagger \right) \; ; \; a_{2\pm}^\dagger = \frac{1}{\sqrt{2}} \left(A_\pm^\dagger - a_\pm^\dagger \right)$$

These relations are now inserted in the representation of the two-particle wavefunction:

$$|n_{1+}, n_{1-}\rangle^{(1)} |n_{2+}, n_{2-}\rangle^{(2)} = \frac{(a_{1+}^\dagger)^{n_{1+}}}{\sqrt{n_{1+}!}} \frac{(a_{1-}^\dagger)^{n_{1-}}}{\sqrt{n_{1-}!}} \frac{(a_{1+}^\dagger)^{n_{2+}}}{\sqrt{n_{2+}!}} \frac{(a_{1-}^\dagger)^{n_{2-}}}{\sqrt{n_{2-}!}} |0\rangle .$$

This expression can now be reexpressed in the following form:

$$\psi_{n_1 m_1}(\vec{r}_1)\, \psi_{n_2 m_2}(\vec{r}_2) = \quad \text{(A.3)}$$
$$A_{n_1 m_1 n_2 m_2} \sum_{M=M_{min}}^{M_{max}} (-1)^M \sum_{N=0}^{N_{max}} K_{N\,M}^{n_1 m_1 n_2 m_2}\, \psi_{N\,M}^{(cm)}(\vec{R})\, \psi_{N_{max}-N, m_1+m_2-M}^{(rel)}(\vec{r}),$$

Here we used the following expressions:

$$\begin{aligned}
M_{min} &= -\frac{2(n_1+n_2) - m_1 - m_2 + |m_1| + |m_2|}{2} , \\
M_{max} &= \frac{2(n_1+n_2) + m_1 + m_2 + |m_1| + |m_2|}{2} , \\
N_{max} &= \frac{1}{2} \left[2(n_1+n_2) + |m_1| + |m_2| - |M| - |m_1 + m_2 - M| \right] ,
\end{aligned}$$

$$A_{n_1 m_1 n_2 m_2} := (-1)^{m_2} \left(\prod_{i=1}^{2} 2^{(2n_i + |m_i|)} \left(\frac{2n_i + m_i + |m_i|}{2} \right)! \left(\frac{2n_i - m_i + |m_i|}{2} \right)! \right)^{-\frac{1}{2}} ,$$

$$K_{N\,M}^{n_1 m_1 n_2 m_2} := C_{\frac{1}{2}(2N+M+|M|)}^{\frac{2n_1+m_1+|m_1|}{2}, \frac{2n_2+m_2+|m_2|}{2}} C_{\frac{1}{2}(2N-M+|M|)}^{\frac{2n_1-m_1+|m_1|}{2}, \frac{2n_2-m_2+|m_2|}{2}} ,$$

$$C_a^{b\,c} := \sqrt{a!} \sqrt{(b+c-a)!} \sum_{s=\max(a-c,0)}^{min(a,b)} \binom{b}{s} \binom{c}{a-s} (-1)^s .$$

A.2 Coulomb matrix elements using relative and center of mass coordinates

The Coulomb matrix elements for a single dot or a vertically coupled double dot have the following form:

$$\frac{e^2}{4\pi\,\epsilon\,\epsilon_0}\langle n_1\,m_1\,\alpha_1\,\sigma_1, n_2\,m_2\,\alpha_2\,\sigma_2|\,\frac{1}{(r_{12}^2+(z_1-z_2)^2)^{1/2}}\,|n_1'\,m_1'\,\alpha_1\,\sigma_1, n_2'\,m_2'\,\alpha_2\,\sigma_2\rangle$$
$$=\frac{e^2}{4\pi\,\epsilon\,\epsilon_0}\int\int d^2r_1\,d^2r_2\,\frac{\psi^*_{n_1\,m_1}(\vec{r}_1)\,\psi^*_{n_2\,m_2}(\vec{r}_2)\,\psi_{n_1'\,m_1'}(\vec{r}_1)\,\psi_{n_2'\,m_2'}(\vec{r}_2)}{\sqrt{(\vec{r}_1-\vec{r}_2)^2+(1-\delta_{\alpha_1\,\alpha_2})\,d^2}}. \quad \text{(A.4)}$$

Here $r_{12}=|\vec{r}_1-\vec{r}_2|$ is the lateral distance between the two electrons, n_i, m_i are the quantum numbers determining the Fock-Darwin eigenstate, σ denotes the electron spin, and α the pseudospin labeling the dot. In a single dot all pseudospin quantum numbers are equal and $z_1=z_2$.

Transforming the two-particle wavefunctions in relative and center of mass part (see Appendix A.1), one arrives at the following expression containing only a single integration:

$$\frac{e^2}{4\pi\,\epsilon\,\epsilon_0}\,\langle n_1\,m_1\,\alpha_1\,\sigma_1, n_2\,m_2\,\alpha_2\,\sigma_2|\,\frac{1}{(r_{12}^2+(z_1-z_2)^2)^{1/2}}\,|n_1'\,m_1'\,\alpha_1\,\sigma_1, n_2'\,m_2'\,\alpha_2\,\sigma_2\rangle$$
$$=\delta_{m_1+m_2,m_1'+m_2'}\,\frac{e^2}{4\pi\,\epsilon\,\epsilon_0\,l_{rel}}A_{n_1\,m_1\,n_2\,m_2}\,A_{n_1'\,m_1'\,n_2'\,m_2'}$$
$$\times\sum_{M=\max(M_{min},M'_{min})}^{\min(M_{max},M'_{max})}\;\sum_{N=0}^{\min(N_{max},N'_{max})}K_{N\,M}^{n_1\,m_1\,n_2\,m_2}\,K_{N\,M}^{n_1'\,m_1'\,n_2'\,m_2'}$$
$$\times\int d\xi_{rel}\,\xi_{rel}\,\frac{\tilde{\rho}_{N_{max}-N,m_1+m_2-M}(\xi_{rel})\,\tilde{\rho}_{N'_{max}-N,m_1'+m_2'-M}(\xi_{rel})}{\sqrt{\xi_{rel}^2+(1-\delta_{\alpha_1\,\alpha_2})\,(d/l_{rel})^2}}. \quad \text{(A.5)}$$

For a single quantum dot or for the intradot Coulomb interaction in a vertical double dot, the single integration left in the above expression can be performed analytically [23, 33, 124, 125]

B Diagrammatic rules for sequential transport through serial double dot

With the definition $P^{\chi_1}_{\chi_2} := \langle\chi_1|\, p\, |\chi_2\rangle$, the kinetic equation Eq. (4.31) can be written as:

$$0 = i\hbar\frac{d}{dt}P^{\chi_1}_{\chi_2} \;\; = \;\; \langle\chi_1|\,[H_{\rm D}, p]\,|\chi_2\rangle + \sum_{\chi_3,\chi_4}\Sigma^{\chi_1\chi_3}_{\chi_2\chi_4}P^{\chi_3}_{\chi_4}\,. \tag{B.1}$$

As discussed in subsection 4.2.3 we are interested in the regime $\Delta_{\rm ab} \lesssim \Gamma \ll k_{\rm B}T$, where the localized states $|{\rm L}\sigma\rangle$ and $|{\rm R}\sigma\rangle$ can be used as eigenstates of the double dot in the calculation of Σ. In the following we show, how we calculate the tensor $\Sigma^{\chi_3\chi_1}_{\chi_4\chi_2}$. The states $\chi_i \in \{\ |0\rangle$, $|{\rm L}\sigma\rangle$, $|{\rm R}\sigma\rangle$, $|{\rm L}\sigma{\rm R}\sigma'\rangle\}$ still include the spin degree of freedom. We apply the diagrammatic

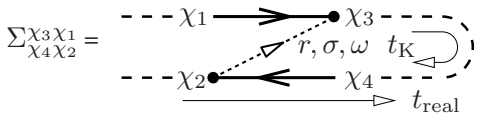

Figure B.1: Sketch of the structure of a diagram. The upper (lower) horizontal line denotes the forward (backward) propagator of the double dot system. The Keldysh time contour is labeled by $t_{\rm K}$, while the real time runs from left to right.

technique introduced in section 4.1. We shortly restate the essentials here. Within the diagrammatic approach, the tensor $\Sigma^{\chi_3\chi_1}_{\chi_4\chi_2}$ is represented as block diagram, which is a part of the Keldysh time contour as shown in Fig. B.1. The upper and lower line of the Keldysh time contour $t_{\rm K}$ represent the propagation of the double dot system forward and backward in time. They connect the matrix element characterized by the labels on the left side with the matrix element characterized by the labels on the right side. In the sequential tunneling approximation all transitions are allowed where a single electron first leaves and then reenters the double dot or vice versa. The two tunnel Hamiltonians are represented by vertices on the propagators. These vertices are connected by the contraction of the lead Fermi operators (indicated by a dashed line). Each line is characterized by its energy ω, the spin σ of the transfered electron, as well as the corresponding reservoir label $r \in \{L, R\}$. A vertex with an outgoing (incoming) tunneling line represents an electron leaving (entering) the double dot on the specified side r. All possible transitions in lowest order in the external coupling Γ belong to one of the eight diagrams depicted in Fig. B.2. $\Sigma^{\chi_3\chi_1}_{\chi_4\chi_2}$ is given by the

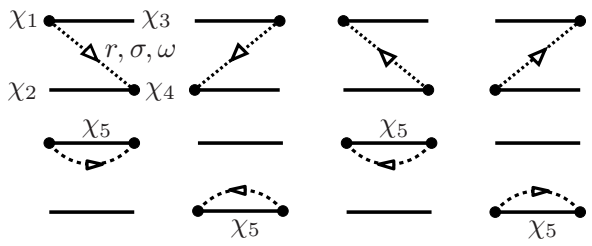

Figure B.2: All topologically different diagrams contributing to the tensor $\Sigma^{\chi_3\chi_1}_{\chi_4\chi_2}$ calculated in first order in the external coupling Γ. Labeling of the eigenstates at the four corners and of the tunneling line like in first diagram. χ_5 labels an intermediate charge state of the double dot.

sum of all diagrams with the corresponding eigenstates at the four corners, see Fig. B.2. The number of relevant diagrams is limited by spin and particle number conservation as well as to the serial system geometry. The general rules of how to calculate the diagrams are given on page 84. Within the sequential tunneling approximation these rules can be simplified for the present system in the following way:

1. Draw the upper and lower time contour. Add two tunnel vertices in any topological different way. The relevant criteria are the upper and lower contour, and the time ordering of the vertices on the real axes, not only on the Keldysh time contour. Assign to each free segment of the contour a state of the double dot and the corresponding energy. For 'bubble' diagrams like in the lower row of Fig. B.2, an intermediate state χ_5 participates.

2. The two vertices are connected by a tunnel line. Each tunnel line is labeled with the energy of the tunneling electron ω, its reservoir label r and its spin σ. Spin and reservoir label of the tunneling electron are uniquely determined by the eigenstates involved in the tunneling processes.

3. Assign to each diagram the resolvent $1/(\Delta E + i0^+)$ where ΔE is the difference between energies belonging to left going lines and energies belonging to right going lines (the tunneling line as well as the propagators).

4. The tunneling line connecting two vertices and labeled by the reservoir index r gives rise to the factor

$$\gamma_r^{\pm}(\omega) = \frac{1}{2\pi}\Gamma^r f_r^{\pm}(\omega)$$

   Here, the Fermi function $f_r^+(\omega) = f_r(\omega) = 1/(1+\exp[(\omega-\mu_r)/k_\mathrm{B}T])$ corresponds to a tunneling line that is backward directed in the Keldysh time ordering (compare Fig. B.1), and $f_r^-(\omega) = 1 - f_r(\omega)$ corresponds to a tunneling line forward directed in the Keldysh time ordering.

5. Each diagram gets a prefactor $(-1)^v$ where v is the number of vertices on the backward propagator. (This leads to an (-1) for the diagrams in the upper row of Fig. B.2.)

6. Sum over possible internal eigenstates χ_5 and integrate over the energy ω of the tunneling electron.

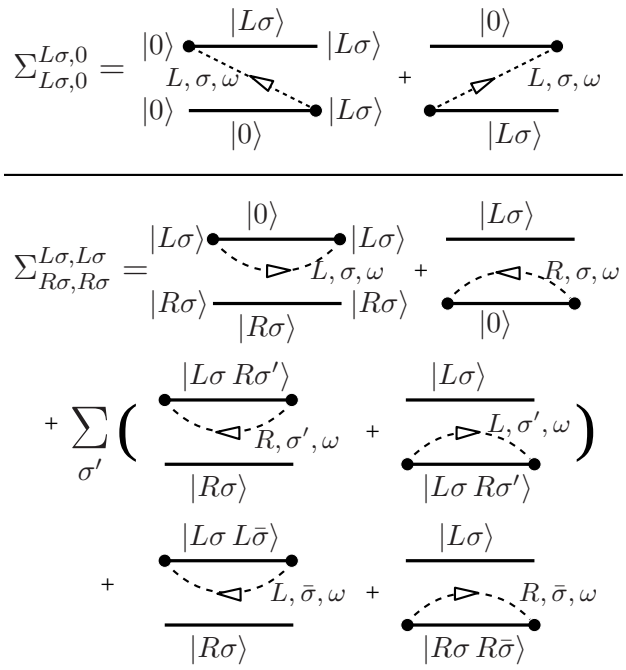

Figure B.3: Relevant diagrams contributing to two specific entries of Σ, in a lowest order expansion in Γ. Every diagram corresponding to a specific entry is labeled by the same eigenstates at its four corners.

In the parameter regime we are interested in, the following relations hold: $kT > \Gamma \geq \varepsilon, \Delta$. Therefore the energy difference between the single particle states is not resolved by the Fermi functions in the reservoir, so that we approximate the eigenenergies of $\{|0\rangle, |\mathrm{L}\sigma\rangle, |\mathrm{R}\sigma\rangle, |\mathrm{L}\sigma\mathrm{R}\sigma'\rangle\}$ by $\{0, E_\mathrm{L} \approx E_\mathrm{R} \approx \bar{E}, 2\bar{E}+U\}$. While we exclude a double occupation of a single dot for the initial or final states by setting $f_r(\bar{E}+U') = 0$ we allow the intermediate state χ_5 to be such a state. These states have the eigenenergy $2\bar{E}+U'$.

In Fig. B.3, we show as examples the diagrammatic expansion of the tensor elements $\Sigma^{\mathrm{L}\sigma,0}_{\mathrm{L}\sigma,0}$ and $\Sigma^{\mathrm{L}\sigma,\mathrm{L}\sigma}_{\mathrm{R}\sigma,\mathrm{R}\sigma}$. $\Sigma^{\mathrm{L}\sigma,0}_{\mathrm{L}\sigma,0}$ is purely imaginary and its magnitude has the meaning of a transition rate for a tunneling-in process starting from the empty double dot and resulting in a single electron with spin σ sitting in the left dot. In contrast, $\Sigma^{\mathrm{L}\sigma,\mathrm{L}\sigma}_{\mathrm{R}\sigma,\mathrm{R}\sigma}$ also has a real part which renormalizes the energy levels. Calculated in lowest order in Γ, each element of the tensor Σ can be expressed by terms of the form:

$$X_r^{(n,m)}(E) = \int d\omega \frac{\gamma_r^n(\omega)}{m(E-\omega)+i0^+}\,, \tag{B.2}$$

where n and m are either $(-)$ or $(+)$. In this notation, the algebraic expression for $\Sigma^{\mathrm{L}\sigma,\mathrm{L}\sigma}_{\mathrm{R}\sigma,\mathrm{R}\sigma}$ is:

$$\begin{aligned}\Sigma^{\mathrm{L}\sigma\mathrm{L}\sigma}_{\mathrm{R}\sigma\mathrm{R}\sigma} = \quad & X_r^{(-,+)}(\bar{E}) + X_r^{(-,-)}(\bar{E}) \\ & + g_\sigma \left(X_r^{(+,+)}(\bar{E}+U) + X_r^{(+,-)}(\bar{E}+U) \right) \\ & + (g_\sigma - 1) \left(X_r^{(+,+)}(\bar{E}+U') + X_r^{(+,-)}(\bar{E}+U') \right)\end{aligned} \tag{B.3}$$

Here and in the following we allow for an arbitrary spin degeneracy $g_\sigma \in \{1, 2\}$, since the presented treatment allows a general solution of the problem including both, the case of spin-polarized electrons ($g_\sigma = 1$), and the case of spin-degenerate electrons ($g_\sigma = 2$). Since $f_r(\bar{E} + U') = 0$ the imaginary part of the last row vanishes, however this is not the case for the real part, which causes the level renormalization. The real part of the diagrams is determined by the principal values of the integrals in Eq. (B.2) and can be expressed as a sum over digamma functions, see Eq. (4.37).

In the following we calculate the effective tensor for Σ, that only depends on the orbital or charge part of the matrix elements (denoted in the following formula by χ_1, χ_2, χ_3, χ_4) and not longer on the spin variables. This tensor is needed for the kinetic equation of the reduced density matrix defined in Eq. (4.32), where we summed over the different spin realizations of each orbital or charge state. The new tensor elements are defined by:

$$\Sigma^{\chi_3\chi_1}_{\chi_4\chi_2} = \sum_f \Sigma^{\chi_3^f\chi_1^i}_{\chi_4^f\chi_2^i} \tag{B.4}$$

Here i labels any possible spin-realization for the initial states, χ_1, χ_2, and f for the final states χ_3, χ_4. (Due to spin degeneracies the two particle states are four fold degenerate, and the left and right states are each two-fold degenerate.) The tunnel tensor $\Sigma^{\chi_3\chi_1}_{\chi_4\chi_2}$ is independent of the spin-realization i. The spin degeneracy appears only as a prefactor, but does not change the functional form of the elements. For example, $\Sigma^{\mathrm{L},0}_{\mathrm{L},0} = \sum_\sigma \Sigma^{\mathrm{L}\sigma,0}_{\mathrm{L}\sigma,0}$ describing the transition from P_0 to P_L is twice as big for spin-degenerate electrons as for spin-polarized ones. On the other hand $\Sigma^{\mathrm{L},\mathrm{L}}_{\mathrm{L},\mathrm{L}} = \Sigma^{\mathrm{L}\uparrow,\mathrm{L}\uparrow}_{\mathrm{L}\uparrow,\mathrm{L}\uparrow} + \Sigma^{\mathrm{L}\downarrow,\mathrm{L}\uparrow}_{\mathrm{L}\downarrow,\mathrm{L}\uparrow} = \Sigma^{\mathrm{L}\downarrow,\mathrm{L}\downarrow}_{\mathrm{L}\downarrow,\mathrm{L}\downarrow} + \Sigma^{\mathrm{L}\uparrow,\mathrm{L}\downarrow}_{\mathrm{L}\uparrow,\mathrm{L}\downarrow}$ describing the loss term of P_L is the same for spin-degenerate or spin-less fermions since $\Sigma^{\mathrm{L}\downarrow,\mathrm{L}\uparrow}_{\mathrm{L}\downarrow,\mathrm{L}\uparrow} = 0 = \Sigma^{\mathrm{L}\uparrow,\mathrm{L}\downarrow}_{\mathrm{L}\uparrow,\mathrm{L}\downarrow}$.

Bibliography

[1] T. Brocke, M.-T. Bootsmann, M. Tews, B. Wunsch, D. Pfannkuche, C. Heyn, W. Hansen, D. Heitmann, and C. Schüller, Phys. Rev. Lett. **91**, 257401 (2003).

[2] T. Brocke, M.-T. Bootsmann, B. Wunsch, M. Tews, D. Pfannkuche, C. Heyn, W. Hansen, D. Heitmann, and C. Schüller, Physica E **22**, 478 (2004).

[3] D. Jacob, B. Wunsch, and D. Pfannkuche, Phys. Rev. B. **70**, 081314(R) (2004).

[4] B. Wunsch, D. Jacob, and D. Pfannkuche, Physica E **26**, 464 (2005).

[5] B. Wunsch, M. Braun, J. König, and D. Pfannkuche, Phys. Rev. B. **72**, 205319 (2005).

[6] P. M. Petroff, A. Lorke, and A. Imamoglu, Physics Today **54**, 46 (2001).

[7] U. Meirav and E. B. Foxman, Semicond. Sci. Technol. **11**, 255 (1996).

[8] J. Kyriakidi, M. Pioro-Ladiere, M. Ciorga, A. Sachrajda, and P. Hawrylak, prb **66**, 035320 (2002).

[9] L. P. Kouwenhoven, D. G. Austing, and S. Tarucha, Rep. Prog. Phys. **64**, 701 (2001).

[10] A. Kumar, S. E. Laux, and F. Stern, Phys. Rev. B **42**, 5166 (1990).

[11] S. M. Reimann and M. Manninen, Rev. Mod. Phys. **74**, 1283 (2002).

[12] S. Tarucha, D. Austing, T. Honda, R. van der Hage, and L. Kouwenhoven, Phys. Rev. Lett. **77**, 3613 (1996).

[13] V. Fock, Z. Phys. **47**, 446 (1928).

[14] C. G. Darwin, Proc. Camb. Phil. Soc. **27**, 86 (1930).

[15] C. Cohen-Tannoudji, B. Diu, and F. Laloë, *Quantenmechanik 1* (Walter de Gruyter, D-10785 Berlin, 1999).

[16] W. Kohn, Phys. Rev. **123**, 1242 (1961).

[17] L. Brey, N. F. Johnson, and B. I. Halperin, Phys. Rev. B. **40**, 10647 (1989).

[18] P. A. Maksym and T. Chakraborty, Phys. Rev. Lett. **65**, 108 (1990).

[19] D. Jacob, *Diploma thesis* (Universität Hamburg, Germany, 2002).

[20] R. J. Warburton, B. T. Miller, C. S. Dürr, C. Bödefeld, K. Karrai, J. P. Kotthaus, G. Medeiros-Ribeiro, P. M. Petroff, and S. Huant, Phys. Rev. B. **58**, 16221 (1998).

[21] P. Maksym and T. Chakraborty, Phys. Rev. Lett. **65**, 108 (1990).

[22] H. Tamura, Annalen der Physik **13**, 249 (2004).

[23] M. Rontani, C. Cavazzoni, D. Bellucci, and G. Goldoni, cond-mat 0508111 (2005).

[24] D. Pfannkuche, V. Gudmundson, and P. A. Maksym, Phys. Rev. B **47**, 2244 (1993).

[25] L. P. Kouwenhoven, G. Schön, and L. L. Sohn, *in Mesoscopic Electron Transport, edited by L. L. Sohn, L. P. Kouwenhoven, and Gerd Schön* (Kluwer Academic Publishers, Dordrecht, Boston, London, 1997), pp. 1–44.

[26] J. König, J. Schmid, and H. Schoeller, Phys. Rev. B. **54**, 16820 (1996).

[27] C. W. J. Beenakker, Phys. Rev. B. **44**, 1646 (1991).

[28] D. Pfannkuche and S. E. Ulloa, Phys. Rev. Lett. **74**, 1194 (1995).

[29] D. Weinmann, W. Häusler, and B. Kramer, Phys. Rev. Lett. **74**, 984 (1995).

[30] A. Hüttel, H. Qin, A. W. Holleitner, R. H. Blick, K. Neumaier, D. Weinmann, K. Eberl, and J. P. Kotthaus, Europhys. Lett. **62**, 712 (2003).

[31] J. Weis, R. J. Haug, K. von Klitzing, and K. Ploog, *in Quantum Dynamics of Submicron Structures, edited by H. A. Cerdeira, B. Kramer, and G. Schön* (Kluwer Academic Publishers, Dordrecht, Boston, London, 1995), pp. 263–274.

[32] J. Weis, *Habilitation Thesis* (Universität Stuttgart, Max-Planck-Institut für Festkörperforschung, Germany, 2002).

[33] D. Pfannkuche, *Habilitation Thesis* (Universität Karlsruhe, Germany, 1998).

[34] D. Weinmann, W. Häusler, and B. Kramer, Ann. Phys. **5**, 652 (1996).

[35] D. Weinmann, W. Häusler, K. Jauregui, and B. Kramer, *in Quantum Dynamics of Submicron Structures, edited by H. A. Cerdeira, B. Kramer, and G. Schön* (Kluwer Academic Publishers, Dordrecht, Boston, London, 1995), pp. 297–310.

[36] J. Weis, R. J. Haug, K. v. Klitzing, and K. Ploog, Phys. Rev. Lett. **71**, 4019 (1993).

[37] C. Romeike, M. R. Wegewijs, and H. Schoeller, cond-mat 0502091 (2005).

[38] F. Cavaliere, A. Braggio, J. Stockburger, M. Sassetti, and B. Kramer, Phys. Rev. Lett. **93**, 036803 (2004).

[39] F. Cavaliere, A. Braggio, M. Sassetti, and B. Kramer, Phys. Rev. B. **70**, 125323 (2004).

[40] T. Fujisawa, D. Austing, Y. Tokura, Y. Hirayama, and S. Tarucha, Phys. Rev. Lett. **88**, 236801 (2002).

[41] D. G. Austing, T. Honda, K. Muraki, Y. Tokura, and S.Tarucha, Physica B **249-251**, 206 (1998).

[42] D. G. Austing, T. Honda, and S.Tarucha, Jpn. J. Appl. Phys. **36**, 1667 (1997).

[43] G. Burkard, G. Seelig, and D. Loss, Phys. Rev. B **62**, 2581 (2000).

[44] S.-R. E. Yang, J. Schliemann, and A. MacDonald, Phys. Rev. B **66**, 153302 (2002).

[45] D. Bellucci, M. Rontani, F. Troiani, G. Goldoni, and E. Molinari, Phys. Rev. B. **69**, 201308(R) (2004).

[46] L. Martin-Moreno, L. Brey, and C. Tejedor, Phys. Rev. B. **62**, 10633 (2000).

[47] B. Partoens and F. Peeters, Europhys. Lett. **56**, 86 (2001).

[48] Y. Tokura, S. Sasaki, D. G. Austing, and S. Tarucha, Physica E **6**, 676 (2000).

[49] B. Partoens and F. Peeters, Phys. Rev. Lett. **84**, 4433 (2000).

[50] Y. T. D. G. Austing and S. Tarucha, J. Phys.: Condens. Matter **11**, 6023 (1999).

[51] M. Rontani, F. Troiani, U. Hohenester, and E. Molinari, Solid State Commun. **119**, 309 (2001).

[52] M. Rontani, F. Rossi, F. Manghi, and E. Molinari, Solid State Commun. **112**, 151 (1999).

[53] M. Rontani, S. Amaha, K. Muraki, F. Manghi, E. Molinari, S. Tarucha, and D. Austing, Phys. Rev. B. **69**, 085327 (2004).

[54] D. G. Austing, S.Tarucha, K. Muraki, F. Ancilotto, M. Barranco, A. Emperador, R. Mayol, and M. Pi, Physica E **22**, 502 (2004).

[55] D. G. Austing, S.Tarucha, H. Tamura, K. Muraki, F. Ancilotto, M. Barranco, A. Emperador, R. Mayol, and M. Pi, Phys. Rev. B. **70**, 045324 (2004).

[56] F. Ancilotto, D. G. Austing, M. Barranco, R. Mayol, K. Muraki, M. Pi, S. Sasaki, and S. Tarucha, Phys. Rev. B. **67**, 205311 (2003).

[57] S. Amaha, D. G. Austing, Y. Tokura, K. Muraki, K. Ono, and S.Tarucha, Solid State Commun. **119**, 183 (2001).

[58] M. Pi, A. Emperador, M. Barranco, F. Garcias, K. Muraki, S. Tarucha, and D. G. Austing, Phys. Rev. Lett. **87**, 066801 (2001).

[59] K. Ono, D. G. Austing, Y. Tokura, and S. Tarucha, Science **297**, 1313 (2002).

[60] J. J. Palacios and P. Hawrylak, Phys. Rev. B **51**, 1769 (1995).

[61] H. Imamura, H. Aoki, and P. A. Maksym, Phys. Rev. B **57**, R4257 (1998).

[62] H. Imamura, P. A. Maksysm, and H. Aoki, Phys. Rev. B **59**, 5817 (1999).

[63] H. Imamura, P. A. Maksym, and H. Aoki, Phys. Rev. B **53**, 12613 (1996).

[64] B. Partoens, V. Schweigert, and F. Peeters, Phys. Rev. Lett. **79**, 3390 (1997).

[65] B. Partoens, A. Matulis, and F. Peeters, Phys. Rev. B. **59**, 1617 (1999).

[66] G. Goldoni, F. Troiani, M. Rontani, D. Bellucci, and E. Molinari, cond-mat 0405261 (2004).

[67] B. Partoens and F. Peeters, Physica B **298**, 282 (2001).

[68] B. Szafran and F. M. Peeters, Phys. Rev. B. **71**, 245314 (2005).

[69] A. K. Hüttel, S. Ludwig, K. Eberl, and J. P. Kotthaus, Phys. Rev. B. **72**, 081310(R) (2005).

[70] D. Pfannkuche, R. H. Blick, R. J. Haug, K. von Klitzing, and K. Eberl, Superlattices & Microstruct. **23**, 1255 (1998).

[71] G. Klimeck, G. Chen, and S. Datta, Phys. Rev. B **45**, 1951 (1992).

[72] K. Ono, D. G. Austing, Y. Tokura, and S. Tarucha, Physica B **314**, 450 (2002).

[73] S. Debald, Ph.D. thesis, Universität Hamburg, 2005.

[74] A. Bertoni, M. Rontani, G. Goldoni, F. Troiani, and E. Molinari, Physica E **26**, 427 (2005).

[75] J. König, H. Schoeller, and G. Schön, Phys. Rev. Lett. **76**, 1715 (1996).

[76] J. König, *Quantum Fluctuations in the Single-Electron Transistor* (Shaker Verlag, Aachen, 1999).

[77] H. Schoeller, *in Mesoscopic Electron Transport, edited by L. L. Sohn, L. P. Kouwenhoven, and Gerd Schön* (Kluwer Academic Publishers, Dordrecht, Boston, London, 1997), pp. 291–330.

[78] R. Schleser, T. Ihn, E. Ruh, K. Ensslin, M. Tews, D. Pfannkuche, D. C. Driscoll, and A. C. Gossard, Phys. Rev. Lett. **94**, 206805 (2005).

[79] A. Thielmann, M. H. Hettler, J. König, and G. Schön, Phys. Rev. Lett. **95**, 146806 (2005).

[80] A. Braggio, J. König, and R. Fazio, Phys. Rev. Lett. **96**, 026805 (2006).

[81] J. Aghassi, A. Thielmann, M. Hettler, and G.Schön, cond-mat 0505345 (2005).

[82] M. Braun, J. König, and J. Martinek, Phys. Rev. B. **70**, 195345 (2004).

[83] M. Büttiker, Phys. Rev. B **46**, 12485 (1992).

[84] Y. M. Blanter and M. Büttiker, Phys. Rep. **336**, 1 (2000).

[85] M. Braun, J. König, and J. Martinek, cond-mat 0601366 (2006).

[86] H. Schoeller and J. König, Phys. Rev. Lett. **84**, 3686 (2000).

[87] S. Mukamel, Phys. Rev. E **68**, 21111 (2003).

[88] W. Nolting, *Grundkurs: Theoretische Physik*, 3rd ed. (Zimmermann-Neufang, Ulmen, 2000), Vol. 7. Vielteilchen-Physik.

[89] A. Thielmann, Ph.D. thesis, Universität Karlsruhe, 2005.

[90] H. Schoeller, cond-mat 9909400 (1999).

[91] J. R. Petta, A. C. Johnson, J. Taylor, E. Laird, A. Yacoby, M. Lukin, C. M. Marcus, M. P. Hanson, and A. C. Gossard, Science **309**, 2180 (2005).

[92] T. H. Oosterkamp, S. F. Godijn, M. J. Uilenreef, Y. V. Nazarov, N. C. van der Vaart, and L. P. Kouwenhoven, Phys. Rev. Lett. **80**, 4951 (1998).

[93] R. H. Blick, D. Pfannkuche, R. J. Haug, K. v. Klitzing, and K. Eberl, Phys. Rev. Lett. **80**, 4032 (1998).

[94] T. Hayashi, T. Fujisawa, H. D. Cheong, Y. H. Jeong, and Y. Hirayama, Phys. Rev. Lett. **91**, 226804 (2003).

[95] D. Loss and D. P. DiVincenzo, Phys. Rev. A **57**, 120 (1998).

[96] V. N. Golovach and D. Loss, Semicond. Sci. Technol. **17**, 355 (2002).

[97] J. Taylor, H.-A. Engel, W. Dür, A. Yacoby, C. Marcus, P. Zoller, and M. Lukin, Nature **1**, 177 (2005).

[98] J. Taylor, W. Dür, P. Zoller, A. Yacoby, C. Marcus, and M. Lukin, Phys. Rev. Lett. **94**, 236803 (2005).

[99] T. Fujisawa, T. Hayashi, H. Cheong, Y. Jeong, and H. Hirayama, Physica E **21**, 1046 (2003).

[100] J. R. Petta, A. C. Johnson, C. M. Marcus, M. P. Hanson, and A. C. Gossard, Phys. Rev. Lett. **93**, 186802 (2004).

[101] T. Brandes, physics reports **408**, 315 (2005).

[102] T. H. Stoof and Y. V. Nazarov, Phys. Rev. B. **53**, 1050 (1996).

[103] B. L. Hazelzet, M. R. Wegewijs, T. H. Stoof, and Y. V. Nazarov, Phys. Rev. B. **63**, 165313 (2001).

[104] H. Sprekeler, G. Kießlich, A. Wacker, and E. Schöll, Phys. Rev. B. **69**, 125328 (2004).

[105] S. A. Gurvitz, Phys. Rev. B. **56**, 15215 (1997).

[106] S. A. Gurvitz, Phys. Rev. B. **57**, 6602 (1998).

[107] S. A. Gurvitz and Y. S. Prager, Phys. Rev. B. **53**, 15932 (1996).

[108] N. C. van der Vaart, S. F. Godijn, Y. V. Nazarov, C. J. P. M. Harmans, J. E. Mooij, L. W. Molenkamp, and C. T. Foxon, Phys. Rev. Lett. **74**, 4702 (1995).

[109] T. Ota, K. Ono, M. Stopa, T. Hatano, S. Tarucha, H. Z. Song, Y. Nakata, T. Miyazawa, T. Ohshima, and N. Yokoyama, Phys. Rev. Lett. **93**, 066801 (2004).

[110] B. Wunsch and A. Chudnovskiy, Phys. Rev. B. **68**, 245317 (2003).

[111] B. Wunsch and A. Chudnovskiy, Physica E **22**, 353 (2004).

[112] K. Blum, *Density Matrix Theory and Applications* (Plenum Press, New York, 1996).

[113] U. Hartmann and F. K. Wilhelm, Phys. Rev. B. **67**, 161307(R) (2003).

[114] U. Hartmann and F. K. Wilhelm, Phys. Rev. B. **69**, 161309(R) (2004).

[115] K. Ishibashi, M. Suzuki, T. Ida, and Y. Aoyagi, Appl. Phys. Lett. **79**, 1864 (2001).

[116] J. Fransson and O. Eriksson, J. Phys.: Condens. Matter **16**, L85 (2004).

[117] J. Fransson and O. Eriksson, Phys. Rev. B. **70**, 085301 (2004).

[118] W. der Wiel, S. D. Franceschi, J. Elzerman, T. Fujisawa, S. Tarucha, and L. Kouwenhoven, Rev. Mod. Phys. **75**, 1 (2003).

[119] A. C. Johnson, J. R. Petta, M. Marcus, M. P. Hanson, and A. C. Gossard, Phys. Rev. B. **72**, 165308 (2005).

[120] T. Fujisawa, T. Oosterkamp, W. G. van der Wiel, B. W. Broer, R. Aguado, S. Tarucha, and L. Kouwenhoven, Science **282**, 932 (1998).

[121] J. König and J. Martinek, Phys. Rev. Lett. **90**, 166602 (2003).

[122] M. Braun, J. König, and J. Martinek, Europhys. Lett. **72**, 294 (2005).

[123] A. L. Chudnovskiy, Europhys. Lett. **71**, 672 (2005).

[124] E. Anisimovas and A. Matulis, J. Phys.: Condens. Matter **10**, 601 (1998).

[125] D. Pfannkuche, R. Gerhardts, P. A. Maksym, and V. Gudmundson, Physica B **189**, 6 (1993).

Acknowledgments

I acknowledge the support of many people who contributed to the presented thesis in many ways. First of all I would like to thank my supervisor Prof. D. Pfannkuche. She was competent in all questions concerning quantum dots and helped a lot in identifying the crucial points of my research and to present them in publications and on conferences. She managed to keep smiling and to stay sympathetic in all situations.

This thesis is a result of various productive cooperation. I thank Prof. J. König and Matthias Braun for our very interesting and fruitful cooperation on sequential transport through double dots. I profited a lot from their profound knowledge about the transport theory and the diagrammatique technique. I thank Prof. Schueller and Thomas Brocke who gave me an interesting insight in Raman spectroscopy on quantum dots, which lead to a very fruitful cooperation. I thank David Jacob for a pleasant and productive cooperation on the charge polarization and pseudospin blockade in double quantum dots. I thank Michael Tews for sharing his interest and knowledge about transport spectroscopy with me. It was a great pleasure to work with him on the transport blocking presented in the first part of this thesis.

Besides these major cooperations I want to acknowledge the support of several other people. I thank Prof. G. Platero for her interest in my work and for refereeing this thesis. I thank Alexander Chudnovskiy, who was always interested in my work and who contributed a lot to my understanding of mesoscopic physics. I thank Karel Výborný for his helpful feedback on my work and and his useful ideas. It was a pleasure to share the office with him. I thank Frank Deuretzbacher and Frank Hellmuth for many interesting discussions and helpful ideas.

I furthermore appreciate interesting feedback and comments on my work from Stefan Debald, Till Vorrath, Alexander Struck, Maxim Rogge, Jasmin Aghassi, Matthias Hettler, Alexandro Braggio and Massimo Rontani. Of course I thank all my colleagues for the good atmosphere and their help concerning computer problems as well as physical questions.

Finally I would like to thank my wife and my family for their constant support throughout the years.

Financial support by the DFG via SFB 508 is gratefully acknowledged.